

Russian Original Vol. 56, No. 1, January, 1984

July, 1984

JOF
~~AS~~
JAL
File

SATEAZ 56(1) 1-64 (1984)

SOVIET ATOMIC ENERGY

АТОМНАЯ ЭНЕРГИЯ
(ATOMNAYA ÉNERGIYA)

TRANSLATED FROM RUSSIAN



CONSULTANTS BUREAU, NEW YORK

SOVIET ATOMIC ENERGY

Soviet Atomic Energy is abstracted or indexed in *Chemical Abstracts*, *Chemical Titles*, *Pollution Abstracts*, *Science Research Abstracts*, *Parts A and B*, *Safety Science Abstracts Journal*, *Current Contents*, *Energy Research Abstracts*, and *Engineering Index*.

Soviet Atomic Energy is a translation of *Atomnaya Énergiya*, publication of the Academy of Sciences of the USSR.

An agreement with the Copyright Agency of the USSR (VAAP) makes available both advance copies of the Russian journal and original glossy photographs and artwork. This serves to decrease the necessary time lag between publication of the original and publication of the translation and helps to improve the quality of the latter. The translation began with the first issue of the Russian journal.

Editorial Board of *Atomnaya Énergiya*:

Editor: O. D. Kazachkovskii

Associate Editors: N. A. Vlasov and N. N. Ponomarev-Stepnoi

Secretary: A. I. Artemov

I. N. Golovin	V. V. Matveev
V. I. Il'ichev	I. D. Morokhov
V. F. Kalinin	A. A. Naumov
P. L. Kirillov	A. S. Nikiforov
Yu. I. Koryakin	A. S. Shtan'
E. V. Kulov	B. A. Sidorenko
B. N. Laskorin	M. F. Troyanov
E. I. Vorob'ev	

Copyright © 1984, Plenum Publishing Corporation. *Soviet Atomic Energy* participates in the Copyright Clearance Center (CCC) Transactional Reporting Service. The appearance of a code line at the bottom of the first page of an article in this journal indicates the copyright owner's consent that copies of the article may be made for personal or internal use. However, this consent is given on the condition that the copier pay the flat fee of \$8.50 per article (no additional per-page fees) directly to the Copyright Clearance Center, Inc., 21 Congress Street, Salem, Massachusetts 01970, for all copying not explicitly permitted by Sections 107 or 108 of the U.S. Copyright Law. The CCC is a nonprofit clearinghouse for the payment of photocopying fees by libraries and other users registered with the CCC. Therefore, this consent does not extend to other kinds of copying, such as copying for general distribution, for advertising or promotional purposes, for creating new collective works, or for resale, nor to the reprinting of figures, tables, and text excerpts. 0038-531X/84 \$8.50

Consultants Bureau journals appear about six months after the publication of the original Russian issue. For bibliographic accuracy, the English issue published by Consultants Bureau carries the same number and date as the original Russian from which it was translated. For example, a Russian issue published in December will appear in a Consultants Bureau English translation about the following June, but the translation issue will carry the December date. When ordering any volume or particular issue of a Consultants Bureau journal, please specify the date and, where applicable, the volume and issue numbers of the original Russian. The material you will receive will be a translation of that Russian volume or issue.

Subscription (2 volumes per year)

Vols. 54 & 55: \$500 (domestic); \$555 (foreign)	Single Issue: \$100
Vols. 56 & 57: \$560 (domestic); \$621 (foreign)	Single Article: \$8.5

CONSULTANTS BUREAU, NEW YORK AND LONDON



233 Spring Street
New York, New York 10013

Published monthly. Second-class postage paid at Jamaica, New York 11431.

Mailed in the USA by Publications Expediting, Inc., 200 Meacham Avenue, Elmont, NY 11003.

POSTMASTER: Send address changes to *Soviet Atomic Energy*, Plenum Publishing Corporation, 233 Spring Street, New York, NY 10013.

SOVIET ATOMIC ENERGY

A translation of *Atomnaya Énergiya*

July, 1984

Volume 56, Number 1

January, 1984

CONTENTS

Engl./Russ.

ARTICLES

High-Temperature Power-Technological Reactor with Solid Coolant and Radiative Heat Exchange - A. M. Alekseev, Yu. M. Bulkin, S. I. Vasil'ev, E. S. Gerasimov, N. A. Dollezhal', I. Ya. Emel'yanov, N. D. Zaichko, Yu. I. Koryakin, É. K. Nazarov, A. V. Petrushin, S. V. Radchenko, V. P. Smirnov, V. A. Chernyaev, and I. L. Chikhladze	1	5
Synthesis of a System for Stabilizing Reactor Power and Energy Distribution on the Basis of Lateral Ionization Chambers - I. Ya. Emel'yanov, L. N. Podlazov, A. N. Aleksakov, E. V. Nikolaev, V. M. Panin, and V. D. Rogova	8	11
Analysis of the Statistical Error and Optimization of Correlation Flow Meters - B. V. Kebabze	13	15
Analytic Approximation of Neutron Physics Data - S. A. Badikov, V. A. Vinogradov, E. V. Gai, and N. S. Rabotnov	19	20
Fracture Rate of 10Kh2M Steel When Water Enters Sodium in a Counterflow Steam Generator - V. S. Sroelov, P. P. Bocharin, A. A. Saigin, and T. I. Vasilevich	26	25
Hydrogen Balance in the INTOR Reactor - V. A. Sharapov, A. E. Gorodetski, A. P. Zakharov, and A. I. Pavlov	30	29
Effect of Uncertainties in Neutron Cross Sections on the Characteristics of a Thermonuclear Reactor Blanket and Shield - A. I. Ilyushkin, I. I. Linge, V. P. Mashkovich, V. K. Sakharov, G. E. Shatalov, and A. V. Shikin	34	32
Spatial Distributions of Dose Fields in a Water Absorber Bombarded with High-Energy Nucleons - A. Ya. Serov, B. S. Sychev, E. P. Cherevatenko, and S. V. Chernov	39	36
Fused Silica in Ionizing-Radiation Dosimetry - R. R. Gulamova, N. A. Kasimov, and M. I. Muminov	44	40
An Application Package for Processing and Analyzing Data on the Environment and Population Health - E. I. Vorob'ev, V. A. Kornelyuk, A. S. Kuz'menko, V. Yu. Reznichenko, and V. L. Shestopalov	48	43
Radionuclide Deflation Effects in a Contaminated Locality with Intermittent and Steady-State Discharges into the Atmosphere - K. P. Makhon'ko	52	47
Use of Proton and Deuteron Activation Method of Analysis in the Determination of Elements with $Z > 42$ - S. Mukhammedov, A. Vasidov, and É. Pardaev	56	50

CONTENTS

(continued)

Engl./Russ.

LETTERS TO THE EDITOR

Results of Measurements of the Neutron Field in the Channels of the VVER-1000 - S. S. Lomakin, A. G. Morozov, G. G. Panfilov, V. P. Kruglov, and G. M. Bakhirev	59	54
Amplitude Characteristic of Pyroelectric Detectors - V. A. Borisyonok and E. Z. Novitskii	61	55

**The Russian press date (podpisano k pečati) of this issue was 12/31/1983.
Publication therefore did not occur prior to this date, but must be assumed
to have taken place reasonably soon thereafter.**

ARTICLES

HIGH-TEMPERATURE POWER-TECHNOLOGICAL
REACTOR WITH SOLID COOLANT AND RADIATIVE
HEAT EXCHANGE

A. M. Alekseev, Yu. M. Bulkin,
S. I. Vasil'ev, E. S. Gerasimov,
N. A. Dollezhal', I. Ya. Emel'yanov,
N. D. Zaichko, Yu. I. Koryakin,
É. K. Nazarov, A. V. Petrushin,
S. V. Radchenko, V. P. Smirnov,
V. A. Chernyaev, and I. L. Chikhladze

UDC 621.039.5/6+621.039.524.2

A high-temperature power-technological reactor for carrying out processes based on endothermic chemical reactions usually is associated with a reactor in which helium under pressure is used as the coolant. The temperature necessary for the efficient conduct of the majority of high-temperature power-technological processes amounts to 850–900°C. The direct transfer of heat from the coolant of the core directly into the technological process is excluded on the grounds of radiation safety: The population uses the product obtained as the result of power-technological processes. Therefore, in such a process the radiation-uncontaminated heat can be supplied only through some or other system of heat-exchange facilities. This means that the coolant temperature (in this case helium) at the core outlet must be somewhat higher and must attain ~950–1000°C. The problem of obtaining and, mainly, of transferring into the process coolant at this temperature through a system of heat-exchange facilities also in the main determines the whole complexity of the construction of a commercial power-technological reactor.

The possibility of overcoming such a high-temperature barrier undoubtedly is increased by finding alternative concepts for reactors of this designation. We note, that at one time the economic competitiveness of electric power reactors was mainly promoted by alternative reactor concepts, extending the feasibility of utilizing coolant with a temperature of ~300°C, at which the majority of light-water reactors operate for the production of electric power.

In this paper, a graphite reactor is described in which the principle of heat transfer by radiative heat-exchange from a solid coolant is used (GROTT). It is proposed to utilize in the nuclear-chemical assembly of the production plant, ammonia as the principal source of high-temperature heat for the steam catalytic conversion of methane.

Construction of the Reactor Facility [1]. The reactor vessel is made of sheet carbon steel in the form of a leaktight ring-shaped box of rectangular cross section. The cover and the base are flat. The vessel is filled with an inert gas (helium) at a pressure close to atmospheric. In one of the sector spaces of the vessel, occupying approximately 1/10th of the volume of the annular graphite brickwork, the core is located. In the remaining space, the plant of the technological zone is located (Fig. 1).

The core moderator is made of graphite blocks, collected in rows of curved stacks (Fig. 2), which are installed concentrically one to the other with a specified pitch over the radius. Above, below, outside, and inside face, the core is surrounded by the reflector, also assembled from graphite blocks. In the longitudinal direction of the core, the curved stacks of the fixed moderator become the brickwork of the so-called neutron cutoff, consisting of graphite blocks with a high-temperature absorbing material. Between the rows of the moderator brickwork, also concentrically with the gaps relative to it, are installed the ring-shaped masonry of the solid coolant, assembled from graphite blocks with a high-temperature nuclear fuel in the form of microparticles with a multilayered graphite cladding. The masonry of the solid coolant is installed on individual supporting annular rotating platforms, made of separate steel curved sections and joined together in a ring with special tie rods. The design of the tie rods ensures, on the one hand, joining of these sections into a single annular rotating platform without free play and, on the other hand, preservation of the originally fixed diameter of the

Translated from *Atomnaya Énergiya*, Vol. 56, No. 1, pp. 5–10, January, 1984. Original article submitted April 27, 1983.

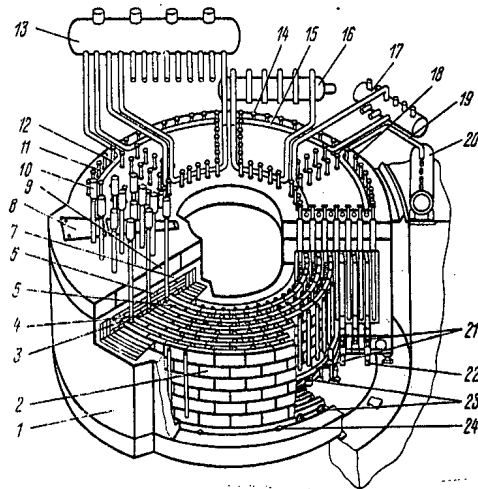


Fig. 1.

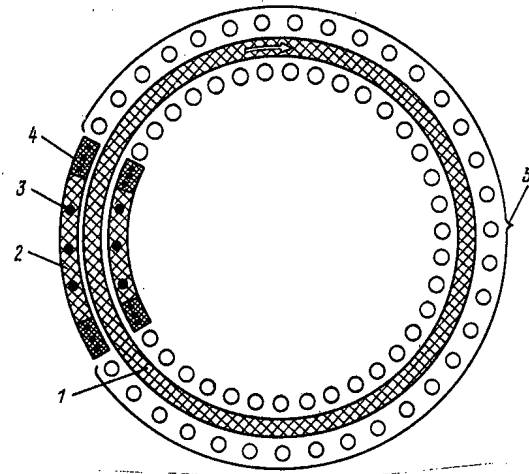


Fig. 2

Fig. 1. Reactor facility with solid coolant: 1) reactor vessel; 2) solid coolant brickwork; 3) core reflector; 4) core moderator brickwork; 5) brickwork of the neutron cutoff zone; 6) thermal shield; 7) thermal insulation; 8) radiation shield; 9) unloading-loading manhole; 10) control and safety rod slave mechanism; 11) evaporative channel; 12) evaporative zone group collector; 13) drum-separator; 14) steam-gas channel; 15) group collector of the steam-gas mixture; 16) steam-gas mixer; 17) distributing collector; 18) conversion channel; 19) conversion zone group collector; 20) composite collector; 21) bearing-rotatable platform; 22) solid coolant actuator; 23) supporting roller; 24) centering roller.

Fig. 2. Diagram of an annular element of the reactor facility: 1) ring-shaped masonry of the mobile solid coolant; 2) masonry of the fixed graphite-moderator of the core; 3) control and safety rods; 4) masonry of the neutron cutoff zone; 5) technological zone (heat-exchanger).

platform (and, consequently, of the coolant brickwork) over the whole range of their working temperature. Each annular platform is supported on rollers and driving wheels installed on the bottom of the vessel. The driving wheels are connected through a leaktight magnetic coupling with individual electric drives. The magnetic couplings are located in cuttings through the bottom of the vessel, and the electric drives are disposed in the sub-reactor compartment. The technological channels are located in the technological zone in the gaps between the rows of the solid coolant masonry. They are also arranged in concentric rows and are grouped according to purpose.

In accordance with the possible variations of the layout of the reactor facility, the channels for the steam catalytic conversion of natural gas (methane), evaporative and superheat channels, channels for heating up the steam-gas mixture, etc. can be located in the technological zone of the reactor. All the channels are structurally designed according to the Field scheme, and the heads of the channels are sealed to the upper flanges of the cuttings through the cover of the vessel. Each group of channels, serving some or other purpose, is joined through headers with the inlet and outlet main lines from the corresponding technological plant of the facility.

The reactor vessel is shielded from inside from the high temperature with a thermal insulator. The cover of the reactor vessel is filled with a material which shields the compartments located above it from the radiative emission. The cover is cooled with water by coils laid in it.

The rods of the reactor control and safety system are arranged in vertical openings of the moderator brickwork, and the rod actuators are brought out at the cap of the radiator.

The principal characteristics of the reactor for a chemical combine with a production of ~1 million tons of ammonia per annum are as follows:

Thermal power, MW	~500
Nuclear fuel charge per run with nuclear fuel enriched to 10% in ^{235}U , tons	~25
Running time of facility before recharging fuel and replacement of conversion tubes, years	~10
Solid coolant in the form of ring-shaped bricks:	
number of ring-shaped bricks	12
diameter of central ring, m	24

height of active part of ring, m	4
peripheral velocity of ring, m/sec	0.5
maximum temperature, °C	~ 1350
average change of temperature during one revolution (cycle) of the ring, °C	100
number of cycles per running time	$2 \cdot 10^6$

Reactor vessel:

height, m	9.5
outside diameter, m	32
inside diameter, m	16
pressure of gas medium inside vessel, MPa	0.095

Reactor Operation [2]. Continuous rotational motion of the supporting annular rotating platforms, with the masonry of graphite blocks installed on them, is effected with electric drives due to the friction coupling of the driving wheels with the bearing surfaces of the platforms. As a result of this, every part of the ring of a graphite brick fulfilling the role of coolant passes through the core, the neutron cutoff zone, and the technological zone. In the core, the nuclear fuel contained in the graphite blocks enters into a chain fission reaction, is heated up, and heats up the graphite. During transit through the core, the graphite is heated up by approximately 100°C on the average, and reaches the maximum temperature, for example 1350°C, sufficient for the efficient transfer of heat by radiative heat emission.

The moving fuel version, in contrast from the fixed fuel version (also possible in GROT) is accepted because it provides a lower temperature to which the fuel must be heated up during operation of the reactor, and also because of the tendency to reduce its recharging to a minimum. The period between rechargings in this case coincides with the service lifetime of the conversion technological tubes of $\sim 90-100 \cdot 10^3$ h, i.e., approximately 10-11 years. The disposal of the fuel over the whole annular circuit of movement of the solid coolant ensures the necessary running time of the reactor.

In the neutron cutoff zone, the chain reaction in the nuclear fuel and the subsequent heating up of the graphite during rotation of the annular rotating platforms cease. In the technological zone, the heated graphite transfers the heat accumulated in it by means of radiative emission to the walls of the technological channels, along which the working medium is moving, and the graphite itself is cooled (Fig. 3).

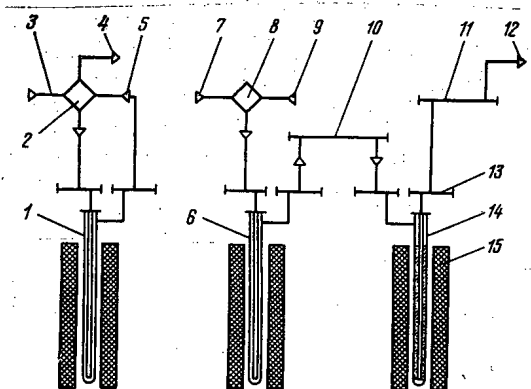


Fig. 3

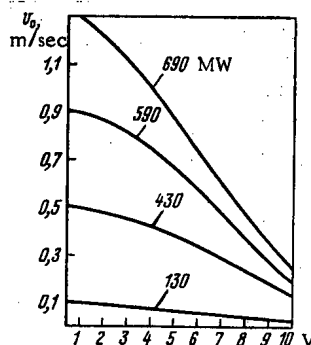


Fig. 4

Fig. 3. Diagram of the movement of the working medium through the technological zones of the reactor facility: 1) evaporative channel; 2) drum-separator; 3) feed water; 4) saturated steam (in the steam superheater); 5) steam-water mixture; 6) steam-gas channel; 7) superheated steam (from the steam superheater); 8) steam-gas mixer; 9) natural gas after sulfur purification; 10) distributive collector; 11) composite collector; 12) conversion product offtake; 13) grouped collector; 14) conversion channel; 15) solid coolant brickwork.

Fig. 4. Distribution of the optimum velocities of motion of the ring of solid coolant with $T_{\max} = 1450^\circ\text{C}$ and with a conversion tube temperature $T_t = 850^\circ\text{C}$.

The feed water, at a temperature of 300°C and a pressure of 10.65 MPa, is fed into the evaporative channels; there it is partially evaporated and then directed into the drum-separator, where the saturated steam is separated from the water. The returned water is mixed with the feed water and again enters the evaporative channels, the saturated steam is directed into the steam superheater of the technological part of the facility, where it is superheated up to 482°C, and then it is mixed with methane. The steam-gas mixture at 4 MPa and 370°C is directed from the mixer into the channels of the steam-gas mixture preheater, whence it enters the distributing collectors of the conversion zone. The temperature of the steam-gas mixture reaches 525°C. From the distributive collectors the heated steam-gas mixture is directed into the steam conversion channels in which a catalyst is located. The products of the catalytic conversion of natural gas at 835°C enter the composite collector and then go on to the second conversion stage. The wall temperature of the conversion channels, made from centrifugal cast tubes (an alloy of the type 45Kh25N20S2), which are used in the tubular furnaces of ammonia production, does not exceed the permissible limits of 950°C.

In the structural layout of the reactor facility being considered, the graphite structures, technological channels, and the thermal insulation of the reactor vessel are located in the high-temperature zone (~1000°C). The actuator mechanisms and equipment, and also the supporting ring-shaped rotating platforms of the solid coolant masonry, are taken out into the low-temperature zone (150-200°C), i.e., they are located close to the bottom of the reactor vessel cooled by water. The electrical part of the actuators are brought out from the reactor vessel into the servicing compartment. This considerably facilitates the working and servicing conditions of the running part of the reactor.

The satisfactory specific heat, excellent thermal conductivity, and high degree of blackness with the necessary fire resistance makes efficient the use of graphite as a coolant in the conditions of heat transfer by radiative heat exchange at 1000°C achieved in GROTT.

The use of graphite as the coolant in a high-temperature power-technological reactor has many advantages, the principal ones of which are the following:

1. The inert gas medium filling the reactor vessel can have any arbitrarily low pressure, right down to vacuum, which:

allows the use for the reactor facility of a low-pressure steel vessel, the construction of which has been assimilated into Soviet reactor construction (for example, the vessel of the RBMK type of channel reactor);

significantly reduces leakage of the gaseous inert medium and radioactive fission products from the reactor vessel;

considerably facilitates the assurance of radiation safety in the case of accidental depressurization of the reactor vessel;

makes it possible to have a pressure gradient between the working medium of the technological circuit and the gas medium filling the inside volume of the reactor vessel, directed from the reactor, and this excludes the entry of radioactive fission products into the technological circuits.

2. The proposed methods of moving the solid coolant ensure its return to the reactor core for repeated heating up at high temperature, which eliminates nonproductive heat losses, due to the necessity for reducing the coolant temperature (when using convective heat exchange), and rids of the solution of the complex problem of designing a system of heat-exchanger equipments and gas blowers for carrying away the heat from the core and transferring it at a permissible temperature to the technological process.

3. Engineering solutions, verified in the production of ammonia in the chemical industry, can be used.

Neutron-Physics Characteristics of GROTT. We shall mention the most significant of them [2, 3, 4]. One of the most valuable qualities of the high-temperature route on the whole is the possibility of extending the nuclear power fuel base by the use of the ^{232}Th - ^{233}U cycle. As is well known, the formation of the intermediate product ^{233}Pa with a long half-life $T_{1/2} = 27$ days and a thermal neutron absorption cross section $\sigma_a = 43$ b is extremely important. The buildup of ^{233}Pa is proportional to the power level, and the capture by it of a neutron leads to a double loss: ^{233}Pa is lost - the potential nucleus of ^{233}U after decay with intensity $\lambda_{\text{Pa}} N_{\text{Pa}}$, and also a neutron which, with a finite probability, could form a ^{233}U nucleus. The necessity for reducing capture leads to a limitation of the specific power of HTGR and, consequently, to a large core size. This creates difficulties when designing reactor systems of this type with a high unit capacity.

In GROTT, the concentration of radioactive products, including ^{233}Pa , because of the fuel circulation is reduced with respect to the length of the movement channels: overall and through the core, i.e., by approximately a factor of 10. This circumstance can be utilized in two ways: either to increase the specific power, or the breeding factor for the same specific power.

Similarly, ^{233}Pa is reduced (in the same ratio, i.e., approximately by a factor of 10) and the concentration of precursors ^{135}Xe and $^{149}\text{Sm} \rightarrow ^{135}\text{I}$ and ^{149}Pm , respectively. In the case of ^{135}Xe , this leads to a reduction of its concentration by a factor of ~ 2.5 , a reduction of the neutron poison capture in ^{135}Xe and, consequently, to an additional increase of the breeding factor, a reduction of the steady-state poisoning from ~ 5 to 3% , which causes an increase of the running time by $\sim 10\%$ and facilitates control of the reactor.

In the case of movement of the solid coolant with the fuel along the core, its burnup takes place on the average along the line of movement in the neutron flux. This effect, which can be called self-recharging, leads to an increase of the running time by $\sim 15\%$ by comparison with the case of the nonmoving fuel.

There are no rigid thermophysical limitations on the thickness of the graphite zone (with and without the fuel) in the solid coolant in GROTT. This gives the possibility of achieving large-scale heterogeneity, which is optimum with respect to neutron physics and which contributes to the achievement of an economically feasible aim - the use of a low-enrichment fuel.

The fuel is disposed over the whole coolant movement circuit, which means that the synchronous charging and running time of the reactor is increased. This might be supposed to be a drawback of the GROTT; however, if one bears in mind the prospect of increasing the unit capacity, and also the specific energy intensity of the core, then this characteristic makes it possible to choose the optimum duration of the running time. In contrast from this case, frequent fuel charging of the reactor with nonmoving fuel would cause considerable deviations of the parameters from the optimum values.

Among the less important, but characteristic features of GROTT, the following are included:

In the outer technological part there is a powerful γ -emission from fission products, which can be used for carrying out radiation-chemical processes. In particular, in the conversion of natural gas using the GROTT with a capacity of 500 MW, the reacting mixture in the conversion tubes with a diameter of 90×130 mm absorbs the energy of the γ -field equal to $1.5 \cdot 10^{18}$ eV.

A considerable fraction of the delayed neutrons are carried away into the outer part. With a core size along the line of movement of $\sim 5-8$ m and a velocity of movement of the ring of ~ 0.5 m/sec, the neutron removal amounts to $\sim 30-40\%$. This, taking account of the strong negative temperature coefficient of reactivity inherent in GROTT, does not create difficulties in the reactor control. In addition, in the outer part there is a certain undesirable submultiplication of neutrons. These effects, as calculations show, are insignificant.

Optimization calculations are interesting, for example, to find the distribution of the linear velocity of motion of the ring, which will ensure an identical maximum temperature at the outlet from the core (Fig. 4).

The calculations showed that the power distribution, the power itself, and its nonuniformity do not vary in the case of the optimization method considered, although the velocity of motion of the rings can vary considerably, for example by a factor of 5 or more. Physically, this is explained simply: The peripheral rings for "pulling" the temperature at the core outlet up to T_{\max} (they are moving in lower neutron fluxes) must be moving more slowly. Therefore, they carry away less heat, i.e., $\Delta T v$ is found to be constant. This factor can be used conveniently for generating a uniform temperature field in the heat exchange zone when carrying out technological processes.

Figure 5 shows the power distribution W along the rings at 1-m height of the solid coolant with different nonuniformity W_k , for a reactor power W_n and a thickness of the fuel layer $H=1$ cm and $H=3$ cm, with a velocity of motion of the ring of 0.5 m/sec.

Thermotechnical Characteristics of GROTT. At the basis of the thermotechnical processes taking place in the reactor, there lie well-studied processes of thermal conductivity, heat transfer by thermal radiation, and convective heat exchange in the technological channels. The necessity for the joint consideration of these processes, the intrinsic heterogeneity of the heat-transfer system, the multiple linking of the heat-transfer scheme, and the limited possibilities of the computer do not allow the well-known mathematical methods to be used for solving this problem without any simplifications of the model of the heat-transfer system. Therefore, a combination of procedures was developed for the thermotechnical calculation of GROTT. In particular, the method of calculation of the multiring system is based on the partial homogenization of the structure of the moving graphite

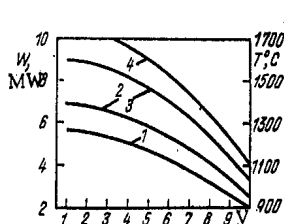


Fig. 5

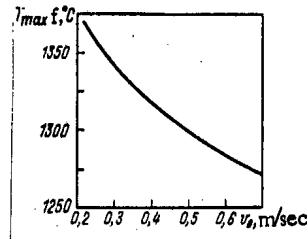


Fig. 6

Fig. 5. Power distribution of the rings of solid (readings of rings from central): 1) $H=1$ cm; $T_t=850^\circ\text{C}$, $W_k=0.767$, $W_n=430$ MW; 2) 1 cm, 550°C , 0.772, 590 MW, respectively; 3) 3 cm, 850°C , 0.770, 690 MW, respectively; 4) 3 cm, 550°C , 0.774, 820 MW, respectively.

Fig. 6. Effect of velocity of rotation of the middle ring on the maximum fuel temperature.

ring with the fuel elements. The homogenization principle was also used when considering the radiative heat exchange between the graphite ring and the series of technological channels (introduction of the average heat fluxes, coefficient of light irradiance, temperature of the surface of the technological channels, etc.).

The major part of the accumulated heat within the confines of the core after one revolution of the rings is in the fuel (70–80%). Therefore, the use of the principle of moving sources of heat release, distributed uniformly over the volume and moving, improves the heat transfer to the solid coolant.

The size of the core is determined from neutron-physical calculations. The low specific power, generated by the low heat-transfer coefficient by radiation ($50\text{--}300$ W/m^2) leads to a considerable size for the heat exchanger and the facility as a whole: The diameter of the middle ring amounts to 25 m.

It follows from Fig. 6 that with increase of v_0 , preheating of the coolant is decreased, which leads to a reduction of $T_{\text{max}f}$. The same relationship is observed also for the thickness of the graphite ring δ . However, for $\delta > 100\text{--}150$ mm, the value of $T_{\text{max}f}$ remains constant. This is explained by the fact that with a large thickness the middle of the graphite ring participates in the transfer of heat. Variations of v and δ only insignificantly affect the length of the heat-exchanger.

Although according to thermotechnical considerations it is desirable to increase the velocity of movement, and also the height of the ring, their final choice is dictated by the neutron-physics characteristics of the core and the mechanical stability of the rotating graphite brickwork.

The following thermotechnical characteristics of the facility and its technological part were obtained by the method of calculation of the multiring system for the starting data:

Length of core together with the neutron cutoff bricks, m	11
Thickness of graphite ring, m	0.25
Angular frequency of rotation of graphite rings, r/min	0.36
Intensity of internal heat release sources, referred to the fuel volume, W/m^3	$1.29 \cdot 10^7$
Coefficient of nonuniformity of heat release:	
along the core radius	1.16
over the height of the core	1.12
Maximum permissible wall temperature of the technological channel, $^\circ\text{C}$	950

The temperature and the thermal fluxes in Table 1 are given for the middle ring in cross section over the height, where the fuel temperature reaches the maximum value.

The calculations of the temperature fields in the moving brickwork, based on the homogenized model, were refined by taking into account the heterogeneous disposition of the fuel. The maximum temperature of the fuel elements and graphite amounted to 1365 and 1315°C , respectively, and the maximum nonuniformity of the fuel element and graphite temperature was 85 and 124°C . A comparison of the calculations by the procedures with a heterogeneous disposition of the fuel and with a homogenized fuel layer showed that consideration of the heterogeneous disposition leads to an increase of the maximum fuel temperature by 40°C .

TABLE 1. Thermotechnical Characteristics of the Zones of the Technological Part of the Facility

Parameter	Reactor zone		
	evap- ora- tive	pre- heater (gas mixt.)	conver- sion
Power of zone, MW	248	37,4	196,6
Av. thermal flux, kW/m ²	150	65	53
Length of zone, m	25	5	37
Pressure of medium, MPa	11	4	4
Temp. of substance at inlet (outlet) to zone	300 (314)	370 (525)	525 (830)

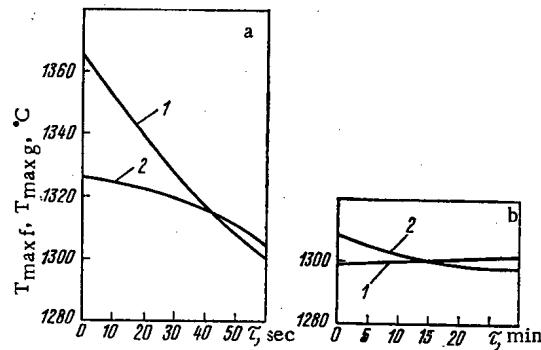


Fig. 7. Change of maximum temperature of fuel (1) and graphite (2) in a small (a) and large (b) time after shutdown of the reactor.

The nonuniformity of the heat-transfer coefficient by radiation around the perimeter of the technological channel can cause nonuniformity of the temperature in it. The radiative heat exchange in the system of bodies (graphite ring - row of technological channels) was calculated by dividing the system of bodies into sections. For each section the equation of the radiative heat exchange with the adjacent sections was written. Thus, the problem was reduced to the solution of a system of linear equations relative to the temperature of the sections.

The maximum temperature nonuniformity over the perimeter of the conversion tubes, located in the worst temperature conditions, on the outside surface amounts to 24°C and on the inside surface -14°C. The reactor with a solid coolant has a large thermal inertia. This facilitates obtaining the necessary rate of heating up and cooling of the reactor units both in the case of planned startups and shutdowns, transition from one power level to another, and also in emergency situations.

Using the method of calculating the nonsteady thermal conductivity in a region with arbitrary geometry, a calculation was performed of the heating-up of the graphite brickwork for the case when the heat is not removed from the masonry. This situation can arise in the case, for example, of an accidental stoppage of the rotation of the annular brickwork of graphite blocks. The temperature field in this brickwork at the instant of its passing the edge of the core is assumed as the initial distribution. It was supposed that the graphite rings are stopped instantaneously. Figure 7 shows the behavior in time of the maximum temperature of the fuel and graphite. At first, the fuel temperature falls because of the outflow of heat into the graphite. Over 15 min, it is equalized in the graphite masonry, and then it starts to increase, over 5 h it reaches the initial maximum value, and over 10-12 h it reaches the maximum permissible of 1400°C. Hence, it follows that there is a large time reserve (10-12 h) for carrying out the various measures to eliminate the consequences of an emergency shutdown of the rings.

The slow rate of heating up of the graphite masonry due to residual heat release can be used for organizing the reactor cooling process by means of a small number of revolutions of the graphite rings (the time between the first and second revolutions of the graphite rings amounts to 13 days).

The computational thermophysical investigations carried out, experiments and test-rig tests of one of the possible variants of the GROTT concept, confirmed the technical feasibility and the efficiency of high-temperature heat transfer from the nuclear fuel to the technological users.

LITERATURE CITED

1. N. A. Dollezhal', N. D. Zaichko, and A. M. Alekseev, *At. Energ.*, **43**, No. 6, 432 (1977).
2. I. L. Chikhladze, *Problems of Nuclear Science and Technology. Series Atomic-Hydrogen Power Generation and Technology [in Russian]*, Issue 2 (1979), p. 101.
3. V. T. Zhukov, R. P. Fedorenko, and I. L. Chikhladze, *Thermal Problem for a Nuclear Reactor with Solid Coolant. Preprint of the Institute of Applied Mathematics, Academy of Sciences of the USSR [in Russian]*, No. 51 (1981).
4. I. Ya. Emel'yanov, V. T. Zhukov, and I. L. Chikhladze, *Problems of Nuclear Science and Technology. Series of Atomic-Hydrogen Power Generation [in Russian]*, Issue 2(12) (1982), p. 29.

SYNTHESIS OF A SYSTEM FOR STABILIZING REACTOR
POWER AND ENERGY DISTRIBUTION ON THE BASIS
OF LATERAL IONIZATION CHAMBERS

I. Ya. Emel'yanov, L. N. Podlazov,
A. N. Aleksakov, E. V. Nikolaev,
V. M. Panin, and V. D. Rogova

UDC 621.039.515

A current task with the power reactors in nuclear power stations is to upgrade the stability and working parameters by upgrading the automatic controls [1]. One way of improving reactor stability is to use branched automatic stabilization systems for the power distribution. The current approach of designing such systems involves introducing a certain number of local automatic controls (LAC) working with signals from transducers within the reactor and uniformly distributed over the core [1, 2]. However, it has been shown [3-5] that it is possible to improve the stabilizing performance of an automatic control by optimizing the spatial structure of the control system by using the asymmetry of the neutron-balance operator [6, 7]. It has been suggested [4] that the asymmetry principle should be combined with zone control in constructing a power-distribution stabilization system. This suggestion was extended in [5], where it was shown that the optimum location for the rods and transducers as regards stabilizing performance is characterized by placing the rods closer to the center of the reactor and the transducers at the periphery. As a result, it became clear that a high-performance stabilization system can be based not only on transducers within the reactor but also on lateral ionization chambers (LIC). Such a structure is technically attractive because of the higher reliability and wide dynamic range of LIC by comparison with transducers within the reactor.

Here we consider the engineering synthesis of a zone-asymmetric stabilization system for the radial and azimuthal power distributions that also provides overall power regulation by means of LIC. A difference from [5] is that a criterion is used for minimum spatial dispersion in the neutron-flux deviations in tracking reactivity perturbations:

$$D(t) = \int_{\Omega} \varphi^2(r, t) dr,$$

where $\varphi(r, t)$ is the dimensionless neutron-flux deviation from the stationary value.

The control system is synthesized by the method of [8], according to which the synthesis is divided into two stages. In the first stage, one analyzes the system viability at constant (nominal) power under conditions of instability in the power distribution and with technological perturbations. The second stage includes examining the operation in emergency situations requiring rapid controlled power reduction.

Translated from *Atomnaya Énergiya*, Vol. 56, No. 1, pp. 11-15, January, 1984. Original article submitted February 16, 1983; revision submitted May 11, 1983.

TABLE 1. Optimum Values of the Rod-Location Radius and Angle of Rotation Relative to the Chambers for Three, Four, and Five Regulators: the Values of R Are Given as Fractions of the Extrapolated Core Radius

n	R	γ
3	0,38	22°
4	0,37	17°
5	0,38	11°

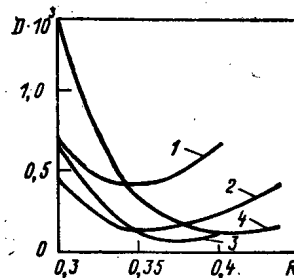


Fig. 1. Dependence of the dispersion of the location radius of the rods in the LAC-LIC system with various angles of displacement of a rod relative to a transducer for three regulators: 1) $\gamma = 0^\circ$; 2) $\gamma = 15^\circ$; 3) $\gamma = 22^\circ$; 4) $\gamma = 30^\circ$.

In the first stage, the control system is synthesized on the basis of a linear two-dimensional model for the spatial neutron kinetics [8]. The neutron flux is described by a linearized diffusion equation with allowance for one group of delayed neutrons and two power feedbacks (fast and slow) in the form of first-order links. The rapid power feedback incorporates effects from the fuel temperature and steam content, while the slow one is related to the graphite temperature and xenon poisoning. The control is provided by rods at discrete points following a relay law. Galerkin's method [9] is used. The calculations incorporated 17 harmonics of the form

$$\psi_{ij}(r, \theta) = J_j \left(\frac{\alpha_i}{R_0} r \right) \begin{cases} \sin j\theta \\ \cos j\theta \end{cases},$$

where $J_j(z)$ is a Bessel function of the first kind and α_i are the solutions to the equation $J_j(z) = 0$. The number of harmonics was chosen on the basis of attaining an adequate accuracy.

A serious problem arises over choosing the form of the perturbation, since this substantially influences the results. Real perturbations vary in spatial form and occur with different rates. To select a representative set of perturbations, one needs information on the perturbations characteristic of a given reactor, whose features are related to ones in the technological scheme and the detailed specifications for power control for a reactor working in a power system. The most reliable source of such data comes from experience in reactor operation. At present, statistical data are lacking on the actual frequencies and intensities for perturbations of various spatial forms in existing reactors; and it is even more difficult to obtain such information for reactors under design. To overcome this uncertainty and to synthesize a system having sufficient practical performance, we use an approach based on a time-stepped perturbation uniformly distributed over the amplitudes of all the harmonics incorporated into the solution:

$$\Delta k_p = \sum_{i,j} \psi_{ij}(r) 1(t).$$

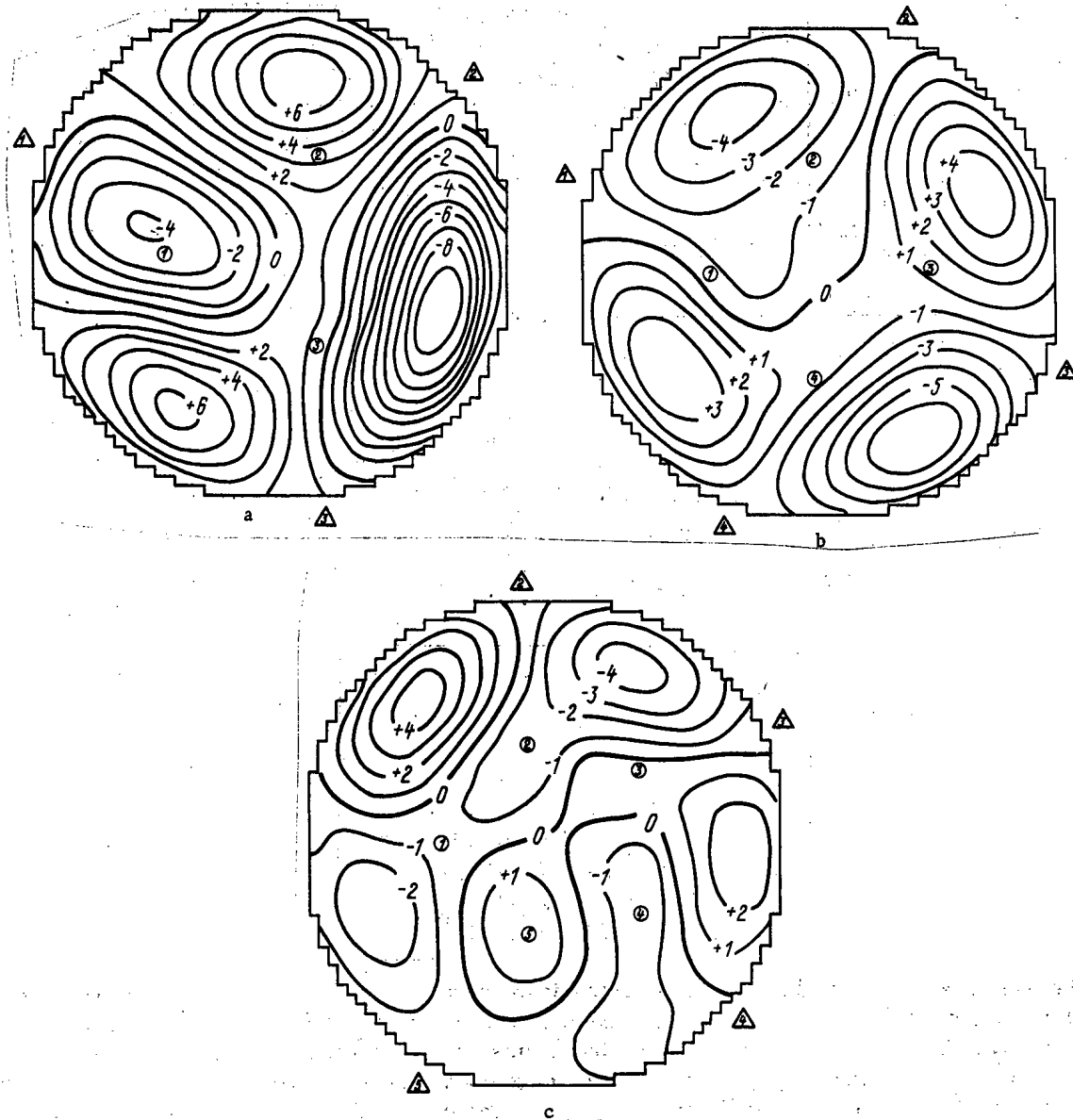


Fig. 2. Spatial form of the inherent motion for the power distribution in a reactor fitted with an LAC-LIC system: a-c) three, four, and five regulators correspondingly; O) rod in LAC-LIC system; Δ) transducer in LAC-LIC system; —+1—) line of equal deviation in the energy distribution from the initial state in %.

The optimum control-rod disposition is found from the condition for minimum D at the instant when the relay zone-asymmetric regulator system has tracked the initial perturbation and is going over to a sliding mode of operation. Figure 1 shows the dependence of D on the rod location radius R for various angles of displacement of the rod relative to the transducer γ for three rod-transducer pairs (the curves for larger number of regulators are similar to these). There is a pronounced minimum of each curve in Fig. 1. Table 1 gives the optimum values of R and γ for three, four, and five regulators. As the number of regulators increases, the angle of displacement of a rod relative to a transducer decreases, as does the significance for optimizing the response to a perturbation. There is a minimum in D as R varies because the system does not bring the mean power back to the initial value on taking up the unbalance in the regulator channels in the insensitive zone on tracking the perturbation when the rods are displaced closer to the transducers, i.e., to the edge of the core. Conversely, displacing the rods towards the center of the core causes mean-power overshoot.

Different results are obtained as regards the angle γ between the rod and transducer on synthesizing the system from the criterion for minimum in the maximal real part of the root of the characteristic equation for the dynamics of the radial and azimuthal energy distribution [5] and from the criterion for minimum spatial dispersion. One gets a smaller angle if one incorporates into the synthesis not only the stability but also the transient response.

These results have been obtained from a linear reactor model. It is necessary to use a nonlinear two-dimensional digital model in a detailed examination of the viability of the LAC-LIC system under conditions of emergency controlled power reduction. The reason arises from the characteristic difficulties encountered in performing tests on power-station reactors: There are nonstationary states related to extensive changes in the parameters, which are particularly difficult for the automatic control, and which are extremely undesirable to produce artificially for experimental purposes, since they involve large loads of all the main equipment. However, it is necessary to be completely convinced that the automatic system will perform its functions reliably in a real emergency. The only possibility is to synthesize a system with allowance for all the states that have to be provided for with a model that accurately reproduces these states. Such a model has been realized with a BESM-6 computer. The model equations contained 540 nodes and described the nonstationary neutron-physics processes in the diffusion approximation, the core thermodynamics, including convective heat transfer and the formation of steam, the changes in xenon and iodine concentrations, and the operation of the control systems on the basis of the characteristics of the control apparatus and effecters. The calculated and experimental values were compared for RBMK-1000 reactors; particularly in order to check the adequacy of the model, and the agreement was good [8].

The stabilizing behavior is characterized by the times involved in the residual deformations in the power distribution during prolonged operation in the steady state. The viability of the LAC-LIC system in a stabilization mode was examined with this model. The reactivity coefficients were as follows in the calculations: $\alpha_{\varphi} = 0.02025$; $\alpha_T = -0.9 \cdot 10^{-5} \text{ 1/}^\circ\text{C}$; $\alpha_c = 5.5 \cdot 10^{-5} \text{ 1/}^\circ\text{C}$ (these correspond approximately to the states of the reactors in the first and second units of Leningrad Nuclear Power Station at the present time). The purpose of the calculation was to identify the spatial form of the inherent motion in the energy distribution together with the time characteristics under conditions of prolonged maintenance of stationary power by the LAC-LIC system in the absence of other controls. Pulsed reactivity perturbations to the initial state were introduced at the start of calculations (two or three rods were displaced by about $\pm 0.5 \text{ m}$ in the intervals between the regulators). Over a sufficiently long interval, the traces of the initial perturbation die away and one identifies the inherent distribution motion.

The results show that the period of rising amplitude in the inherent motion for the LAC-LIC system with three regulators is about 30 min. Figure 2a shows the spatial form of this motion. The motion in a reactor with four regulators is determined in the main by the second azimuthal harmonic, and the period is about 50 min (Fig. 2b). A five-zone LAC-LIC system has even better stabilizing performance, but as with three regulators, it is difficult to identify the predominance of any one harmonic (Fig. 2c). The period was estimated as several hours, i.e., the LAC-LIC system with five regulators is close in performance to the seven-zone LAC system with transducers within the reactor [2].

It was found that there was no objection to increasing the number of LAC further on the basis of a study of the performance of the LAC-LIC system for stabilizing the distribution in the steady state and also from an analysis of the response of the system to perturbations. However, calculations on the period of the residual motion indicate that there will be no increase in stabilizing performance from using more than seven LAC. A system consisting of seven regulators completely stabilizes the radial and azimuthal distributions with the above reactivity coefficients. Figure 3 shows the dependence of the residual-deformation time constant on the number of regulators in the LAC-LIC system.

Nevertheless, improved overall performance is produced in the rods included in the power control, and this is favorable from the viewpoint of emergency power reduction in individual parts of the main equipment. Of course, all the requirements of the nuclear safety rules are met. Final choice of the LAC-LIC system structure is based not only on the calculations but also on the requirement for maximum possible simplicity in realization. In the present case, the structure of the automatic-control system on the RBMK-1000 allows very simple transfer to an LAC-LIC system, since the signal from each of the chambers is processed by an individual amplifier, in which it is simultaneously subtracted from the power-transducer signal [9]. The RBMK-1000 is fitted with two automatic controls (main and reserve) with four chambers in each, which are located virtually uniformly in azimuth [9]. Under these conditions, it is clear that one should implement an LAC-LIC system with eight individual regulators.

The operation of an eight-zone LAC-LIC system under nonstationary conditions was considered by reference to emergency power reduction on emergency shutdown in the main circulation pump (MCP) in one of the circulation loops. When the MCP shuts down, the circulation rate in one half of the reactor decreases and the steam content increases, and on account of the steam effect on the reactivity a perturbation is produced in this half that can cause an increase in the neutron power. To provide normal conditions for fuel-pin cooling under

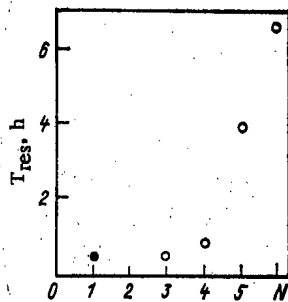


Fig. 3

Fig. 3. Dependence of the residual-deformation time constant T_{res} on the number of regulators N : ●) value of T_{res} in the presence of automatic control (τ_{01}).

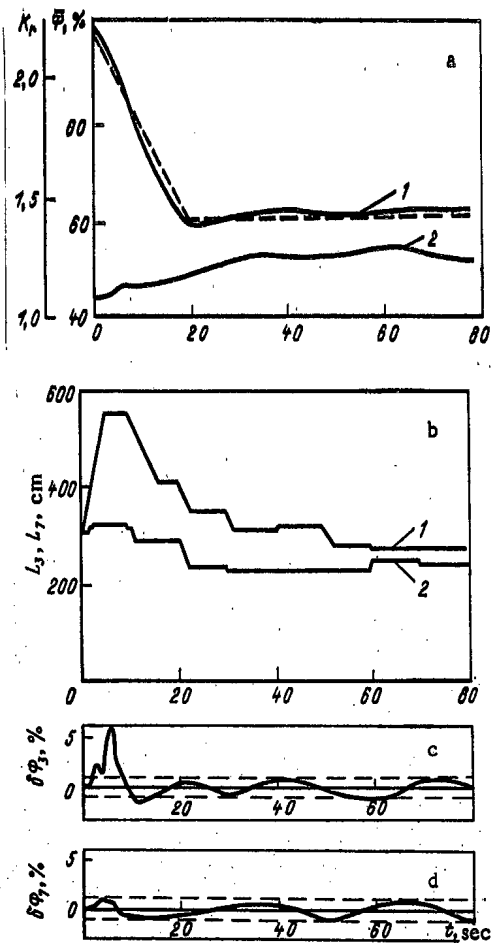


Fig. 4

Fig. 4. Transience in MCP shutdown mode: a) behavior of the neutron power $\bar{\Phi}$ and nonuniformity coefficient for the radial distribution K_r : 1) $\bar{\Phi}$; 2) K_r ; ----) setting; b) rod position in LAC-LIC system in left half L_3 and right half L_7 of reactor: 1) L_3 ; 2) L_7 ; c and d) unbalance in the LAC-LIC system channel in the left half $\delta\phi_3$ and the right half $\delta\phi_7$ of the reactor correspondingly; ----) boundary of the insensitive zone.

such a situation one has to reduce the power at a rate of 2%/sec to the level of 60% of the nominal value, while maintaining the energy distribution unchanged. Figure 4 shows the transience in this state as obtained with the nonlinear digital spatial dynamic model. Parts c and d of Fig. 4 give the unbalances in the LAC-LIC system channels in different halves of the reactor. The unbalance in the channel in the half with the switch-off MCP rapidly but briefly passes outside the limits of the insensitivity zone. The unbalances in the LAC-LIC channels in the opposite half remain virtually within this zone throughout the transient response. The LAC-LIC system copes successfully with this perturbation and provides a power reduction uniform over the reactor. The performance of the control rods in the LAC-LIC system in this state is sufficient: The rods remain in the working range throughout the transient response.

This study of synthesis of a zone-unsymmetrical system has shown that it is possible to produce a highly effective system for stabilizing the power distribution on the basis of LIC, which have high reliability and a wide dynamic range. Increasing the number of regulators to more than seven or eight is undesirable, since beyond this limit there is virtually no more increase in the stabilization performance. A five-zone LAC-LIC system is comparable in stabilizing performance with a seven-zone LAC as regards the residual-deformation growth time. Synthesis of an LAC-LIC system provides a system corresponding to the set of practical specifications.

LITERATURE CITED

1. I. Ya. Emel'yanov et al., *At. Energ.*, **49**, No. 6, 357 (1980).
2. I. Ya. Emel'yanov et al., *Nuclear Science and Engineering, Series Reactor Physics and Engineering [in Russian]*, Issue 1(5), 3 (1979).
3. A. M. Afanas'ev and B. Z. Torlin, *At. Energ.*, **43**, No. 4, 243 (1977).
4. I. Ya. Emel'yanov et al., *ibid.*, **46**, No. 2, 82 (1979).
5. I. Ya. Emel'yanov et al., *ibid.*, **47**, No. 6, 370 (1979).
6. D. Wiberg, *Nucl. Sci. Eng.*, **27**, 600 (1967).
7. I. S. Postnikov and E. F. Sabaev, *At. Energ.*, **26**, No. 1, 56 (1969).
8. I. Ya. Emel'yanov et al., *ibid.*, **53**, No. 5, 301 (1982).
9. I. Ya. Emel'yanov et al., *ibid.*, **48**, No. 6, 360 (1980).

ANALYSIS OF THE STATISTICAL ERROR
AND OPTIMIZATION OF CORRELATION FLOW METERS

B. V. Kebabze

UDC 681.12:621.039.534

Correlation methods are used increasingly to measure the coolant flow rate in nuclear power plants, making use of different kinds of inhomogeneities in the flow and employing appropriate sensors [1-6]. The shift of the maximum of the cross correlation function (CCF) along the time axis is the directly measurable parameter in this case. An important advantage of the correlation method is that it is not sensitive to a change in the conversion ratios of the sensors. One drawback of the method is the relatively long measuring time due to the need to carry out statistical processing of random signals. The error caused by the statistical scatter of the positions of the correlation maximum along the time axis is considered in this paper. This error appears regardless of the form of coolant and sensor, depends on the frequency properties and degree of correlation of the signals, and determines the measuring time necessary to obtain the required accuracy; from the practical point of view it is important to make a substantiated reduction of this time.

Derivation of Relations for the Estimation of the Statistical Error. Unlike the case of the amplitude error, which has been discussed in detail in [7], methods for the estimation of the time error in correlation measurements have not been developed adequately. The computational relation obtained in one paper on this subject [2] is applicable only to a partial form of statistical characteristics. The correlated nature of the amplitude errors is obtained in the form of a functional dependence on the total amplitude error of the CCF.

At the same time, it is not difficult to show that for completely correlated signals the time error of the position of the maximum is insignificant and easily removed for any large amplitude error. As an example, we consider identical signals $x(t) = y(t)$ which are not shifted in time. When cyclical notation is used for the realization of a random process determined by the condition $x(t+T) = x(t)$, the following relation is satisfied:

$$\frac{1}{T} \int_0^T [x^2(t) - x(t)x(t+\tau)] dt = \frac{1}{2T} \int_0^T [x(t) - x(t+\tau)]^2 dt = [\hat{R}(0) - \hat{R}(\tau)] \geq 0.$$

Here $\hat{R}(0)$ and $\hat{R}(\tau)$ are estimates of the correlation function (CF). Thus, in this case $R(\tau)$ has a maximum at $\tau = 0$ without regard for the dependence on the amplitude error of the estimate. The absence of a shift along the time axis is due mainly to the fact that the amplitude errors at close points of the CF are not independent but are cross-correlated. This subsequently allows the shape of the correlation peak in the absence of uncorrelated noise to be assumed to be approximately constant, only random variations of the amplitude being taken into account. Similar discussions can be carried out for the case of pure delay between completely correlated identical signals.

Uncorrelated noise is the main source of error in the time shift. It is clear from the above that we must separate the components of the signal and the correlation functions into correlated (CC) and uncorrelated (UC) components. The following arguments can serve as the physical basis for this separation. The nearly identical signals from the sensors arise when flow inhomogeneities (of temperature, the velocity profile) pass through the sensors. As follows from the experiment in [3, 5], these inhomogeneities are due mainly to the existence

Translated from *Atomnaya Energiya*, Vol. 56, No. 1, pp. 15-20, January, 1984. Original article submitted May 10, 1982.

of large-scale hydrodynamic formations (vortices) in the flow; the stability of these formations under displacement over a considerable distance ($L > D$, where D is the diameter of the tubing) and the fact that they maintain their spatial orientation are conducive to the formation of identical signals (the correlated component). There are also obstacles to this. Thus, with displacement with the flow some "smearing" of inhomogeneities occurs, as manifested in the damping of high frequencies in the signals. The use of filtration with allowance for the frequency variations during the transfer of perturbations makes it possible to reduce the difference of the signals and to increase the fraction of the correlated component. At the same time, the complex nature of the turbulent motion leads to the appearance of uncorrelated components. The probability exists that a vortex, detected by the first sensor, will break up before reaching the second sensor; new perturbations, which affect only the second sensor, are formed in the segment between the sensors. For vortices recorded by both sensors there exists a statistical scatter of the trajectories, displacement time, and spatial orientation. Local small-scale fluctuations within the confines of each sensor and the noise of the measuring ions within the confines of each sensor and the noise of the measuring channels are additional sources of uncorrelated noise. Thus, the signals of the sensors are represented as

$$\begin{aligned} x(t) &= s(t) + n_1(t); \\ y(t) &= s(t - \tau_{\max}) + n_2(t), \end{aligned} \quad (1)$$

where the noise sources $n_1(t)$ and $n_2(t)$, which are uncorrelated with the value of $s(t)$ and $s(t - \tau_{\max})$ because for the nonideal coincidence of $s(t)$ and $s(t - \tau_{\max})$ because the filters incompletely compensate for the frequency distortions. When the uncorrelated nature of $s(t)$, $n_1(t)$, and $n_2(t)$ is taken into account the autocorrelation and cross-correlation functions of the x and y signals can be represented as

$$\begin{aligned} R_x(\tau) &= R_s(\tau) + R_{N_1}(\tau); \\ R_y(\tau) &= R_s(\tau) + R_{N_2}(\tau); \\ R_{x,y}(\tau) &= R_s(\tau - \tau_{\max}). \end{aligned} \quad (2)$$

Further derivation follows mainly from [8]:

1. Using the well-known expression from [7] for the variance of the estimate of the CCF of random processes with a normal distribution law,

$$\sigma_{\hat{R}_{xy}}^2 = \frac{1}{T} \int_{-\infty}^{+\infty} R_x(\xi) R_y(\xi) + R_{xy}(\xi + \tau) R_{yx}(\xi - \tau) d\xi,$$

taking Eq. (2) into account, and assuming that the length of realization is sufficient for the uncorrelated components of the CCF to vanish, we separate the components of the error of the correlated and uncorrelated components of the CCF:

$$\begin{aligned} \sigma_{\hat{R}_{xy}}^2 &= \sigma_{CC}^2 + \sigma_{UC}^2 = \frac{1}{T} \int_{-\infty}^{+\infty} [R_s^2(\xi) + R_s(\xi + \tau - \tau_{\max}) R_s(\xi - \tau + \tau_{\max})] d\xi + \\ &+ \frac{1}{T} \int_{-\infty}^{+\infty} [R_s(\xi) R_{N_1}(\xi) + R_s(\xi) R_{N_2}(\xi) + R_{N_1}(\xi) R_{N_2}(\xi)] d\xi. \end{aligned} \quad (3)$$

The value of σ_{CC}^2 can be estimated as

$$\sigma_{CC}^2 \leq \frac{2}{T} \int_{-\infty}^{+\infty} R_s^2(\xi) d\xi,$$

while σ_{UC}^2 is the sum of the variances of the uncorrelated components of the CCF:

$$\sigma_{UC}^2 = \sigma_{R_s N_1}^2 + \sigma_{R_s N_2}^2 + \sigma_{R_{N_1} N_2}^2$$

2. We introduce the constraint consisting in the assumption that the functions R_s , R_{N_1} , and R_{N_2} have the same form

$$R_s = S f(\tau); \quad R_{N_1} = N_1 f(\tau); \quad R_{N_2} = N_2 f(\tau); \quad f(0) = 1 \quad (4)$$

This constraint reflects the real situation.

If the form of the functions R_s and R_N (hence, R_x , R_y , and R_{xy} as well) were to differ strongly, this would mean that the measuring channels are loaded with signals that are not informative from the point of view of correlation measurements and that frequency filtration is necessary. Such filtration, which suppresses both low-frequency fluctuation of the parameters and high-frequency noise, is carried out in practice, and as a consequence the frequency characteristic of the signals and the form of the correlation function are formed to a considerable degree by the filters. When Eqs. (3) and (4) are taken into account the dispersions, normalized to the square S^2 of the correlation peak, are

$$\sigma_{CC,0}^2 \leq 2\Phi/T; \quad (5)$$

$$\sigma_{UC,0}^2 = \frac{\Phi}{T} \left(\frac{N_1}{S} + \frac{N_2}{S} + \frac{N_1}{S} \frac{N_2}{S} \right), \quad (6)$$

where $\Phi = \int_{-\infty}^{+\infty} f^2(\tau) d\tau$ is the form factor.

3. The error in the determination of the position of the maximum of the CCF is due to the fact that because of the statistical error of the uncorrelated components of the CCF a peak possessing a random amplitude, randomly displaced from the main peak by an interval Δ along the τ axis, may be superimposed onto the main peak determined by the correlated component. The height of the correlated peak has a scatter in accordance with the relative variance $\sigma_{CC,0}^2$. If by δ_{UC} we denote the amplitude of the random peak relative to S and by δ_C we denote the relative deviation of the amplitude of the main peak, we get the following expression for the estimate of the CCF in the region of the maximum:

$$f_1(\tau) = (1 + \delta_C) f(\tau) + \delta_{UC} f(\tau - \Delta).$$

The origin of the time coordinate has been transferred here to the point τ_{max} ; since the frequency properties of the signals are identical we assume that the shapes of the peaks can be described by the same function $f(\tau)$. Using an expansion up to the quadratic term in the form

$$f_1(\tau) = (1 + \delta_C) \left[1 + \frac{1}{2} f''(0) \tau^2 \right] + \delta_{UC} \left[1 + \frac{1}{2} f''(0) (\tau - \Delta)^2 \right]$$

with allowance for the existence of $f''(0)$ for real random processes, we can easily determine the shift of the maximum

$$\tau_s = \frac{\delta_{UC} \Delta}{1 + \delta_C + \delta_{UC}}. \quad (7)$$

For $\delta_C, \delta_{UC} \ll 1$ we have

$$\tau_s \approx \delta_{UC} \Delta. \quad (8)$$

We determine the variance of τ_s , taking account of the fact that the mathematical expectations of δ_{UC} and Δ are 0:

$$\sigma_{\tau_s}^2 = \iint_D (\delta \times \Delta) p(\delta, \Delta) d\Delta. \quad (9)$$

The subscript UC is omitted here and henceforth $p(\delta, \Delta)$ is the combined probability density, defined in a certain region D . The amplitude of the random maximum and its position along the time axis are statistically independent and, therefore,

$$p(\delta, \Delta) = p(\delta) p(\Delta). \quad (10)$$

For $p(\Delta)$ we have taken uniform distribution in an interval, for which we have chosen the correlation interval

$$\tau_C = \int_0^{\infty} |f(\tau)| d\tau.$$

This choice can be justified by the fact that the probability of one random peak appearing in this interval is fairly high while the number of these peaks is small:

$$p(\Delta) = \frac{1}{\tau_C}; \quad -\frac{\tau_C}{2} \leq \Delta \leq \frac{\tau_C}{2}. \quad (11)$$

The probability density for the amplitude of random maxima can be found, taking account of the fact that the estimates of the correlation functions are asymptotically normal [9]. In the case under consideration the estimate has a zero mathematical expectation and the variance (6). The values of the CCF of correlated process can be considered as a realization of a random process along the τ axis. It is known [7] that the frequency characteristics of this realization are roughly the same as those of the initial processes. The range of the latter is limited by high and low frequencies. As is known [9], for processes with an almost constant spectral density in a limited frequency band the amplitude distribution approaches a Rayleigh distribution as the frequency band decreases.

We apply it for the amplitude of a random maximum with allowance for the symmetry of the distribution:

$$p(\delta) = \frac{1}{2} \frac{|\delta|}{\sigma^2} \exp\left(-\frac{\delta^2}{2\sigma^2}\right). \quad (12)$$

In accordance with Eq. (9) with allowance for Eqs. (6) and (10)-(12) we get

$$\sigma_{\tau_s} = \sqrt{\frac{2}{3} \frac{\tau_C}{2} \sigma} = \sqrt{\frac{2}{3} \frac{\tau_C}{2} \left[\frac{\Phi}{T} \left(\frac{N_1}{S} + \frac{N_2}{S} + \frac{N_1 N_2}{S^2} \right) \right]^{1/2}}, \quad (13)$$

where σ is the relative rms deviation for the uncorrelated components of the CCF. For the particular $N_1 = N_2 = N$ with allowance for the definition of the correlation coefficient ρ ,

$$\rho = \frac{R_{xy}(\tau_{\max})}{\sqrt{R_x(0)R_y(0)}} = \frac{S}{S+N} \quad (14)$$

we get

$$\sigma_{\tau_s} = \sqrt{\frac{2}{3} \frac{\tau_C}{2} \left\{ \frac{\Phi}{T} \left[2 \frac{1-\rho}{\rho} + \left(\frac{1-\rho}{\rho} \right)^2 \right] \right\}^{1/2}}. \quad (15)$$

In solving the optimization problem we consider the relative error $\sigma_r = \sigma_{\tau_s} / \tau_{\max}$; τ_{\max} can be expressed in terms of the basal distance Δz and the average flow velocity: $\tau_{\max} = \Delta z / v_{av}$.

Comparison with Experiment and the Possibility of Optimization of the Parameters of a Correlation Flow Meter. The calculated estimates of the error on the basis of the relations derived were compared with experimental random errors in correlation measurements of the velocities and flows of sodium and air [3, 10]. Low-inertia thermocouples were used as fluctuation sensors in the case of sodium and hot-wire anemometers in the case of air. The distribution law of random signals is nearly normal. During the experiments we varied the basal distance between sensors, the frequency range of the filters, and the measuring time. For each set of these parameters we carried out 100 measurements of 100 CCF and from the results we estimated the relative rms deviations of the position of the correlation maximum which are given in Figs. 1 and 2 with a 90% confidence interval indicated. When correlating thermal noise it is necessary to suppress the low-frequency component arising as a result of the thermal interaction of temperature inhomogeneities with the wall; accordingly, in the experiments we employed a band filter with a tunable central frequency f_0 and an attenuation of 48 dB per octave. In comparing the calculated data with the experimental data we assumed that the frequency properties of the signals are determined completely by the filter, whose frequency characteristic was presented as

$$F(f) = \exp\left\{-\frac{[2\pi(f-f_0)]^2}{2\beta^2}\right\},$$

which corresponds to a normalized correlation function $R(\tau) = \exp\left(-\frac{\beta^2 \tau^2}{4}\right) \cos \omega_0 \tau$. The parameter β was determined in accordance with the given attenuation:

$$\beta = \pi f_0 / 2 \sqrt{\ln 2}.$$

The form factor and the correlation interval were determined from the relations presented earlier and were

found to be equal to $\sqrt{\frac{\pi}{2} \frac{1}{\beta}}$.

Since the sensors were set up in the stabilized segment of the flow, we can justifiably assume that the statistical characteristics of their signals are identical ($N_1 = N_2$) and use formula (15), taking the value of ρ from the experiment. During measurements, over a wide range, of the basal distances and operating frequencies in sodium and air flows it was established [3, 10] that the dependence of ρ on the parameters indicated is approximated well by the expression

$$\rho(\Delta z, K) = C_1 \exp[-(C_2 + C_3 \Delta z) K], \quad (16)$$

where $K = f_0 / v$ (in the calculation the relative error σ_r has been assumed). The results are represented by solid lines in Figs. 1 and 2. The general nature of the dependence of the error on the measuring time corresponds to $1/\sqrt{T}$ (see Fig. 1a, b), which follows from formulas (13) and (15). The calculations also confirm the existence of maxima of the error as a function of Δz for different frequency ranges (see Fig. 2a, b). Fair quantitative

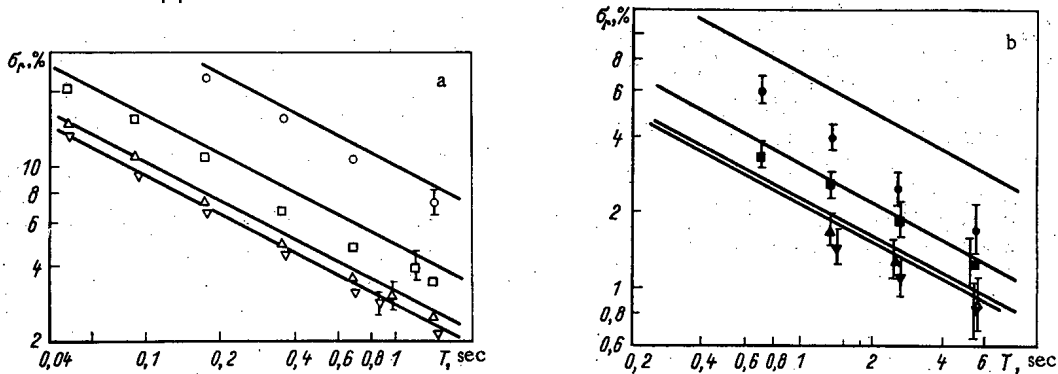


Fig. 1. Relative rms deviation σ_r as a function of the measuring time for air (a) for $v_{av} = 54$ m/sec and $\Delta z = 100$ mm and for sodium (b) for $v_{av} = 5$ m/sec and $\Delta z = 143$ mm: $\circ, \square, \Delta, \nabla$) $f_0 = 100, 200, 300, 500$ Hz, respectively, $\rho = 0.74, 0.64, 0.57,$ and 0.34 ; $\bullet, \blacksquare, \blacktriangle, \blacktriangledown$) $f_0 = 30, 60, 90,$ and 120 Hz, respectively, $\rho = 0.55, 0.45, 0.37,$ and 0.25 .

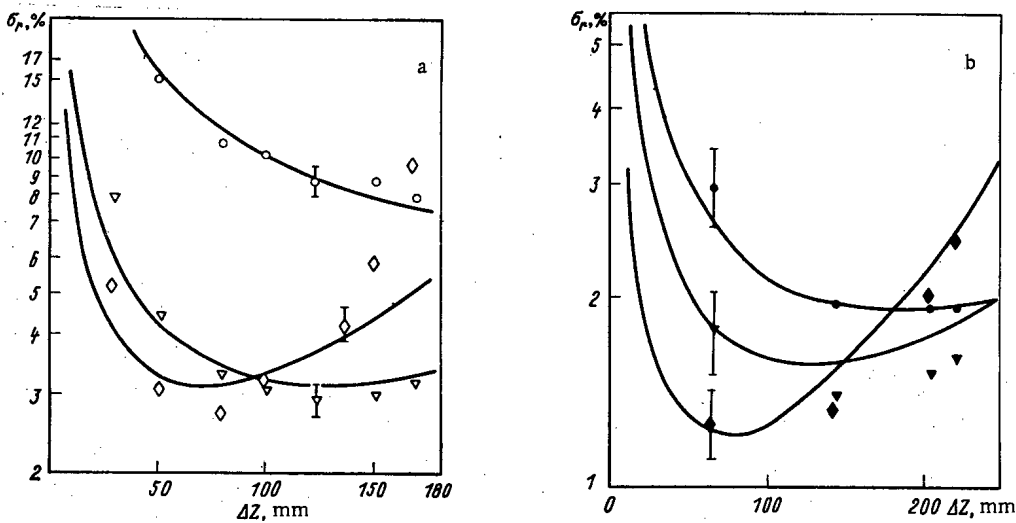


Fig. 2. Relative rms deviation σ_r as a function of the basal distance for air (a) for $v_{av} = 54$ m/sec, $T = 0.68$ sec, $\rho = 1.0 \exp[-(3.57 + 0.72 \Delta z) K]$, $K = f_0 / v_{av} \text{ cm}^{-1}$ and for sodium (b) for $v_{av} = 5$ m/sec, $T = 2.7$ sec, $\rho = 0.9 \exp[-(0.235 + 0.38 \Delta z) K]$, $K = f_0 / v_{av} \text{ cm}^{-1}$; \circ, ∇, \diamond (curves 1, 2, 3) $f_0 = 100, 500,$ and 1000 Hz; $\bullet, \blacktriangledown, \blacklozenge$) $f_0 = 60, 90,$ and 160 Hz.

agreement of the experimental and calculated data is observed over a wide range of frequencies and correlation coefficients ($\rho = 0.1-0.9$). The appreciable discrepancy at $f_0 = 1000$ Hz and large basal distances (curve 3, Fig. 2a) can be explained by the fact that for the given frequency range and distances the real form of the CCF and the values of τ_C and Φ can differ from the same parameters obtained from the characteristics of the filter, owing to a drop in the spectral density of the signal within the filtration band. On the whole, Eq. (15) correctly reflects the nature of the dependence of σ_r on the measuring conditions and can be used to analyze the statistical error and to minimize it.

Once the dependence of the correlation coefficient ρ on the basal distance and the frequency range has been determined on the basis of a small number of measurements, Eq. (15) can be used to calculate the parameters of the optimum correlation flow meter which ensures a minimum statistical error at a given measuring time or a minimum measuring time for a given error. Thus, solving the minimum problem for the function $\sigma_r = \sigma(\Delta z, f_0)$ using Eq. (16), we can easily show that the optimum basal distance $\Delta z_{opt} = 2C_2/C_3$. The corresponding value of $f_{0, opt}$ is found by solving a transcendental equation. On the basis of the values of $C_1, C_2,$ and C_3 obtained experimentally [3, 10] we found the optimum parameters for measuring segments with air ($\Delta z_{opt} = 9.92$ cm, $f_{0, opt} = 711$ Hz, $\sigma_r = 3.06\%$ for $v_{av} = 54$ m/sec, $T = 0.68$ sec) and with sodium ($\Delta z_{opt} = 1.24$ cm, $f_{0, opt} = 1014$ Hz, $\sigma_r = 0.76\%$ for $v_{av} = 5$ m/sec, $T = 2.7$ sec). We note that the optimum values for air lie within the inves-

tigated range of Δz and f_0 and are fairly reliable. The calculations for sodium indicate a need to carry out measurements in the range of high frequencies, which were not encompassed by the experiments of [3, 10], and it may prove necessary to make the approximation relations (16) more exact by taking account of the frequency of the temperature sensors. This enables the optimum parameters to be refined. The optimum basal distance decreases with the damping exponent of the correlation coefficient C_2 , which does not depend on the basal distance and is determined mainly by the intrinsic noise of the measuring channels (measuring lines, amplifiers). Consequently, the range of optimum frequencies shifts to lower frequencies. The tendency of σ_T to vary within the framework of the approximation used for ρ is traced well provided that $C_3\Delta z \gg C_2$. Decreasing Δz when $\Delta z f_0 = \text{const}$ and bearing in mind that $\tau_C, \Phi \sim 1/f_0$, we can easily show that $\sigma_T \sim 1/\sqrt{f_0} \sim \sqrt{\Delta z}$. Obviously, the reduction in the error owing to a decrease in the basal distance and an increase in the frequency should be ensured by the dynamic properties of the sensors. We also point out that the possibility of a given error being attained in a minimum time as a result of optimization also means an improvement in the dynamic characteristics of correlation flow meters operating in a continuous measurement mode. The examples presented here show that the statistical error (1%) employed can be reached in 2-3 sec under the actual conditions of sodium loops. It must be pointed out at the same time that in the optimization of correlation flow meters the criterion of minimum statistical error is not the only criterion. When correlation flow meters are constructed it is necessary to take other factors into account as well, e.g., the relative error of the basal distance, the influence of local distortions of the flow profile, etc.

In conclusion, we point out that, despite the series of constraints and assumptions adopted during the derivation, the relations obtained for the estimation of the statistical error are in fairly good agreement with the experimental data and can be used to optimize the parameters of correlation flow meters. Refinements of the computational technique can involve the choice of the interval for finding the random maximum; the limits of applicability of the derived relations must also be estimated.

LITERATURE CITED

1. R. Gopal and W. Ciaramitaro, *Progr. Nucl. Energy*, 1, No. 2-4, 759 (1977).
2. H. Bazerghi and K. Serdula, *Progr. Nucl. Energy*, 1, No. 2-4, 629 (1977).
3. J. Benkert et al., *Progr. Nucl. Energy*, 1, No. 2-4, 553 (1977).
4. V. M. Selivano et al., *At. Energ.*, 42, No. 1, 49 (1977).
5. B. V. Kebabze et al., *At. Energ.*, 45, No. 1, 30 (1978).
6. P. Bentley, in: *Proceedings of Specialists Meeting on Sodium Flow Measurements in Large LMFBR Pipes*, Bergish Gladbach, West Germany (1980), p. 73.
7. J. S. Bendat and A. G. Piersol, *Measurement and Analysis of Random Data*, Wiley, New York (1966).
8. B. V. Kebabze, *Problems of Atomic Science and Engineering "Nuclear Reactor Physics and Engineering" Series*, No. 3(25), 90 (1982).
9. B. R. Levich, *Theoretical Foundations of Statistical Radio Engineering [in Russian]*, Sovet-skoe Radio, Moscow (1974).
10. C. Mika, *Dissertation*, Hannover Technical University, Hannover, West Germany (1975).

ANALYTIC APPROXIMATION OF NEUTRON
PHYSICS DATA

S. A. Badikov, V. A. Vinogradov,
E. V. Gai, and N. S. Rabotnov

UDC 539.12.088

A need of an analytic representation of one-dimensional functional relations arises at various stages of physics research and engineering development in which the results of the research are used. The physics calculations for nuclear physics plants require an extremely large amount of calculations and input data. A substantial part of the latter are functions in one variable, describing the energy dependence of the cross sections of various nuclear reactions initiated by neutrons. The acquisition, storage, estimation of these data, and representation of them in a form that is most suitable for use have become an object of independent and important scientific discipline. The goal of this discipline is to obtain estimated data for which, in addition to the value of the cross section for any energy, it is necessary to know the accuracy of that value, i.e., to be able to determine the error of the estimator curve.

The initial experimental information is always a discrete set of values measured with a finite error at a finite number of points. Analytic approximation of these data should determine: The approximant $f^{[L]}(E, p_1, p_2, \dots, p_L)$, where E is an independent variable, p_i are parameters, and L is the total number of the parameters. The value of the approximated cross section for a given E and the $f^{[L]}$ found remains, of course, a random quantity that is not known exactly, so that $f^{[L]}(E)$ is the average value of the statistical distribution of this random quantity;

- $\Delta(E)$ is the error of the random quantity. If its distribution can be assumed to be normal, then usually $\Delta(E)$ is the standard deviation, which is the quadratic form of the errors Δp_i of the parameters;

- The correlation coefficient $\rho(E, E_2)$ for the values of the approximant at two arbitrary points of the energy range under consideration.

All of these characteristics of an approximation by rational functions (Padé approximation) are considered below.

The Padé Approximant, Its Physical Sense, and Different Parametrizations. The Padé approximation was advanced at the end of the last century [1] but only in the last decade has it found increasing application in very diverse problems of mathematical physics [2-7]. Its use in the processing of experimental data has hitherto been limited by the nonlinearity of the corresponding problem of the method of least squares and the peculiar form of the instability due to the appearance of real singular points in the approximant. In [8-10] methods were proposed for overcoming these difficulties, an applicable method of Padé approximation of experimental relations was constructed, and practical experience from the use of this method was accumulated. A Padé approximation of the second kind for a function $f(E)$ is the name given to the rational function

$$f_{N, M}^{[L]}(E) = P_N(E)/Q_M(E) \quad (1)$$

[here, $P_N(E)$ and $Q_M(E)$ are polynomials of degree N and M], which coincides with $f(E)$ at L points, i. e., satisfies the system of equations

$$f_{N, M}^{[L]}(E_\nu) = P_N(E_\nu)/Q_M(E_\nu) = f(E_\nu); \quad \nu = 1, 2, \dots, L. \quad (2)$$

When each equation is multiplied by $Q_M(E_\nu)$ this system is transformed into a linear system in the coefficients of the polynomials. Its solution can be easily found by means of simple two-term recurrence relations, without resorting to matrix inversion (see, e.g., [11]).

A distinctive feature of the Padé approximant is that it has poles which coincide with the roots of the polynomial Q_M . In neutron physics the approximating functions are most often resonance curves of neutron cross sections. The resonances correspond to complex poles of the S matrix and this serves as the physical basis of

Translated from *Atomnaya Énergiya*, Vol. 56, No. 1, pp. 20-25, January, 1984. Original article submitted April 22, 1983.

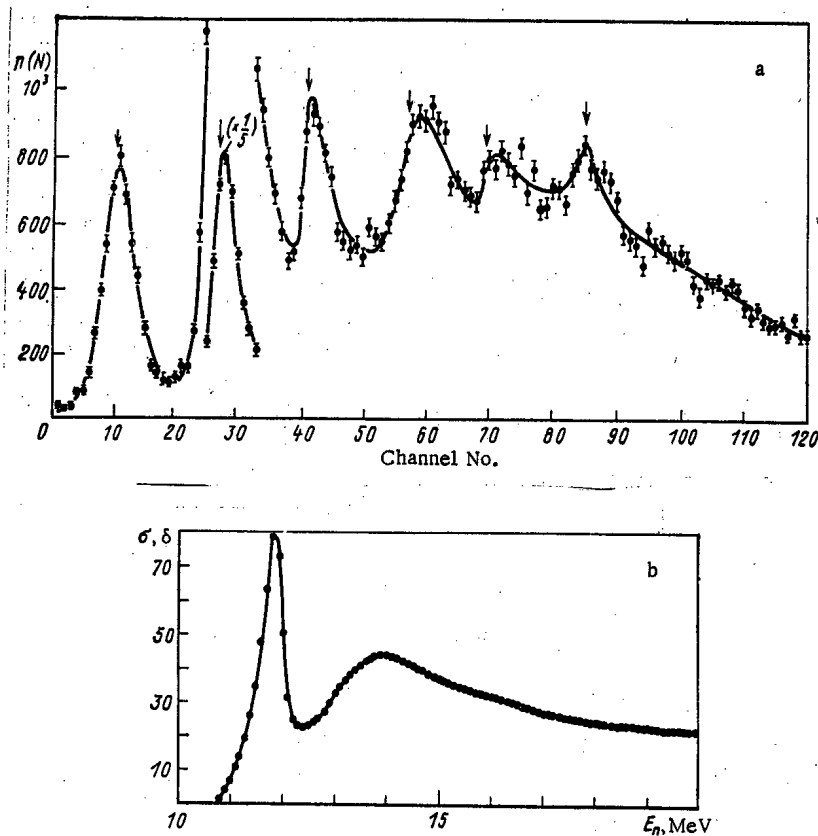


Fig. 1. Results of Padé approximation: a) of time spectrum in measurement of the $^{52}\text{Cr}(p, n)$ cross section [19] for $L = 28$ parameters; b) estimated data on the $^{16}\text{O}(n, p) ^{16}\text{N}$ cross section in point-by-point assignment (BOSPOR library; the complete results of its analytic approximation are collected in [14h]); ●) experiment; —) approximant.

the Padé approximation in this case. Rational functions are convenient to use in calculations. Since the result of any arithmetical operations on them is once again a rational function, which can be expanded into a sum of elementary expressions in only one way [see Eq. (3)], then many functionals (collision integrals, coefficients of resonant self-screening, etc.) which are important in reactor calculations can be quickly calculated analytically.

The parameters determining the Padé approximant can be chosen in many ways, e.g., the coefficients or the roots of the polynomials $P_N(E)$ and $Q_M(E)$ can be taken. One way, which is most suitable for our purposes, is to give the representation in the form of a pole expansion

$$f_{N, M}^{[L]}(E) = C + \sum_{h=1}^{i_1} \frac{ak}{E - p_h} + \sum_{i=1}^{i_2} \frac{\alpha_i (E - \varepsilon_i) + \beta_i}{(E - \varepsilon_i)^2 + \gamma_i^2}. \quad (3)$$

Such an expansion can be obtained by finding the roots of $Q_M(E)$ (the real poles should, naturally, lie beyond the limits of the interval under consideration). Equation (3) is in essence a generalized multilevel formula of resonance analysis and the parameters appearing in it can in many cases be assigned a clear physical meaning. For an investigation of the statistical characteristics of the approximant obtained, however, it turns out to be more suitable to use the parametrization with reference ordinates, as presented in [12, 13]. If we choose L arbitrary values of the argument E_ν and write the system of equations

$$f(E_\nu, p_1, \dots, p_L) = f_\nu; \quad \nu = 1, 2, \dots, L, \quad (4)$$

defining the set (p_ν) as a function of the set (f_ν) , then the values of f_ν can be considered as new independent parameters. We shall call them reference ordinates.

The errors of the reference ordinates directly produce a "corridor of errors" along the curve. Moreover, all of these parameters have the same dimension and the approximant is, in a sufficiently general case, a homogeneous symmetric function of the first order in those parameters (the last is most important). By Euler's theorem on homogeneous first-order functions the following representation is valid for them:

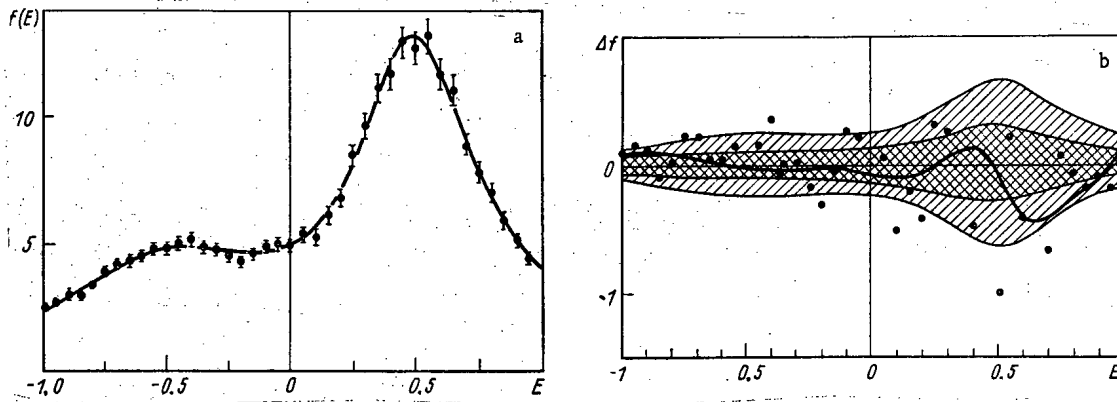


Fig. 2. Results of processing of model problem [the function, determined by Eq. (18), has had its values randomized with a scatter of $(\Delta f/f) = 5\%$]: a) Padé approximant, constructed by discrete optimization; b) estimate of the approximation error by formulas (7) and (9) (cross hatching); single shading represents the experimental error; —) approximant reckoned from the true curve; ●) experiment.

$$f(E, f_1, \dots, f_L) = \sum_{\nu=1}^L f \frac{\partial f}{\partial f_\nu}. \quad (5)$$

Although it is not linear in f_ν (the derivative also depends on f_ν), in some respects, as will be shown below, it can play the role of a linear expansion in orthogonal functions. The choice of the values of the abscissas E_ν is arbitrary, making the parametrization with reference ordinates extremely flexible. The choice can be subordinated to certain optimality requirements and can be made unique. Two versions of such a choice are considered below.

Construction of the Padé Approximant. The system of equations (2) is reduced to a linear system in the coefficients of the polynomials P_N and Q_M , but it can be used to solve only the interpolation problem. A problem of the method of least squares, in which the number N_{ex} of experimental points is greater than the number L of parameters is nonlinear in the Padé approximant. The complexity of the numerical solution of this problem increases as L grows. Accordingly, in [8, 9] we proposed an approximate method of solving this problem by minimizing the statistical sum of a discrete subset of values of the parameters f_ν . In this case L experimental values in different combinations are chosen as reference values. The convergence of the method proved to be entirely acceptable. The details of the corresponding iteration process were described in [8]. Theoretical estimates show that the rms deviation of the approximant obtained by the method of partitioning from the solution of the problem of the method of least squares is smaller by a factor of $\sqrt{N_{\text{ex}}/L} \cdot a$ than the deviation of the latter from the exact curve. If N_{ex}/L is of the order of a few units, the solution can be made more exact by minimizing the statistical sum using gradient methods since an explicit expression [see Eq. (9) below] is easily obtained for the derivatives with respect to the reference ordinates appearing in Eq. (5).

For a number of years we have used the Padé approximation to represent different kinds of experimental and estimated data in neutron and nuclear physics in analytic form [10, 12-17]. Figure 1 shows the approximants for different stages in the processing of neutron data, constructed for the time spectrum at the analyzer output (see Fig. 1a) and for the estimated curve of the cross section for the threshold reaction in point-by-point assignment (see Fig. 1b). Figures 2a and 3a give examples of the processing of a model problem and the construction of an estimated curve on the basis of a set of experimental data from various authors. The examples differ as to the degree of complexity (the number of parameters used is approximately four per "peak"). The method was used to approximate resonance curves with the total number of parameters $L \leq 40$.

Variation of the Choice of Reference Abscissas. Statistically Optimal Padé Approximant. We consider the following problem. Suppose that we know the measured dependence is described by a rational function of order L and suppose that the measurements are carried out for values of the argument E_μ which can be chosen arbitrarily within the limits of the given interval, and that the absolute accuracy of the measurement is fixed and does not depend on E . This means that the measured values are

$$F_\mu = f(E_\mu) + \Delta_\mu, \quad \mu = 1, 2, \dots, L, \quad (6)$$

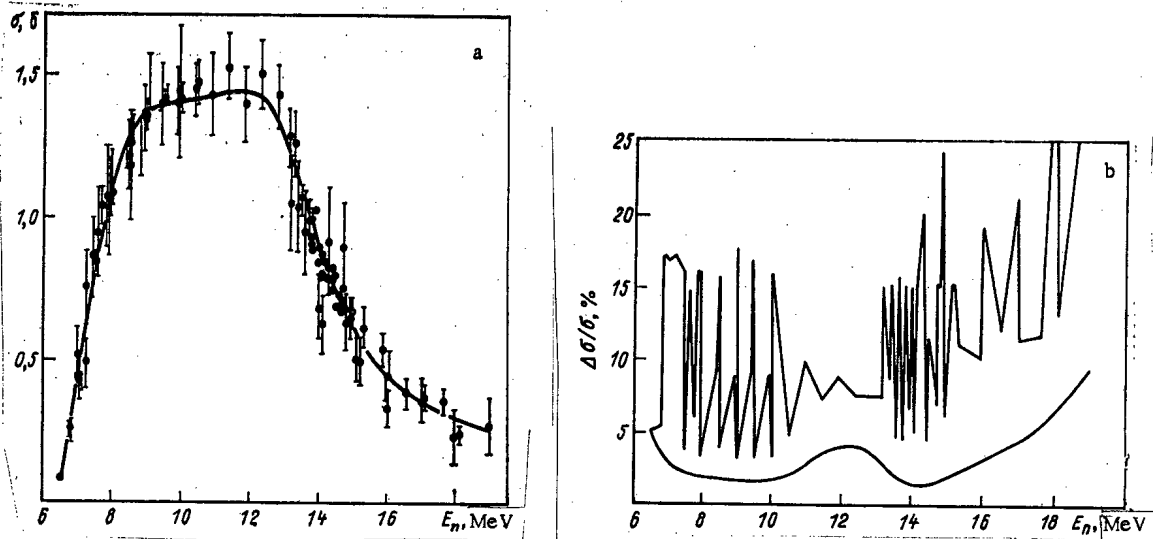


Fig. 3. Results of construction of estimated $\sigma(E)$ curve for the $^{238}\text{U}(n, 2n)$ curve on the basis of the experimental data of [14g]: a) Padé approximant; b) estimate of the approximation error (smooth solid curve); the values of the experimental errors are shown by the broken line.

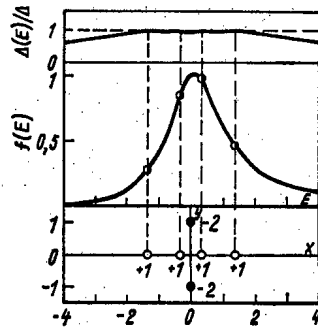


Fig. 4. Maximally informative points and error of statistically optimum interpolation for an isolated resonance. The middle part depicts the function $f(E) = (1 + 0.2E)/(1 + E^2)$; the bottom part shows the position of the maximally informative points (O) and the poles of the approximant in the complex plane (●) to illustrate the electrostatic analogy; the upper part shows the curve of the interpolation error $\Delta(E)$.

where $f(E_\mu)$ are the values of the true rational function and Δ_μ are random quantities with the same normal distribution. The interpolating function $f^{[L]}(E)$ is constructed by substituting F_μ into Eqs. (1) and then solving the system. The values of $f^{[L]}(E)$ at arbitrary points of the interval under consideration are random quantities whose distribution depends on the choice of the interpolation points E_μ .

As the optimality criterion for the choice of E_μ we take the minimization of $\max \Delta^2(E)$, the maximum of the mathematical expectation of the squared deviation of the values of the interpolation function from the true function in the interval under consideration. The rms error of the description, for small Δ_μ , is equal to

$$\Delta^2(E) = \sum_{\mu=1}^L \left(\frac{\partial f^{[L]}(E)}{\partial f_\mu} \right)^2 \bar{\Delta}_\mu^2 = \Delta^2 \sum_{\mu=1}^L \left(\frac{\partial f^{[L]}(E)}{\partial f_\mu} \right)^2 \quad (7)$$

TABLE 1. Reference Abscissas E_μ and Ordinates f_μ , Ensuring a Diagonal Covariant Matrix, and Errors Δf_μ of the Reference Ordinates

μ	Model problem (Fig. 2)			Estimate of $^{238}\text{U}(n, 2n)$ cross section (Fig. 3)		
	E_μ	f_μ	Δf_μ	E_μ, MeV	f_μ, mb^*	$\Delta f_\mu, \text{mb}^*$
1	-0,936	2,650	0,0665	5,55	86,5	4,2
2	-0,669	4,184	0,0870	7,09	508	13,2
3	-0,368	4,838	0,0995	8,24	1209	22,5
4	-0,080	4,652	0,0965	9,75	1405	24,5
5	0,493	7,006	0,1503	11,62	1447	54,1
6	0,432	12,375	0,2935	13,61	1052	19,4
7	0,656	10,254	0,2268	14,60	720	11,8
8	0,927	4,790	0,1101	17,29	335	16,7

* $1 \text{ b} = 10^{-28} \text{ m}^2$.

The right-hand part is obtained for $\bar{\Delta}^2 \equiv \Delta^2$.

The derivatives [in Eq. (8)] of the approximants with respect to the independent parameters (reference ordinates f_ν) possess obvious properties:

$$\left. \frac{\partial f^{[L]}(E)}{\partial f_\nu} \right|_{E=E_\mu} = \delta_{\mu\nu}. \quad (8)$$

From the definition (2) it also follows that all of the functions $\partial f^{[L]}(E)/\partial f_\nu$ should be the ratio of two polynomials, the polynomial in the denominator being equal to $Q_M^2(E)$ while the polynomial in the numerator is of the degree $M+N$ and should satisfy Eqs. (8). This uniquely determines

$$\frac{\partial f^{[L]}(E)}{\partial f_\mu} = \frac{\prod_{\nu \neq \mu} (E - E_\nu) Q_M^2(E_\mu)}{Q_M^2(E) \prod_{\nu \neq \mu} (E_\mu - E_\nu)}. \quad (9)$$

Thus, we require that $\Delta^2(E) \leq \Delta^2(E_\mu) = \Delta^2$ for $E \neq E_\mu$. Then the necessary optimality condition for choice of the reference points will be

$$\left. \frac{\partial}{\partial E} \frac{\partial f^{[L]}(E)}{\partial f_\mu} \right|_{E=E_\mu} = 0; \quad \mu = 1, 2, \dots, L. \quad (10)$$

It was shown in [12, 13] that a simple electrostatic analogy exists for the problem of finding the sets of E_μ which satisfy Eqs. (10). The values of E_μ correspond to the equilibrium coordinates of a system of L charges of the same value and sign which can move freely along the E axis, interacting in accordance with a logarithmic law with each other as well as with M charges of opposite sign and twice the value, attached at points in the plane with the coordinates x_k^0 and y_k^0 if the complex numbers $E_k^0 = x_k^0 + iy_k^0$ are the roots of the denominator of the approximant f . This statement is illustrated in Fig. 4 for the simplest case of an isolated resonance of unit half-width for $Q_M = 1 + E^2$. In the general case calculation of the four statistically optimum abscissas gives $\pm (1 \pm 2/\sqrt{5})^{1/2}$. The optimum points "repel" each other and are "attracted" to the poles of the approximant, i.e., to resonance energies.

In the particular case of polynomial interpolation [$Q_M(E) \equiv 1$] "external" charges are absent and the optimum abscissas coincide with the solution of the problem of the so-called maximum spacing of points on a segment [18]. If by a linear transformation we reduce the interval of values of E under consideration to $[-1, 1]$, then E_μ will be zeros of the derivative of a Legendre polynomial of order $L-1$ with the addition of the ends of the interval $E_{1,L} = \pm 1$ and for $\Delta^2(E)$ we obtain the explicit expression

$$\Delta^2(E) = 1 - (1 - E^2) [P'_{L-1}(E)]^2 / L(L+1), \quad (11a)$$

where $P_{L-1}(E)$ is the Legendre polynomial.

The exact result for the "diagonal" Padé interpolation (for $M=N$) is of interest. In this case $\Delta^2(E) = \Delta^2 = \text{const}$, i.e., the approximation error is constant and is equal to the measuring error (or calculation error if calculated values are interpolated). In another important particular case of the "near-diagonal" Padé approximation ($N=M-1$)

$$\Delta^2(E) = \left[1 - \prod_{\mu=1}^L (E - E_{\mu})^2 / Q_M(E) \right] \Delta^2 \leq \Delta^2. \quad (11b)$$

It must be pointed out that with a nonoptimum (e.g., equidistant) choice of interpolation points the interpolation error increases rapidly with the order; for $L \gg 10$ it assumes the nature of a "swing," in which case the values of the function between angles increase in an unlimited and uncontrolled manner as to modulus. The values of E_{μ} , chosen by this method, will be called statistically optimum abscissas of the first kind or maximally informative points.

Another version of the choice of optimum abscissas is associated with the problem of the method of least squares. It enables a diagonal covariant matrix to be obtained for the reference ordinates for statistically independent experimentally values.

Suppose that F_i ($i=1, 2, \dots, N_{ex}$) are the experimental values of the approximated function, measured for the values E_i of the argument with independent normally distributed errors, whose variances are given and are equal to σ_i^2 . Then

$$S = \sum_{i=1}^{N_{ex}} \frac{[f^{[L]}(E_i) - F_i]^2}{\sigma_i^2} \quad (12)$$

is a statistical sum which can be minimized in the method of least squares. We subject the choice of the reference abscissas E_{μ} ($\mu = 1, 2, \dots, L$) to the requirement that the informative $A_{\mu\nu}$ and its covariant inverse $V_{\mu\nu}$ be diagonal. By definition

$$A_{\mu\nu} = \frac{\partial S}{\partial f_{\mu}} \frac{\partial S}{\partial f_{\nu}} \equiv (V^{-1})_{\mu\nu} = \lambda_{\mu} \delta_{\mu\nu}. \quad (13)$$

Here the averaging is carried out over the distribution of the deviations of the experimental values from the true values. Substituting the sum (12) into Eq. (13), we get

$$A_{\mu\nu} = \sum_{i=1}^{N_{ex}} \frac{1}{\sigma_i^2} \left[\frac{\partial f(E_i)}{\partial f_{\mu}} \right] \left[\frac{\partial f(E_i)}{\partial f_{\nu}} \right] = \lambda_{\mu} \delta_{\mu\nu}. \quad (14)$$

For this matrix to be diagonal it is necessary and sufficient that the derivatives $\partial f(E)/\partial f_{\mu}$ be orthogonal on a discrete set of values of the argument E_i with a weight of $1/\sigma_i^2$. In this case

$$(\Delta f_{\nu})^2 = 1/\lambda_{\nu} \quad (15)$$

are the variances of the reference ordinates as parameters of the approximant.

Using the well-known properties of orthogonal polynomials [18] and taking Eq. (9) into account, we can easily see that in order for Eqs. (14) to be satisfied it is sufficient to take for E_{μ} the roots of the polynomial $p_L(E)$ from the system of polynomials $p_0(E), p_1(E), \dots, p_L(E)$, which are orthogonal on the set E_i with a weight of $1/[\sigma_i^2 Q_M^4(E_i)]$, i.e., satisfy the relations

$$\sum_{i=1}^{N_{ex}} p_h(E_i) p_l(E_i) / \sigma_i^2 Q_M^4(E_i) = N_h \delta_{hl}. \quad (16)$$

Methods of recursive construction of such systems of polynomials are well known [18]. After the choice of the reference abscissas by the method indicated (they can be called statistically optimum abscissas of the second kind) the estimate of the mean-square error of the value of the approximant at any point is determined by Eq. (7) and the correlation coefficient of the values of $f^{[L]}(E_1)$ and $f^{[L]}(E_2)$ at two arbitrary points is equal to

$$\rho(E_1, E_2) = \sum_{\mu=1}^L \frac{\partial f^{[L]}(E_1)}{\partial f_{\mu}} \frac{\partial f^{[L]}(E_2)}{\partial f_{\mu}} (\Delta f_{\mu})^2 / \sqrt{\Delta^2(E_1) \Delta^2(E_2)}. \quad (17)$$

We illustrate the described method of calculating the error of the approximant. We begin with a model example for which we chose the approximation of the function

$$f(E) = \frac{1}{(E+0.5)^2 + 0.5^2} + \frac{1+0.2E}{(E-0.5)^2 + 0.3^2}, \quad (18)$$

"measured" at 41 "equidistant" points in the interval $[-1, 1]$ with an error which was determined by a random-number unit selecting random numbers from a normal distribution with an average value of 0 and a variance

corresponding to a standard deviation of 5%. Figure 2a gives these simulated "experimental" points and the constructed approximant and Fig. 2b gives the deviation of the approximating function from the true function. The shaded regions correspond to the corridors of error, the "experimental" corridor and that determined by formula (7). As was to be expected, the points of the approximant lie in the second corridor, roughly half as wide, with a probability corresponding to the standard deviation. The values of the statistically optimum abscissas of the second kind E_{μ} , the reference ordinates f_{μ} , and the errors Δf_{μ} of the reference ordinates for this example are given in Table 1.

In Fig. 4 such data processing is carried out for the estimate of the cross section for the ^{238}U ($n, 2n$) reaction in the energy range from the threshold energy to 19 MeV (example taken from [14g]). The readings are made from the values of the approximant. Although the number of parameters in the same case is the same as in the first case (eight), abrupt jumps in the dependence of the experimental error on the energy (data from many papers with different accuracy were processed simultaneously) worsen the condition of the numerical construction of the required system of orthogonal polynomials, but this complication does not cause any difficulties. The numerical data, as for the model problem, are given in Table 1. As is seen, the error of the estimate is everywhere noticeably smaller than the envelope of the experimental error.

Conclusion. The method presented above for constructing rational approximants and obtaining their statistical characteristics is fairly convenient and universal. When it is considered that exponential-harmonic analysis also reduces to rational approximation, not of the function itself but of the results of the application of the Fourier and Laplace transforms to the function [15a, b], the range of application of this method encompasses practically all the major systems of approximating functions. The existence of pole singularities in the Padé approximant is an extremely valuable analytic property, substantially expanding the region of convergence and increasing its speed as compared with the polynomial approximation. The Padé approximation is particularly a natural instrument for processing resonance curves since the resonances correspond to complex poles of the approximant. But in the general case as well analytic representation of data in this form is convenient and compact. Thus, representation of data on the cross sections for threshold reactions under the action of neutrons (BOSPOR library [14h]) in the form of rational functions resulted in a 20-fold reduction of the numerical information subject to storage as compared with the point-by-point assignment with the same accuracy of description. All of this enables the Padé approximation to be considered as a promising method of representing neutron and nuclear data.

LITERATURE CITED

1. H. Padé, *Ann. l'Ecole Norm.*, **9**, No. 3, 3 (1892).
2. G. Baker, *Essentials of Padé Approximants*, Academic Press, New York (1975).
3. G. Baker and J. Gammel, *The Padé Approximants in Theoretical Physics*, Academic Press, New York (1970).
4. P. Graves-Morris, *Padé Approximants and Applications*, Academic Press, New York (1973).
5. J. Zinn-Justin, *Phys. Rep.*, **1C**, No. 3, 56 (1971).
6. J. Basdevant, *Fortschr. Physik*, **20**, 283 (1972).
7. A. A. Apresyan, *Izv. Vyssh. Uchebn. Zaved., Radiofiz.*, **22**, No. 6, 653 (1979).
8. V. N. Vinogradov, E. V. Gai, and N. S. Rabotnov, Preprint FÉI-484, Physics and Power Engineering Institute, Obninsk (1974).
9. V. N. Vinogradov, E. V. Gai, and N. S. Rabotnov, *Problems of Atomic Science and Engineering. "Nuclear Constants" Series*, No. 20(1), 13 (1975).
10. V. N. Vinogradov et al., *Yad. Fiz.*, **26**, No. 5, 936 (1977).
11. O. L. Danilov et al., *Continued Fractions. Mathematical Analysis [in Russian]*, Fizmatgiz, Moscow (1961), p. 226.
12. V. N. Vinogradov, E. V. Gai, and N. S. Rabotnov, *Zh. Vychisl. Mat. Mat. Fiz.*, **21**, No. 8, 1557 (1981).
13. V. N. Vinogradov, E. V. Gai, and N. S. Rabotnov, Preprint FÉI-1328, Physics and Power Engineering Institute, Obninsk (1982).
14. V. N. Vinogradov et al., *Problems of Atomic Science and Engineering. "Nuclear Constants" Series*: a) No. 21, 21 (1976); b) No. 25, 76 (1977); c) No. 25, 81 (1977); d) No. 33, 31 (1979); e) No. 34, 70 (1979); f) No. 42, 9 (1981); g) No. 45, 33 (1982); h) No. 47, 66 (1982).
15. V. N. Vinogradov, E. V. Gai, and N. S. Rabotnov, a) Preprint FÉI-513, Physics and Power Engineering Institute, Obninsk (1974); b) Preprint FÉI-554, Physics and Power Engineering Institute, Obninsk (1975); c) Preprint FÉI-951, Physics and Power Engineering Institute, Obninsk (1979); d) Review OB-125, Physics and Power Institute, Obninsk (1981); e) Preprint FÉI-1279, Physics and Power Engineering Institute, Obninsk (1982).

16. V. N. Vinogradov et al., in: Neutron Physics [in Russian], TsNIIAtominform, Moscow (1976), Part 1, p. 165; Part 4, p. 104.
17. V. N. Vinogradov et al., in: Neutron Physics [in Russian], TsNIIAtominform, Moscow (1980), p. 58.
18. G. Seger, Orthogonal Polynomials [Russian translation], Fizmatgiz, Moscow (1962), p. 127.
19. N. S. Biryukov et al., Yad. Fiz., 35, No. 4, 814 (1982).

FRACTURE RATE OF 10Kh2M STEEL WHEN WATER
ENTERS SODIUM IN A COUNTERFLOW STEAM
GENERATOR

V. S. Sroelov, P. P. Bocharin,
A. A. Saigin, and T. I. Vasilevich

UDC 621.039.526

Experimental investigations of processes that occur when water enters sodium in a counterflow steam generator showed that various regimes of sodium flow can arise in a faulty tube [1, 2]: internal-flow regime in which the sodium flows stably through the tube; a displacement regime in which the tube is partially or completely filled with gas and sodium does not flow through the tube; finally, a pulsation regime, characterized by a successive change of internal-flow and displacement regimes. The fracture rate of the structural material at the site of a leak depends essentially on the flow regime. In the displacement regime at leaks greater than 1 g/sec (which is characteristic of the second stage of leak self-development) the tube does not fracture for a fairly long time [1, 3].

In the internal-flow regime the rate of self-development of small leaks is the same as in a once-through steam generator [3]. The same is also true of the fracture rate of the tube opposite the site of a leak [1] since at this point there is a continuous contact of sodium with the leaking water. Consequently, in the calculation of breakdown processes in a counterflow steam generator use can be made of experimental data on the fracture rate of targets, obtained under similar conditions for a once-through steam generator.

The dependence of the fracture rate of 10Kh2M steel on different parameters was investigated thoroughly in [4] but these data cannot be applied directly to the conditions of a counterflow steam generator since they were obtained at a sodium velocity of 0.24 m/sec in the experimental segment (as applied to a steam generator at the Monju Atomic Power Plant) and the sodium flow velocity in the tubes of a counterflow steam generator is substantially higher; e.g., in the counterflow steam generator of the BOR-60 plant [5] this velocity is 3.5 m/sec.

Contradictory results have been obtained on the influence of the sodium flow velocity on the fracture rate of steel. It turns out [6] that at nozzle-target distances of 32-35 mm and water flow rates of 2-30 g/sec the fracture rate of the steel is inversely proportional to the sodium flow velocity. Green [7] reports the opposite tendency: as the sodium flow velocity increases from 0.6 to 3.0 m/sec the fracture rate increases roughly two-fold. Dumm [8] gives a qualitative relation which shows that at relative nozzle-target distances of 15-120 the fracture rate of the steel decreases as the sodium flow velocity increases from 0.3 to 3.0 m/sec. In later papers Kanegae et al. [4] and Cambillard [9] point out that the fracture rate does not depend on the sodium flow velocity. The dependence of the fracture rate of steel on the sodium flow velocity in the tube of a counterflow steam generator, therefore, was investigated experimentally.

The construction of the experimental apparatus is shown in Fig. 1. A sodium channel with a 16-mm diameter is drilled in the casing 1. A water injector is introduced through a fitting 2 into the channel perpendicular to its axis; the injector consists of a bushing 3, piston 4, nickel needle 9, nickel nozzle 10, union nut 5, and a mechanical drive for the needle with a hermetically sealing sylphon bellows (not shown). A target 7, made of 10Kh2M steel, is inserted coaxially with the injector into the channel on the opposite generatrix. An excess argon pressure of 5 MPa was produced in the gap between the target and the flange 8. The experimental apparatus is installed in the circulation sodium loop by welding the casing to the tubes 6.

Before the experiment the sodium loop was heated to the required temperature and the required sodium flow rate through the experimental segment was established. Once the steam line had been purged, the valve

Translated from *Atomnaya Energiya*, Vol. 56, No. 1, pp. 25-28, January, 1984. Original article submitted April 27, 1983.

TABLE 1. Conditions and Results of the Experiments

Conditions of expt.	No. of expt.														
	1	2	3	4	5	6	7	8	9	10	11	12	13	14	15
Sodium temp., °K	716	718	713	721	715	718	708	732	725	730	733	737	733	733	729
Sodium velocity, m/sec	5,36	3,06	0,948	1,81	2,50	3,91	2,92	4,46	5,96	1,35	4,72	2,75	0	1,37	0,967
Steam temp., °K	709	711	706	711	712	710	703	715	708	701	713	718	718	718	720
Diam. of hole, mm	0,48	0,48	0,48	0,48	0,48	0,48	0,60	0,60	0,60	0,60	0,25	0,25	0,25	0,25	0,25
Rel. nozzle-target distance, mm	35,4	35,4	35,4	35,4	35,4	35,4	28,3	28,3	28,3	28,3	68	68	68	68	68
Water flow rate, g/sec	1,87	1,82	1,80	1,99	1,88	1,85	2,97	3,0	2,89	3,0	0,519	0,483	0,525	0,508	0,518
Time of expt., sec	31,3	34,0	37,0	46,6	50,7	55,0	42,4	53,0	80,0	39,0	63,3	106	43,3	40,0	38,3
Depth of fracture, μm	10	130	2190	1910	940	140	1340	500	930	3050	10	10	2600	740	920
Fracture rate, μm/sec	0,1	3,82	59,2	41,0	18,5	2,54	31,6	9,43	11,6	78,2	0,1	0,1	60,5	18,5	24,0

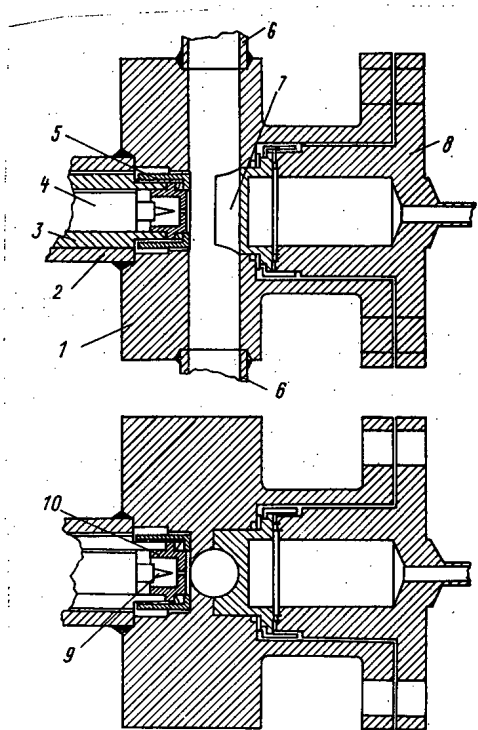


Fig. 1. Construction of experimental apparatus.

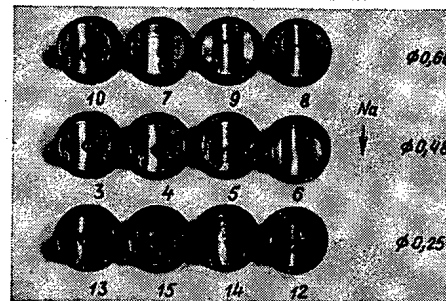


Fig. 2. Targets after tests.

device of the injector was opened and steam entered the sodium. The experiment was ended upon the elapse of a set time or after the target had been burned right through, as indicated by an abrupt drop in pressure in the target gap. In the experiment we determined the flow rate and temperature of the sodium, as well as the feed time, temperature, and flow rate of the steam.

When the target was removed the depth of the fracture was measured with a micrometer. The fracture rate W of the material was defined as the ratio of the depth of the fracture to the steam feed time. The sodium flow velocity was found from the formula

$$v = 4\bar{Q}/\pi d^2,$$

where \bar{Q} is the mean integrated volume of sodium during the experiment and d is the diameter of the channel in the experimental apparatus.

TABLE 2. Values of the Coefficients A, B, C

Coefficient	L/D		
	28,3	35,4	68
A	17,1	12,3	6,9
B	16,5	12,5	7,9
C	0,1	0,05	0

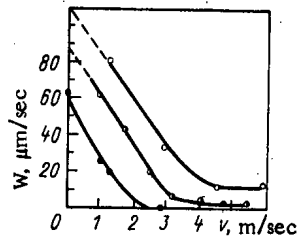


Fig. 3

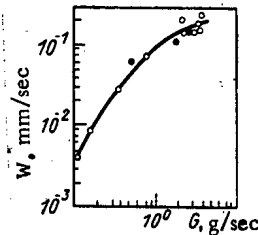


Fig. 4

Fig. 3. Fracture rate as a function of the sodium velocity for different diameters of the steam-delivery hole: ○) 0.6 mm, ◐) 0.48 mm, and ●) 0.25 mm.

Fig. 4. Comparison of data on the fracture rate of 10Kh2M steel, obtained in [4] and in this paper: ○) data of [4], $T=753^{\circ}\text{K}$, $v=0.24$ m/sec, $L=17.5$; ●) data of this paper; the solid curve represents the relation of [4].

The results of the experiment are given in Table 1. The steam pressure in all the tests was the same (9.5 MPa) and the nozzle-target distance was 17 mm. Figure 2 shows targets after the experiments; the numbers are the numbers of the tests.

The position of the experimental points in v - W coordinates (Fig. 3) indicates that under the conditions of a counterflow steam generator the fracture rate of the steel depends essentially on the sodium flow velocity and diminishes as the flow velocity increases, which is consistent with the data of [6] and [8].

Figure 4 compares the data published in [4] on the fracture rate of 10Kh2M with the results obtained, normalized to the same experimental conditions: $v=0.24$ m/sec, $T=753^{\circ}\text{K}$. The values of the fracture rate for $v=0.24$ m/sec are found by extrapolation (see Fig. 3) and the results are recalculated for 735°K by the formula [4]

$$W = \frac{4400}{L} \exp \left\{ - \left[0.255 \left(\ln \frac{G}{5.12} \right)^2 + \frac{5460}{T} \right] \right\}, \quad (1)$$

where L is the nozzle-target distance (mm), G is the water flow rate (g/sec), T is the sodium temperature ($^{\circ}\text{K}$), and W is the fracture rate (mm/sec).

As follows from Fig. 4 formula (1) describes the experimental results with an error of $\sim 20\%$, which confirms that this formula can be used under corresponding conditions for a counterflow steam generator in an internal-flow regime. The dependence of the fracture rate of the steel on the sodium flow rate can be taken into account by correction factors in formula (1).

The experimental dependences of the fracture rate of the steel on the sodium flow velocity (see Fig. 3) in the dimensionless coordinates v^* - W^* can be approximated by broken lines which are described by the following equations:

$$\left. \begin{aligned} W^* &= 1 - \frac{v^*-1}{A} && \text{for } v^* < B \\ W^* &= C && \text{for } v^* \geq B \end{aligned} \right\} \quad (2)$$

As the scale we chose a sodium flow velocity of 0.24 m/sec and a fracture rate $v=0.23$ m/sec. The coefficients A, B, and C for different L/D ratios (D is the diameter of the hold delivering steam) are given in Table 2. The dependence of the coefficient A on L/D can be approximated by the hyperbola

$$A = 480 (L/D)^{-1}. \quad (3)$$

Substituting formula (3) into Eq. (2) and taking the dependence of C on L/D into account, we get

$$W^* = 1 - \frac{v^* - 1}{480} \frac{L}{D}; \quad (4)$$

$$\left. \begin{aligned} W^* \geq 0.1 & \text{ for } 28 \leq L/D \leq 35 \\ W^* \geq 0.05 & \text{ for } 35 < L/D \leq 68 \\ W^* \geq 0 & \text{ for } L/D > 68 \end{aligned} \right\}. \quad (5)$$

From Eq. (4) and the inequality (5) we determined W^* , a correction factor that makes allowance for the dependence of the fracture rate of the steel on the sodium flow velocity.

Thus, the fracture rate of a 10Kh2M steel tube of a counterflow steam generator opposite the segment of a leak in an internal-flow regime can be determined from the formula

$$W = W_0 W^*, \quad (6)$$

where W_0 is the fracture rate calculated from Eq. (1). Equation (6) approximates the experimental results with an error of $\sim 30\%$.

On the basis of the data obtained we can make certain conclusions about the mechanism of the influence of the sodium flow velocity on the fracture rate of the steel. From the shape of the target after the experiments (see Fig. 2) it is not difficult to determine the distance by which the axis of the jet is displaced at the point of intersection with the target, under the action of the sodium flow. At a sodium velocity of 2.75 m/sec and a relative distance $L/D=68$ this displacement of the jet axis was 4.5 mm (test No. 12), which corresponds to a deviation of the axis by an angle of 13° and an elongation of the path from the site of the leak to the target from 17 to 17.6 mm. It is not very likely that in this case the mechanical energy acquired by the target would decrease substantially, although the fracture rate in this test dropped almost to zero. Apparently, when the sodium flow velocity increases under the conditions of a confined space the mixing of the pure sodium with the products of the reaction in the jet intensifies and as a consequence of this the temperature of the jet and the concentration of reaction products in it decrease, leading to a drop in the fracture rate.

LITERATURE CITED

1. V. S. Sroelov, A. A. Saigin, and P. P. Bocharin, Preprint P-33(327), Scientific-Research Institute for Atomic Reactors, Dimitrovgrad (1977).
2. V. S. Sroelov et al., Preprint P-35(443), Scientific-Research Institute for Atomic Reactors, Dimitrovgrad (1980).
3. F. A. Kozlov et al., *At. Energ.*, **53**, No. 4, 231 (1982).
4. N. Kanegae et al., *Water Reactions, Nucl. Technol.*, **40**, 261 (1978).
5. V. A. Tsykanov et al., in: *Papers of Seminar of COMECON Member Countries. Experience on the Development and Operation of Steam Generators for Fast Reactors* [in Russian], Dimitrovgrad, May 18-21 (1982), p. 64.
6. I. Biscarel, A. Lafon, and N. Lions, *Effect de petites fuites d'eau dans le sodium sur les tubes du faisceau des générateurs de vapeur de Phénix*. IAEA Study Group Meeting on LMFBR Steam Generators, Bensberg Federal Republic of Germany, October 14-17 (1974).
7. D. A. Greene, "Sodium-water wastage and reactions program performed by General Electric in support of the U. S. AEC LMFBR Steam Generator Development, IAEA Study Group Meeting on LMFBR Steam Generators," Bensberg, Federal Republic of Germany, October 14-17 (1974).
8. K. Dumm, "Small water/steam leaks on sodium-heated steam generators - evaluation of the reaction-zone effects on $2\frac{1}{4}$ Cr 1 Mo structural material," IAEA Study Group Meeting of LMFBR Steam Generators, Bensberg, Federal Republic of Germany, October 14-17 (1974).
9. E. Cambillard, "Compte rendu des essais d'érosion-corrosion sur l'acier soviétique 1X2M," Reunion Franco-Soviétique, Saclay, November 23-25 (1977).

HYDROGEN BALANCE IN THE INTOR REACTOR

V. M. Sharapov, A. E. Gorodetskii,
A. P. Zakharov, and A. I. Pavlov

UDC 621.039.633

Direct experiments on the determination of hydrogen leaks through the first wall of a tokamak reactor due to diffusion have still not been conducted up to now, and either computational data or the data of simulation experiments on hydrogen permeability under conditions of ion bombardment are used to estimate these leaks. We have conducted such experiments using a glow discharge. A glow discharge seems to us to be a convenient means of simulating the interaction of a low-temperature hydrogen plasma with a metal primarily because of the possibility of producing a plasma with a wide range of ion energies and ionic fluxes (right up to the largest expected in thermonuclear assemblies).

The equipment layout and experimental procedure are described in [1]. The flux and ion energy were similar to the values expected in the INTOR and were $3 \times 10^{16} \text{ cm}^{-2} \cdot \text{sec}^{-1}$ and 350 eV, respectively. The investigations were conducted in the 300–800°C temperature range. The membrane being investigated served as the cathode, and different brands of stainless steel were investigated [2]. Only the results for Kh18N10T stainless steel (Type SS 304) are given in this article.

The temperature dependence of the flux P passing through a sample whose wall thickness is $d=0.5 \text{ mm}$ is given in Fig. 1 (curve 1). In the high-temperature region the activation energy of the penetration process is 14,500 cal/mole. The deviation from an exponential nature of the temperature dependence of P at low temperatures is possibly associated with the effect of migratory radiation defects or the atomic component of the plasma on the hydrogen diffusion. Similar dependences were also obtained for samples with wall thicknesses of 1 and 1.5 mm. An inverse proportionality of transmitted flux P to thickness is observed in the region in which the exponential temperature dependence is noted.

The results of these experiments have been used to estimate the hydrogen balance in the discharge chamber of the INTOR (surface area of the discharge chamber is $S=400 \text{ m}^2$, volume $V=300 \text{ m}^3$, and stainless steel wall thickness is 10 mm). The experimental data on permeability were scaled to a thickness of 10 mm according to the law $P \sim 1/d$. The duration of a discharge pulse is taken to be equal to 100 sec, and the interval between pulses is taken as 20 sec.

Data on the amount of hydrogen which has passed through, the hydrogen content in the metal volume, the time to establish a steady flux, and the ratio of the hydrogen which has passed through the metal to the incident flux are given in Table 1 for different temperatures.* When the wall is in contact with the plasma (see Table 1) it was established that:

1. The fluxes of hydrogen passing through the wall P_{pass} for a given thickness are approximately 10^{-5} – 10^{-3} of the incident flux.

2. The amount of hydrogen which accumulates in the wall in the permeability regime Q_{f} at a temperature above 400°C depends weakly on the temperature. In this case the hydrogen concentration C in the wall depends only on the flux of ions incident on the wall, and the amount of transmitted flux (the hydrogen permeability) is determined by the diffusion coefficient. Therefore the lower the temperature, the smaller the hydrogen losses are. At a temperature below 400°C the hydrogen content in the wall increases. Thus the hydrogen losses are a minimum at 400°C.

*The values of the diffusion coefficients of hydrogen in stainless steel $D=0.12 \exp(-14,100/T)$ taken from [3] are used in the calculation.

†The amount of hydrogen in the wall in the steady permeability regime is determined from the expression $Q = C_{\text{in}}/2(S \cdot d) = (P_{\text{pass}} \cdot d)/2D(S \cdot d)$, where C_{in} is the hydrogen concentration on the side of the wall in contact with the plasma.

Translated from *Atomnaya Énergiya*, Vol. 56, No. 1, pp. 29–31, January 1984. Original article submitted April 29, 1983.

TABLE 1. Data on the Hydrogen Permeability of a Wall in Contact with a Hydrogen Plasma at Different Temperatures (Kh18N10T stainless steel, $d=10$ mm, $P_{inc}=3 \times 10^{26}$ ions \cdot cm $^{-2}$ \cdot sec $^{-1}$)

T, °C	P_{pass} , atoms/(cm 2 \cdot sec)	P_{pass}/P_{inc}	Amt. of hydrogen passing in 100 sec through an area 4 \cdot 10 6 cm 2 , liters*	Amt. of hydrogen in a wall with area 4 \cdot 10 6 cm 2 in the steady permeability regime, liters*	Time to establish a steady flux, h	Amt. of hydrogen escaping from the wall in the interval between pulses, liters*	Concn. of the hydrogen liberated into the discharge chamber towards the end of the interval bet. pulses N, atoms/cm 3
300	$1 \cdot 10^{13}$	$3,3 \cdot 10^{-5}$	0,008	68	85,5	0,45	$3 \cdot 10^{13}$
400	$2,65 \cdot 10^{12}$	$8,8 \cdot 10^{-6}$	0,02	29,2	13,3	0,48	$3 \cdot 10^{13}$
600	$3,25 \cdot 10^{13}$	$1,1 \cdot 10^{-5}$	0,22	32	1,2	1,7	$1,2 \cdot 10^{13}$

*Normal conditions.

Remark. When the thickness d is changed, these values will change as follows: the penetrating flux $\sim 1/d$; the amount of hydrogen which accumulates in the wall $\sim d$; the amount of hydrogen liberated from the wall in the interval between pulses does not depend on d ; the time to establish a steady regime is $\sim d^2$; and the hydrogen concentration in the discharge chamber towards the end of the interval between pulses does not depend on d .

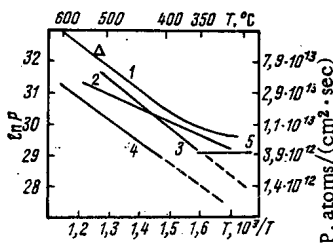


Fig. 1. Temperature dependence of the hydrogen permeability of the stainless steel upon ionic irradiation: 1) data of this paper; 2-5) data of [5, 6, 4, and 9], respectively.

3. The indicated amount of hydrogen in the wall (in the permeability regime) is accumulated in a specified time. Thus at 300°C this will occur after approximately 3000 pulses.

4. The amount of hydrogen P_{lib} liberated from the wall in the interval between pulses (our estimate as applied to the INTOR) will amount to

$$P_{lib} = P_{pass} \cdot \frac{d}{\sqrt{Dt_{int}}} St_{int}, \quad (1)$$

where t_{int} ($t_{int} > 1$ sec) are the time intervals between pulses and P_{pass} is the flux of penetrating hydrogen (hydrogen permeability).

This expression is the solution of the diffusion equation which describes the liberation of hydrogen with the following boundary and initial conditions:

$$\frac{\partial C}{\partial t} = D \frac{\partial^2 C}{\partial x^2}; \quad (2)$$

$$-D \frac{\partial C}{\partial x} = \delta C |_{x=0} \dagger; \quad (3)$$

$$C(x, 0) = C_0 = \frac{P_{pass}}{D} d. \quad (4)$$

† δ is the rate constant of hydrogen liberation.

TABLE 2. Data of the Hydrogen Permeability of a Wall in Contact with Molecular Hydrogen *

T, °C	Diffusion coeff., cm ² /sec	P pass, atoms/(cm ² ·sec)	Amt. of hydrogen passing in 100 sec through an area of 4·10 ⁶ cm ² , liters †	Amt. of hydrogen in wall with area 4·10 ⁶ cm ² in the steady permeability regime, liters †
300	5,4·10 ⁻⁷	4,8·10 ¹⁰	3,8·10 ⁻⁴	3,4
400	3,4·10 ⁻⁶	4·10 ¹¹	3,2·10 ⁻³	4,4
600	3,7·10 ⁻⁵	6,5·10 ¹²	5,2·10 ⁻²	6,4

*The values in Table 2 are obtained by extrapolation of the experimental data for 1330 Pa to a pressure of 133 Pa. One should have performed this extrapolation to p=0.133-0.0133 Pa (the working pressure in the chamber). However, indeterminacy of the dependence of the indicated values of pressure at p=0.133 Pa would make such an extrapolation incorrect.

†Normal conditions.

In 20 sec the amount of hydrogen liberated at a temperature of 300°C amounts to approximately 0.7% of the amount of hydrogen which has accumulated in the wall in the permeability regime. A value of ~5% has been obtained by a similar estimate [4]. At higher temperatures this value becomes greater, and at 600°C more than 5% of the hydrogen which has penetrated during a pulse is liberated in 20 sec.

5. We have also estimated the concentration of hydrogen in the discharge chamber towards the end of the interval between pulses. The fact that at any time the evacuation rate is equal to the liberation rate of hydrogen from the wall, i.e.,

$$(dN/dt)_{\text{evac}} = (dN/dt)_{\text{lib}} \quad (5)$$

where N is the number of molecules in the chamber volume, was an initial prerequisite, just as in [5].

The evacuation rate is

$$(dN/dt)_{\text{evac}} = N/\alpha, \quad (6)$$

where α is the evacuation constant (for the operating conditions of INTOR $\alpha = 1$ sec).

The liberation rate is

$$(dN/dt)_{\text{lib}} = P_{\text{lib}} (S/V), \quad (7)$$

and P_{lib} is determined from expression (1).

Then the hydrogen concentration in the discharge chamber towards the end of the interval between pulses will be

$$N = \alpha (dN/dt)_{\text{evac}} = \alpha (dN/dt)_{\text{lib}} = \alpha P_{\text{lib}} (S/V) = 10^{-2} P_{\text{lib}} \quad (8)$$

The values of N for different temperatures are given in Table 1. At all values of the temperature N does not exceed the hydrogen concentration in the discharge chamber up to the starting time of the pulse.

Thus, it is clear that when the wall is in contact with a hydrogen plasma the total flow rate of hydrogen (that leaving the discharge chamber due to permeability and that accumulating in the wall) will appreciably exceed the amount of hydrogen in the discharge chamber necessary for the occurrence of a thermonuclear reaction (2 liters).

Data on the hydrogen permeability of a sample of Kh18N10T stainless steel 10 mm thick in contact with molecular hydrogen at a pressure of 133 Pa, recalculated, just as for Table 1, from experimental results for a thickness of 0.5 mm, are given in Table 2. It is evident that in this case the hydrogen flow rate is appreciably less than when the wall is in contact with the plasma. Since the hydrogen pressure in the discharge chamber of the reactor is 0.13-0.013 Pa, the molecular hydrogen leaks at such a pressure are 10³-10⁴ times smaller than from the plasma and will be insignificant in the overall hydrogen balance.

Therefore, it is clear that the most obvious way of protecting the wall from saturation of hydrogen is preliminary molecule formation from ions of atomic or ionized hydrogen until it comes in contact with the first wall. One can achieve this most simply by putting a protective shield (not necessarily hermetic) in front of the wall which bears the brunt of the ionic or atomic hydrogen flows.

Either special treatment of the surface or the creation of special protective coatings can be considered as alternative methods. In order to decrease the hydrogen permeability, it is necessary to raise the rate of reverse liberation of hydrogen by increasing either the effective surface or the rate constant of hydrogen liberation.

In conclusion, we shall compare the data given for hydrogen permeability with similar published results.

Curves 2 and 3 constructed on the basis of calculations of the hydrogen permeability of the first wall made with application of INTOR by American [6] and German [7] scientists are also given in Fig. 1. All the data are given for a thickness of 0.5 mm and an ionic flux $j = 10^{16} \text{ cm}^2 \cdot \text{sec}^{-1}$. It was assumed that $P \sim 1/d$ and $P \sim j$, which has been confirmed by our tests with a glow discharge. Data on hydrogen permeability at $T = 300$ and 500°C for curve 2 were taken from Tables 1 and 2 of [6] with an identical temperature on the inner and outer sides of the wall. The values of P for curve 3 were calculated for temperatures of 350 and 500°C from the formula $P = D \frac{C}{d}$, into which the values of C from Table 3 of [7] and D from [8] are substituted. The permeability itself was directly calculated by the authors of [7] just for 500°C (it is shown as a triangle in Fig. 1). It should be said that previously performed calculations of hydrogen permeability by these same authors [4] give somewhat smaller values of P (curve 4), evidently due to the fact that smaller diffusion coefficients were used in the calculation than in [6] and [7].

Comparing the dependences given, one can draw the following conclusions.

1. The data on hydrogen permeability (and the permeability of tritium) taken from various sources correlate quite well, and the hydrogen permeability of the first wall can be predicted with an error of a factor of two-three. One should stipulate that this is valid for comparatively thin walls when the temperature difference between both sides is either insignificant or absent.

2. The calculation in [6] was performed for a "pure" metal surface ($\alpha = 0.5$). Constants of the surface processes (σ_{K}) also obtained after careful outgassing of the surface were used in the calculation of hydrogen permeability in [7]. In our experiments with a glow discharge the samples were outgassed in advance in a vacuum at $500\text{--}600^\circ\text{C}$, and then they were cleaned in the course of discharge burning during the experiment. Part of the sputtered material was again deposited onto the sample surface (i.e., the conditions were similar to those which exist in actual tokamaks).

The comparatively small difference in the hydrogen permeability in all three cases shows that evidently ordinary vacuum thermal conditioning of the wall surface, and all the more the use for this purpose of a gas discharge, leads to sufficiently good cleaning of the surface, as clean as a steel surface as an engineering material can be in general due to carbon, which is capable of emerging from the interior to the surface during operation of the equipment.

3. In estimating the hydrogen permeability at a low temperature (below 350°C), it is necessary to be oriented to the experimental results, since the weakening of the temperature dependence of hydrogen permeability (curve 1) at low temperatures, and then possibly an independence of the temperature, has not been taken into account in the models used in [6] and [7]. The experimental data presented in [9] (see the figure and curve 5) indicate such a possibility.

LITERATURE CITED

1. V. M. Sharapov, A. P. Zakharov, and V. V. Matveev, *Zh. Tekh. Fiz.*, 45, 2002 (1975).
2. V. M. Sharapov, A. I. Pavlov, and A. P. Zakharov, *Zh. Fiz. Khim.*, 56, No. 5, 1202 (1982).
3. K. Wilson and M. Baskes, *J. Nucl. Mater.*, 76-77, 291 (1978).
4. P. Wienhold et al. *J. Nucl. Mater.*, 93-94, 866 (1980).
5. V. Kh. Alimov, A. E. Gorodetskii, and A. P. Zakharov, *Zh. Fiz. Khim.*, 54, 2882 (1980).
6. M. Baskes, K. Wilson, and W. Bauer, USA Input to INTOR Workshop Session III, Phase 2A, December 1981.
7. P. Wienhold et al., "Berichte der Kernforschungsanlage Jülich," No. 1964, Institut für Plasmaphysik Jül 1694, December 1980.
8. M. Braun et al., *J. Nucl. Mater.*, 93-94, 861 (1980).
9. A. I. Livshits et al., *Voprosy Atomnoi Nauki i Tekhniki, Ser. Termoyadernyi Sintez*, No. 2(10), 73 (1982).

EFFECT OF UNCERTAINTIES IN NEUTRON CROSS
SECTIONS ON THE CHARACTERISTICS OF A
THERMONUCLEAR REACTOR BLANKET AND SHIELD

A. I. Ilyushkin, I. I. Linge,
V. P. Mashkovich, V. K. Sakharov,
G. E. Shatalov, and A. V. Shikin

UDC 621.039.51.15

The transition from a theoretical consideration to the development of conceptual designs of high-power thermonuclear reactors requires the solution of many engineering problems, including the important problem of the design of the blanket and radiation shield of the magnetic system coils (MSC).

The main problems in designing the blanket and shield are determined by their functional purpose. For the blanket it is the lifetime of tritium and plutonium, and radiation heat release. The admissible errors of the calculation of the fundamental blanket parameters are rather small (1-3%), and cannot always be maintained in calculations.

For the MSC shield it is necessary:

to decrease radiation damage in ordinary conductors (e.g., the superconducting busbar stabilizer) to a level at which their resistance is increased by no more than 1.5-2 times;

to prevent a decrease of the critical current in the superconductor (NbTi or Nb₃Sn) under neutron bombardment. For Nb₃Sn, for example, the admissible fluence of fast neutrons ($E > 0.1$ MeV) should not exceed 10^{18} neutrons/cm²;

to decrease the radiation damage in the electrical insulators to prevent a decrease in their resistance. The absorbed dose in this case should not exceed 10^7 Gy;

to decrease the total energy release to a few kilowatts, and to decrease the activation of structural elements of the superconducting windings.

A good basis for the design of a thermonuclear reactor shield is provided by the experience in calculating and designing nuclear reactor shields. However, the structural features of a thermonuclear reactor and the specific properties of the radiation source required additional research and development, including an estimate of the dependence of the errors of the characteristics being calculated on the inaccuracy of the input parameters of the problem.

The errors of the design characteristics of models of the blanket and shield are determined mainly by the uncertainties in the interaction cross sections used. The uncertainties in the multigroup neutron interaction cross sections are due to the errors in the initial nuclear data and in the approximations made in preparing the group interaction cross sections. These errors affect the calculation of nuclear reactor shields also, but they may be still larger in a thermonuclear reactor because of the high energy of the source neutrons. Fast neutrons can undergo inelastic scattering on nuclei of most elements, (n, 2n) reactions, (n, 3n) reactions, and other threshold reactions which play a minor role in the formation of the neutron distribution in nuclear reactors. In a thermonuclear reactor these processes determine the energy distribution of fast neutrons in the blanket and shield, the heat release, and the extent of the radiation damage in structural materials. The errors which arise in the preparation of group constants are due to the strong deformation of the fast neutron spectra in the blanket and shield.

Uncertainties of the first type can be reduced only by further cross section measurements. The determination of the energy range and the required degree of accuracy of the cross section measurements requires data on the sensitivity of the blanket and shield characteristics to variations of the interaction cross sections. This motivates the attention to the problem in hand [1, 2].

Translated from *Atomnaya Énergiya*, Vol. 56, No. 1, pp. 32-36, January, 1984. Original article submitted December 8, 1982.

In the choice of the method of calculating the relative sensitivity functions of the design functional R of the radiation field to variations of an input parameter x_i , defined as

$$p_R(x_i) = \frac{\delta R/R}{\delta x_i/x_i}, \quad (1)$$

preference was given to a method based on linear perturbation theory and realized in the ZAKAT program [3]. The input data for this program are the solutions of the forward and adjoint transport equations obtained with the ROZ-11 program [4], and files of multigroup constants. The program is based on the calculation of the functions of relative sensitivity to variations of the absorption cross sections, cross sections for elastic or inelastic transfer from group to group, and variations of the individual harmonics of these cross sections. The relative sensitivity of R to a variation of the l -th harmonic of the elastic scattering cross section of the k -th isotope in the geometric region V_m , in particular, is calculated with the formula

$$p_R(\Sigma_{el,l}^{i,j,h}, V_m) = -\frac{2\pi}{R} \int_{-1}^1 \int_{V_m} \varphi^i(r, \mu) \Sigma_{el,l}^{i,j,h}(r) \varphi^{*j}(r, \mu) d\mu dV +$$

$$+ \frac{1}{4\pi R} \int_{V_m} \varphi_0^i(r) \Sigma_{el,0}^{i,j,h}(r) \varphi_0^{*j}(r) dV \quad \text{for } l=0;$$

$$p_R(\Sigma_{el,l}^{i,j,h}, V_m) = \frac{2l+1}{4\pi R} \int_{V_m} \varphi_l^i(r) \Sigma_{el,l}^{i,j,h}(r) \varphi_l^{*j}(r) dV \quad \text{for } l \geq 1.$$

In addition, the ZAKAT program provides for the calculation of the sensitivity to variations of the characteristics of the fission cross section $\Sigma_f^{i,k}$, $\nu^{i,k}$, and $\chi^{j,k}$

$$p_R(\Sigma_f^{i,k}, V_m) = -\frac{2\pi}{R} \int_{-1}^1 \int_{V_m} \varphi^i(r, \mu) \Sigma_f^{i,k}(r) \varphi^{*i}(r, \mu) d\mu dV;$$

$$p_R[(\nu \Sigma_f)^{i,k}, V_m] = \frac{1}{4\pi R} \int_{V_m} \chi^j \varphi_0^{*j}(r) (\nu \Sigma_f)^{i,k} \varphi_0^i(r) dV;$$

$$p_R[(\nu \Sigma_f)^{i,k}, V_m] = p_R(\Sigma_f^{i,k}, V_m) + \sum_j p_R[(\nu \Sigma_f)^{i,k}, \chi^{j,k}, V_m]$$

and to variations of Σ_R^i the response function of the functional R being calculated:

$$p_R(\Sigma_R^i, V_m) = \frac{2\pi}{R} \int_{-1}^1 \int_{V_m} \varphi^i(r, \mu) \Sigma_R^i(r, \mu) d\mu dV. \quad (4)$$

The following notation was used in Eqs. (2)-(4): $\varphi^i(r, \mu)$ and $\varphi^{*i}(r, \mu)$ are, respectively, the spatial-angular neutron flux density and importance of the i -th energy group; $\varphi_l^i(r)$ and $\varphi_l^{*i}(r)$ are the l -th harmonics of the expansions of $\varphi^i(r, \mu)$ and $\varphi^{*i}(r, \mu)$ in Legendre polynomials; $\Sigma_{el,l}^{i,j,k}$ is the l -th harmonic of the cross section for elastic transfer from group i to group j during scattering on the k -th isotope; $\Sigma_f^{i,k}$ and $\nu^{i,k}$ are, respectively, the fission cross section and the average number of neutrons per fission of the k -th isotope in the i -th energy group; $\chi^{j,k}$ is the fraction of fission neutrons which belong to group j . Integration of expressions of the type (2)-(4) over various variables gives data on the sensitivity of R to variations of the partial and total cross sections of specific elements, and the macroscopic cross sections of the medium.

The design model of the blanket and shield under study (Fig. 1) includes a first wall of stainless steel (0.7 cm), uranium (24.7 cm) and lithium (35.0 cm) blankets, an iron-water shield (110 cm), and the region of the magnetic system coils. The uranium zone contains 27.5% natural uranium and ensures the lifetime of plutonium ($K_{Pu} \approx 1.1$ per source neutron). The lithium zone, filled with the eutectic $Li_{17}Pb_{83}$, ensures the lifetime of tritium ($K_T \approx 1.17$ tritium nuclei per source neutron). Layers of moderator are distributed through the lithium zone to increase the lifetime of tritium. Because of its low density the coolant is not taken into account in the calculations. The windings are shielded by alternating layers of stainless steel, boron steel containing 0.6 wt.% boron, and water. The MSC zone is introduced to give a correct account of the boundary conditions in the form of a homogeneous region of copper and stainless steel.

The characteristics of the neutron distribution at various distances from the first wall were calculated with the ROZ-11 program in plane geometry, and with the BLANK program [5] in cylindrical geometry. The 49 group BND-49 constants [6] were used in calculations with the ROZ program, and the 52 group library of

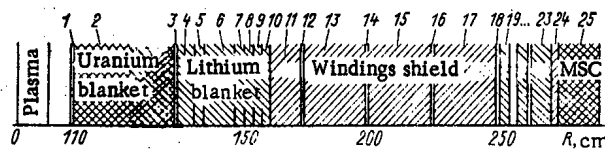


Fig. 1

Fig. 1. One-dimensional design model of thermonuclear reactor blanket and shield. Volume composition of zones: zones 1, 3, 11, 13, 15, 17, 24) stainless steel (100%); zone 2) uranium (27.5%), iron (23.0%); zones 4 and 6) iron (4.3%), $\text{Li}_{17}\text{Pb}_{83}$ eutectic (79.0%); zones 5, 7, 9) iron (5.3%), eutectic (46.8%), calcium hydride (48.6%); zones 8 and 10) iron (2.0%), eutectic (98.0%); zones 12, 14, 16, 18, 20, 22) water (100%); zones 19, 21, 23) boron steel (100%); zone 25) steel (50%), copper (50%).

Fig. 2. a) Spatial distribution of neutron flux density at various energies; b) neutron spectra at $r=136$ cm calculated with ROZ-11 program (—) and with the BLANK program (---).

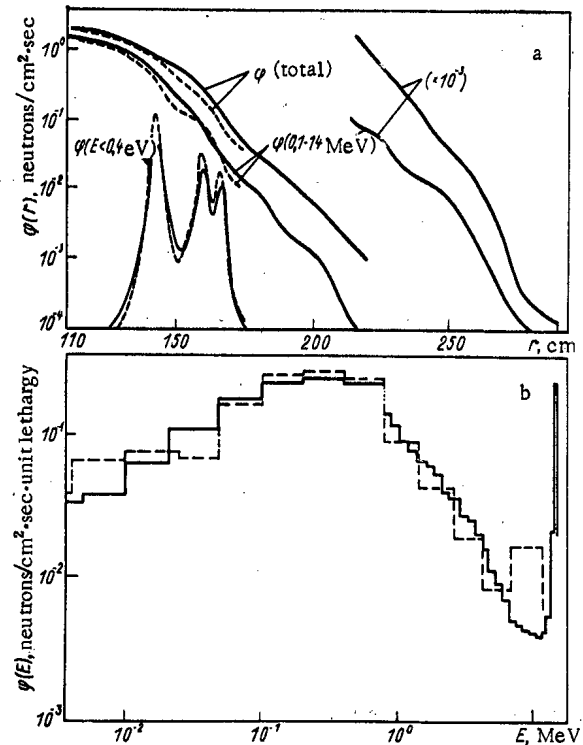


Fig. 2

neutron constants in the energy range 0.1–14.1 MeV [7] combined with the 21 group system of constants [8] in the energy range $E > 0.1$ MeV in calculations with the BLANK program. Figure 2 shows the spatial and energy distributions of the neutron flux density calculated with these programs. Differences in geometry were taken into account by appropriate normalization of the results. The agreement of the calculated results is good in the uranium zone and satisfactory in the lithium zone.

We chose as design characteristics the lifetime coefficients of plutonium (K_{Pu}) and tritium (K_{T}), which are global characteristics of the blanket, and the fast ($E > 0.1$ MeV) neutron flux density at the outer boundary of the shield (ϕ_{b}). We analyzed the energy dependence of the relative sensitivity of K_{Pu} , K_{T} , and ϕ_{b} to variations of the following cross sections: absorption (Σ_{a}), elastic (Σ_{el}) and inelastic (Σ_{in}) scattering, fission (Σ_{f}), and the total interaction cross sections of ^{238}U , Pb , ^6Li , ^7Li , Fe , Cr , and other components of the blanket and shield, and also the sensitivity of variations of the $\Sigma_{\text{n},\gamma}^{238}\text{U}$ and $\Sigma_{\text{n},\alpha}^6\text{Li}$ cross sections, which determine the response functions of the K_{Pu} and K_{T} functionals.

Absorption Cross Section. The values of K_{Pu} , K_{T} , and ϕ_{b} are insensitive to the absorption cross sections of all elements and nuclides except ^{238}U and ^6Li ; $p_{K_{\text{T}}}(\Sigma_{\text{a}}^{\text{Fe}})$ and $p_{K_{\text{Pu}}}(\Sigma_{\text{a}}^{\text{Fe}})$, for example, do not exceed 0.54 and 0.46, respectively. An appreciable contribution to $p(\Sigma_{\text{a}}^{\text{Fe}})$ comes from the energy range in which the uncertainties in $\Sigma_{\text{a}}^{\text{Fe}}$ are small (Fig. 3). Because of the increase of the capture cross section and the decrease of the neutron flux density with decreasing energy down to 4.65 eV, the values of $p_{K_{\text{T}}}(\Sigma_{\text{a}}^{\text{U}})$ and $p_{K_{\text{Pu}}}(\Sigma_{\text{a}}^{\text{U}})$ are approximately independent of energy in the range 4.65 eV–1 MeV. The uncertainties in $\Sigma_{\text{a}}^{\text{U}}$ in this range do not exceed 4–5% [9]. The small uncertainties in $\Sigma_{\text{a}}^{\text{U}}$ assume a correct account of resonance self-shielding of the cross sections. Since the sensitivity of K_{Pu} to a variation of the response function is positive, and in the energy range 4.65 eV–200 keV is larger than $p_{K_{\text{Pu}}}(\Sigma_{\text{a}}^{\text{U}})$, we can conclude that the uncertainties in the response function play a significant role in the calculation of K_{Pu} .

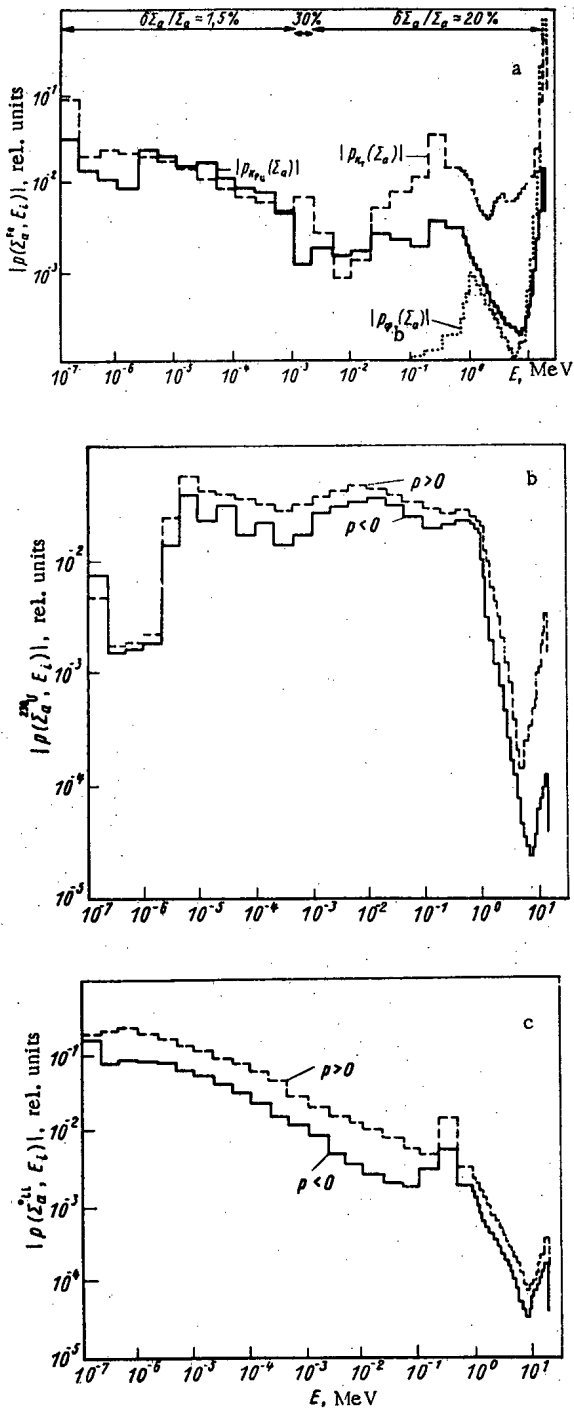


Fig. 3

Fig. 3. Energy dependence of relative sensitivity of K_{Pu} (—), K_T (---), and ϕ_b (. . .) to variations of the absorption cross sections of a) Fe; b) ^{238}U ; c) 6Li .

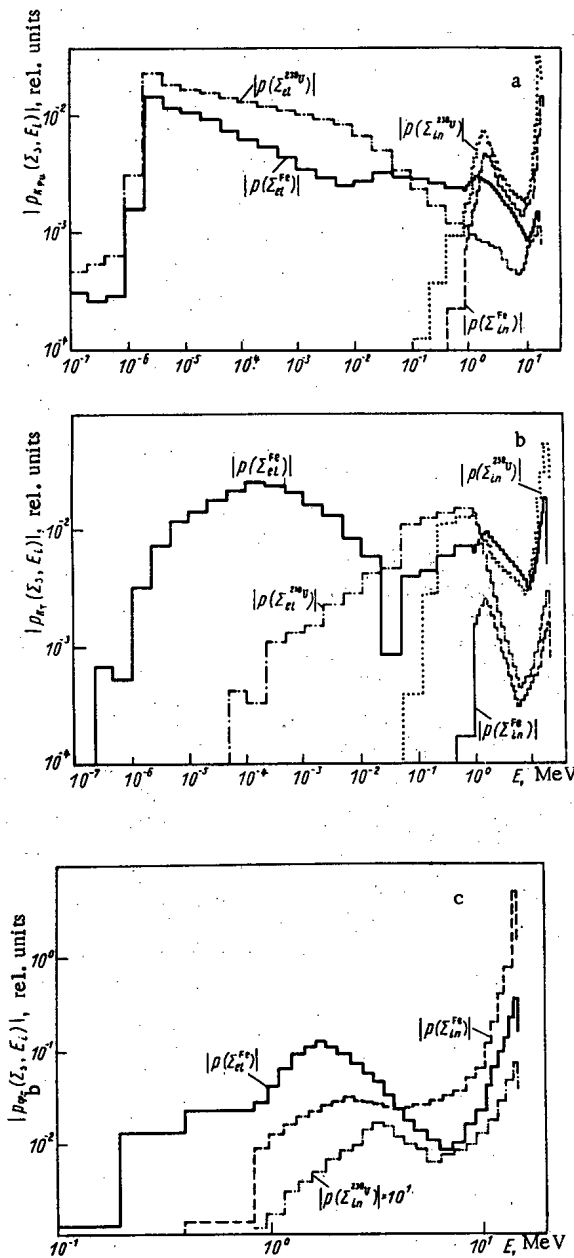


Fig. 4

Fig. 4. Energy dependence of relative sensitivity of a) K_{Pu} ; b) K_T ; c) ϕ_b to variations of the elastic and inelastic scattering cross sections of ^{238}U , Fe and Pb.

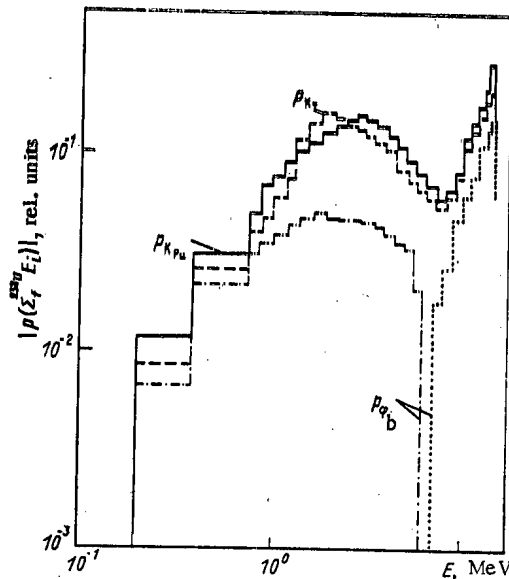


Fig. 5. Energy dependence of relative sensitivity of K_{Pu} (—), K_T (---), φ_b (··· and - · -) to variations in the ^{238}U fission cross section for $p > 0$ (— ; --- ; - · -) and $p < 0$ (···).

The $^6Li(n, \alpha)T$ cross section is small for fast neutrons except for the 0.2-0.4 MeV group which contains the resonance region (0.25 MeV), although even in this group it is much smaller than the total macroscopic cross section. Neutrons in this group make up to a 5% contribution to K_T , which causes a maximum of $p_{K_T}(\Sigma_R)$; $p_{K_T}(\Sigma_R)$ is larger than $p_{K_T}(\Sigma_a^{Li})$ over the whole energy range. K_{Pu} , and particularly φ_b , are insensitive to variations of the Σ_a^{Li} cross section.

Scattering Cross Section. Because of the complex character of the cross sections, the composition of the heterogeneous model of the blanket and shield, the neutron spectra, and the response functions, general rules cannot be given for the energy dependence of the sensitivity of K_{Pu} , K_T , and φ_b to variations of the scattering cross sections (Fig. 4). The values of $p_{K_{Pu}}(\Sigma_s^i, V_m)$ and $p_{K_T}(\Sigma_s^i, V_m)$ in neighboring groups may differ in sign as well as in magnitude. We note the large absolute values of $p_{K_{Pu}}(\Sigma_s^i)$, $p_{K_T}(\Sigma_s^i)$, and $p_{\varphi_b}(\Sigma_s^i)$. Analysis of $p(\Sigma_{el,l}^{Fe})$ showed that K_{Pu} , K_T , and φ_b are insensitive to variations of the elastic slowing down cross section for intermediate and heavy nuclei. This is important, since these cross sections depend very strongly on the shape of the averaging spectrum in the preparation of the group cross sections. The values of K_{Pu} and K_T are insensitive to the nonzero harmonics of the scattering cross section, but φ_b is quite sensitive. Thus, for $\Sigma_{el,l}^{Fe}$, $p(\Sigma_{el,l}^{Fe}, l=0) = -6.36$; $p(\Sigma_{el,l}^{Fe}, l=1) = 1.31$; $p(\Sigma_{el,l}^{Fe}, l=2) = 0.57$, ..., $p(\Sigma_{el,l}^{Fe}, l=5) = 0.03$. The hard neutron source spectrum makes the functionals of the neutron distribution sensitive to variations of the inelastic scattering cross sections of uranium, lead, and, to a lesser degree, iron. The appreciable uncertainties in these cross sections made a very large contribution to the error of the calculated values of φ_b , K_T , and K_{Pu} . For φ_b the sensitivity to a variation of the energy distribution of neutrons after inelastic scattering is particularly great. For K_T , except for cross sections for transfer from groups with energies above 10 MeV into the 0.2-0.4 MeV group in which the values of $p_{K_T}(\Sigma_{in}^j)$ reach 0.048 and 0.065 for lead and lithium respectively, and K_{Pu} , the energy distribution of neutrons after inelastic scattering is unimportant.

Fission Cross Section. More than 80% of the fissions in the hybrid blanket occur in ^{238}U nuclei, i.e., at neutron energies above 0.1 MeV; the function $p_{K_{Pu}}(\Sigma_f^{238U})$ is positive over the whole energy range (Fig. 5). The neutron importance functions for K_T and φ_b have a harder spectrum in the uranium blanket, which causes a decrease in $p_{K_T}(\Sigma_f)$ and $p_{\varphi_b}(\Sigma_f)$ for $E > 1.5$ MeV and their negative values for energies above 6-7 MeV (Fig. 5). The total sensitivity of K_T and K_{Pu} to variations in Σ_f is positive [$p_{K_{Pu}}(\Sigma_f) = 1.4$, $p_{K_T}(\Sigma_f) = 1.03$] and negative for φ_b [$p_{\varphi_b}(\Sigma_f) = -0.7$].

Total Cross Section. Since $p_R(\Sigma_\kappa)$ may have different signs for different partial cross sections κ , $p_R(\Sigma_t)$ is insensitive. A different dependence is found for φ_b . Here $p(\Sigma_\kappa)$ is negative everywhere except for Σ_f for $E < 0.8$ MeV. Therefore $p_{\varphi_b}(\Sigma_t)$ is rather large; $p_{\varphi_b}(\Sigma_t^{Fe}) = -4.68$; $p_{\varphi_b}(\Sigma_t^U) = -1.63$; $p_{\varphi_b}(\Sigma_t^{Pb}) = -1.2$.

Data on the relative sensitivity of a functional to variations of the total cross section of a specific element and the total macroscopic cross section of the medium can be interpreted as the relative sensitivity of R to variations of the concentration of the given element or the density of the material. The latter can be used to solve design changes.

The uncertainties in certain characteristics of the interaction cross sections can reach 20–30%. This causes certain difficulties in the use of sensitivity data obtained within the framework of linear perturbation theory. The reliability of the estimate of the variation of a functional can be increased by using an exponential model for $\Delta R/R$ described in [10].

The sensitivity analysis performed showed the need for further research on the effect of uncertainties in the energy and angular distributions of secondary particles – neutrons and photons – on the design characteristics of a thermonuclear reactor blanket and shield. Such studies can be based on the design systems mentioned above.

LITERATURE CITED

1. V. V. Kotov et al., Preprint IAE-2817, Moscow (1977).
2. M. Yousseff, R. Conn, and C. Maynard, Nucl. Technol., 2, 648 (1982).
3. V. V. Bolyatko et al., in: Numerical Solution of the Transport Equation in One-Dimensional Problems [in Russian], Inst. Prikl. Mat. Akad. Nauk SSSR, Moscow (1981), p. 202.
4. T. A. Germogenova et al., *ibid.*, p. 222.
5. S. V. Marin, D. V. Markovskii, and G. E. Shatalov, Preprint IAE-2532, Moscow (1977).
6. M. Yu. Vyorskii et al., At. Energ., 53, No. 2, 113 (1982).
7. L. N. Zakharov et al., Preprint IAE-2994, Moscow (1977).
8. S. M. Zakharov, B. N. Sivak, and G. I. Toshinskii, in: Bulletin of Nuclear Data Information Center, No. 3, App. 1 [in Russian], Atomizdat, Moscow (1967).
9. L. I. Abagyan et al., Group Constants for Designing Reactors and Shields [in Russian], Énergoizdat, Moscow (1981).
10. V. V. Bolyatko et al., Errors of Calculations of a Shield Against Ionizing Radiations [in Russian], Énergoizdat, Moscow (1983).

SPATIAL DISTRIBUTIONS OF DOSE FIELDS IN A WATER ABSORBER BOMBARDED WITH HIGH- ENERGY NUCLEONS

A. Ya. Serov, B. S. Sychev,
E. P. Cherevatenko, and S. V. Chernov

UDC 621.039.538

In order to solve a number of problems of beam therapy, in particular to determine the optimum irradiation conditions when narrow beams of high-energy nucleons are used, it is necessary to have quantitative information about the characteristics of the dose field in the absorber, both in the region of the beam and beyond its limits. In this paper we present some results of investigations of the laws governing the formation of the spatial distribution of the absorbed and equivalent doses in a water absorber, irradiated with a narrow beam of neutrons and protons. The results of calculations are compared with the data of [1] which were obtained for a standard geometry as well as with the results of measurements in the neutron medical beam at the Laboratory of Nuclear Problems at the Joint Institute for Nuclear Research (JINR) [2].

Method of Calculation. In this paper we consider a cylindrical water absorber with a thickness of 30 cm and a radius r_a . The beam of particles is oriented perpendicularly to the end surface of the absorber. The cross section of the beam is a circle of radius r_0 and the beam axis coincides with the central axis of the cylinder. The particle distribution over the area of the beam cross section is assumed to be uniform. The results of the calculations of the two-dimensional distributions have been normalized to one primary particle in the cross-sectional area of the beam. The space-energy distribution of secondary hadrons formed as a result of

Translated from Atomnaya Énergiya, Vol. 56, No. 1, pp. 36-40, January, 1984. Original article submitted August 25, 1983.

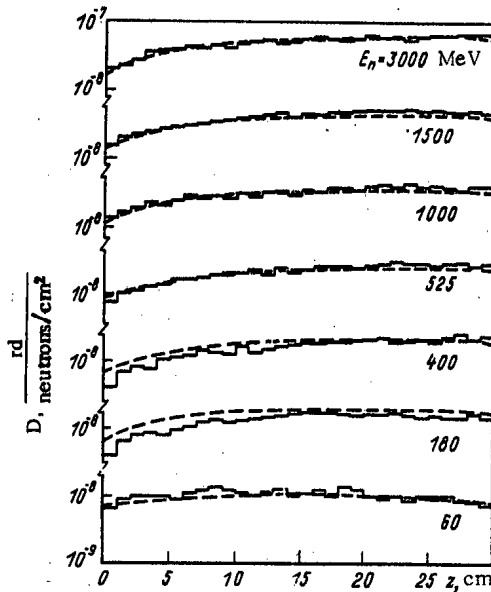


Fig. 1

Fig. 1. Depth distributions of dose absorption D ($1 \text{ rd} = 0.01 \text{ Gy}$) for a standard geometry (E_n is the energy of monoenergetic neutrons): the histogram represents the calculated data of [1] and the dashed curve represents the calculation of this paper.

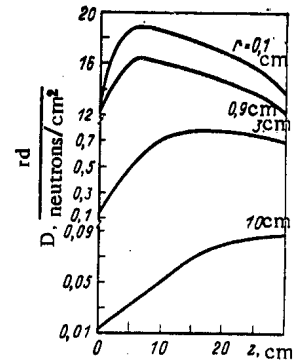


Fig. 2

Fig. 2. Spatial distribution of the absorbed dose D in water for monoenergetic neutrons for different values of r .

the development of an internuclear cascade in the absorber was calculated within the framework of the method of successive collisions [3]. In a cylindrical geometry the radiation field is characterized by the particle distribution function $\Phi(r, z, \theta, \psi, E)$ which is presented in the problem under discussion in the form of a series, with the first three terms of the expansion taken into account:

$$\Phi_i(r, z, \theta, \psi, E) = \sum_{n=1}^3 \Phi_i^{(n)}(r, z, \theta, \psi, E), \quad (1)$$

where $\Phi_i^{(n)}(r, z, \theta, \psi, E)$ is the distribution function of particles of type i , calculated from the recurrence relation

$$\begin{aligned} \Phi_i^{(n)}(r, z, \theta, \psi, E) = & 2 \sum_j \int_{\theta_{\min}}^{\theta_{\max}} \text{tg } \theta' d\theta' \int_0^{\psi_{\max}} d\psi' \int_{E_{\min}}^{E_{\max}} dE' \int_{z_{\min}}^{z_{\max}} \Phi_j^{(n-1)}(r', z', \theta', \psi', E') \times \\ & \times \left[\sum_h \eta^{(h)} \sum_j^{(h)}(E') \frac{d^2 N_j^{(h)}}{dE d\Omega} - (E' \rightarrow E^*) \right] f_i(z, z', \theta, E, E^*) \frac{\beta_i(E^*)}{\beta_i(E)} dz'. \end{aligned} \quad (2)$$

Here $i = n, p, \pi^\pm, \pi^0$ (e^\pm), $j = n, p, \pi^\pm, \eta^{(k)}$ is the mass content of the k -th element ($\sum \eta^{(k)} = 1$), $\Sigma_j^{(k)}(E)$ is the macroscopic cross section of the inelastic interaction of a particle of type j with nuclei of the k -th element,

$\frac{d^2 N_j^{(h)}}{dE d\Omega}(E' \rightarrow E^*)$ is the twofold differential distribution of particles α of type i with an energy E^* which are

formed when particles of type j with an energy E' interact with a nucleus of the k -th element, α is the angle between the directions of motion of the primary (j) and secondary (i) particles, $f_i(z, z', \theta, E, E^*)$ is a function describing the transport of a particle from the point of formation to the point of observation, and $\beta_i(E)$ are the specific ionization energy losses by a particle of type i ; for neutrons and π^0 mesons $E^* = E$ while for charged particles E^* is found from the relation

$$R_i(E^*) = R_i(E) + \frac{z-z'}{\cos \theta},$$

where $R_i(E)$ is the ionization mean free path for a particle of type i with an energy E . The limits of integration in Eq. (2) are determined from the geometrical relations. Integration was carried out not over the whole of phase space but only over those regions outside of which the contribution is negligible.

The space-energy distribution of the fluence of particles was obtained by convoluting the distribution functions with respect to the angular variables:

$$F_i(r, z, E) = 2 \int_{\theta_{\min}}^{\theta_{\max}} \sin \theta d\theta \int_0^{\psi_{\max}} \Phi_i(r, z, \theta, \psi, E) d\psi. \quad (3)$$

The transition from the space-energy distribution (3) to a space distribution of the dose was effected as follows. The total absorbed dose at any point of the absorber is determined by the sum

$$D_{\Sigma}(r, z) = D_{p1}(r, z) + D_{p2}(r, z) + D_{\pi^{\pm}}(r, z) + D_{\pi^0}(r, z) + D_{p^*}(r, z) + D_h(r, z) + D_{\gamma}(r, z), \quad (4)$$

where $D_{p1}(r, z)$, $D_{p2}(r, z)$, $D_{\pi^{\pm}}(r, z)$ is the dose due to the ionization stopping of the primary protons, high-energy secondary protons, and charged π -mesons;

$$D_i(r, z) = \int_{E_1}^{E_{\max}} F_i(r, z, E) \beta_i(E) dE; \quad (5)$$

$$i = p1, p2, \pi^{\pm},$$

where E_1 is the minimum energy in the spectra of primary particles ($E_1 = 4$ MeV), and $D_{\pi^0}(r, z)$ is the dose due to electrons and positrons which are formed as a result of the development of an electron-photon shower initiated by γ -quanta from the decay of π^0 -mesons. It was assumed that π^0 -mesons decay at the point of their formation and as a result of the decay two γ rays are emitted in the direction of motion of the π^0 -meson. In calculating $D_{\pi^0}(r, z)$ we used analytic expressions for the cascade curves of the ranges of electrons in a one-dimensional geometry.

The last three terms in expression (4), $D_{p^*}(r, z)$, $D_h(r, z)$ and $D_{\gamma}(r, z)$, denote the contribution to the dose from low-energy secondary nucleons (n, p), heavy charged particles (d, t, ^3He , α), as well as elastically scattered recoil nuclei of oxygen from the water and the γ rays formed in the stage when the residual excitation of the oxygen nuclei is removed:

$$D_i(r, z) = \sum_l \int_{0.1 \text{ MeV}}^{40 \text{ MeV}} E dE \int_{E_1}^{E_{\max}} \sum_{j=n, p, \pi^{\pm}} F_j(r, z, E') \eta^{(0)} \sum_j^{(0)}(E') \frac{dN_l^{(0)}}{dE}(E, E') dE', \quad (6)$$

where $dN_l^{(0)}/dE$ is the energy spectrum of low-energy particles of type l : when $i=p^*$ the particles $l=n, p$ and when $i=h^*$ the particles $l=d, t, ^3\text{He}, \alpha$;

$$D_h(r, z) = D_{h^*}(r, z) + D_O(r, z);$$

$$D_O(r, z) = \sum_{j=n, p, \pi^{\pm}} \int_{E_1}^{E_{\max}} F_j(r, z, E) \sum_j^{e1}(E) \bar{E}_O(E) dE, \quad (7)$$

where $\sum_j^{e1}(E)$ is the macroscopic cross section for the elastic interaction of hadrons with an oxygen nucleus, $\bar{E}_O(E)$ is the average energy of an oxygen recoil nucleus;

$$D_{\gamma}(r, z) = \sum_{j=n, p, \pi^{\pm}} \int_{E_1}^{E_{\max}} F_j(r, z, E') \eta^{(0)} \sum_j^{(0)}(E') E_{\gamma} dE',$$

where E_{γ} is the energy carried from the nucleus by the γ rays. It was assumed that the energy of all low-energy particles and oxygen recoil nuclei are absorbed locally at the point of their formation.

The differential distributions of the cascade and low-energy particles formed in inelastic hadron-nuclear interactions, were calculated from the approximation expressions in [4, 5].

The equivalent dose $D_{\text{equiv}}(r, z)$ was calculated using the radiation quality factors determined in accordance with the recommendations of [6]. For charged particles with a linear energy transfer (LET) > 3.5 keV/ μm we used the recommended dependence of the quality factor on the LET of particles in water [7]. The quality factor for the oxygen recoil nucleus was taken to be 20.

The formalism presented above served as the basis for the computing program MEDICA which was used to calculate the characteristics of the dose field in a water absorber.

Results of Calculation in a One-Dimensional Geometry. Figure 1 gives the depth distribution of dose absorption in an absorber irradiated with monoenergetic neutrons with an energy ranging from 60 to 3000 MeV.

TABLE 1. Spatial Distribution of the Quality Factor in an Absorber upon Irradiation with a Beam of Monoenergetic Neutrons for $E_n = 525$ MeV and $r_0 = 1$ cm *

r, cm	z, cm					
	0	6	12	18	24	30
0,1	6,06	4,42	4,33	4,29	4,26	4,46
0,5	6,09	4,52	4,42	4,38	4,34	4,55
0,9	6,21	4,86	4,72	4,66	4,62	4,82
1,5	2,30	1,84	1,80	1,79	1,78	1,69
3,0	2,42	1,93	1,84	1,81	1,78	1,70
10	2,50	2,17	1,99	1,89	1,82	1,75
20	2,56	2,35	2,18	2,05	1,95	1,88
40	2,74	2,62	2,50	2,39	2,28	2,20
K(z)	4,62	3,00	2,72	2,59	2,50	2,44

* $K(r, z) = D_{\Sigma}^{equiv}(r, z) / D_{\Sigma}(r, z)$; $K(z) = D_{\Sigma}^{equiv}(z) / D_{\Sigma}(z)$.

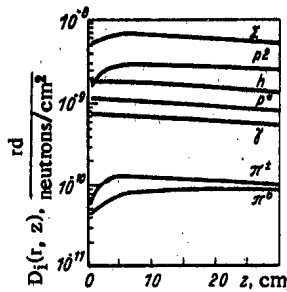


Fig. 3

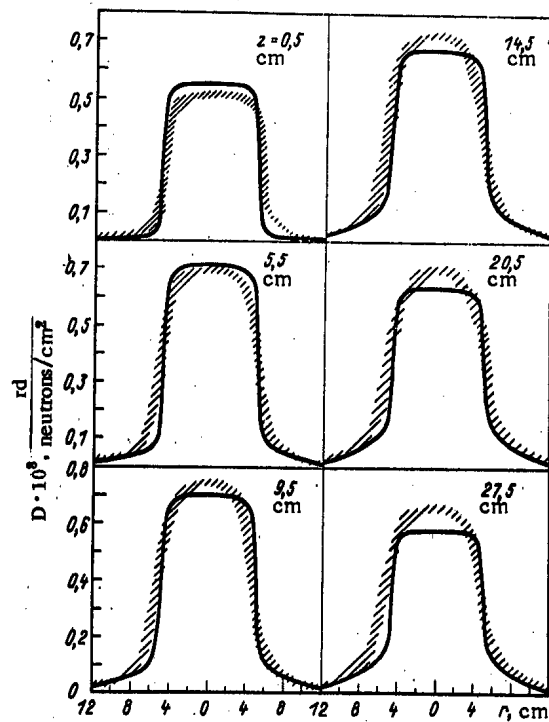


Fig. 4

Fig. 3. Depth distributions of the absorbed dose and its components in the zone of a beam of neutrons generated from a beryllium target by neutrons.

Fig. 4. Radial distributions of the absorbed dose at different depths of the phantom and for different z: - - -) experiment; —) calculation in this paper.

The results of our calculations are compared with the data of [1], which were obtained for a standard geometry (a wide beam of monodirectional radiation with a particular energy falls perpendicularly onto a phantom in the form of a semiinfinite layer 30 cm thick). Our calculation was carried out for absorber radii r_a of up to 40 cm. As shown by the calculation, a further increase in the absorber radius does not result in any major change in the depth distributions (the contribution to the depth distribution from the peripheral region with a radius r_a ranging from 30 to 40 cm amounts to about 3%).

The depth distributions of the absorbed dose are in satisfactory agreement with each other. The equivalent doses calculated by this method are 15-30% lower than those calculated in [1]. This difference is apparently due to the fact that in [1] the quality factor was taken to be 20 for all heavy low-energy particles, regardless of their energies.

The results of our calculations for primary protons with an energy of 400-3000 MeV differ from the data of [1] by no more than in the case of primary neutrons (see Fig. 1).

Comparison of the depth distributions of the absorbed dose of neutrons ($E=10$ GeV) with the data of [8, 9] shows that the depth distributions obtained in this paper are substantially closer to the results of the calculation in [9], the difference being no more than 25%.

Results of Calculation for Two-Dimensional Geometry. Figure 2 and Table 1 present data which characterize the spatial distribution of the absorbed dose and the quality factor for neutrons with $E_n=525$ MeV at a beam radius $r_0=1$ cm. It is seen that the shape of the depth distributions depends essentially on the coordinate r (the distance from the beam axis). Thus, the distribution in the zone of the beam is characterized by a maximum at a depth of ~ 6 cm while at a radius $r=10$ cm the maximum dose is attained at a depth of 30 cm. As follows from Table 1, the value of the quality factor varies over the volume of the absorber from 6.21 to 1.69, this being a consequence of the nonuniformity of the spatial distribution of the absorbed and equivalent dose components.

For primary protons with $E=1000$ MeV and $r_0=0.564$ cm we have obtained data characterizing the distribution of the absorbed and equivalent dose due to the primary and secondary radiation at a depth $z=12$ cm of a water absorber. It was established that in the zone of the beam the dose due to the secondary radiation is $\sim 16\%$ of the total absorbed dose and $\sim 45\%$ of the total equivalent dose.

Comparison with Experimental Results. The calculated data, given in Figs. 3 and 4, were obtained for the specific geometry of the experiment in [2]: A water phantom was irradiated with a beam ($r_0=5$ cm) of neutrons generated in a beryllium target with a thickness of 36 cm under the action of protons with $E=645$ MeV. In the calculation we used data on the energy spectrum of the neutrons produced [2] and the measured neutron flux density at the front face of the absorber, normalized to a unit neutron fluence with the assumption of a uniform distribution of particles over the area of the beam.

Figure 3 presents the calculated data on the depth distribution of the absorbed dose and its components in the zone of the beam ($r=1$ cm). It is seen that the main contribution to the dose comes from cascade protons and low-energy heavy particles. Comparison of the calculated and experimental data on the radial distribution of the absorbed dose for six values of the depth (see Fig. 4) shows satisfactory agreement with respect to both the shape and absolute value.

Principal Results. On the basis of the method of successive collisions, a method has been developed for the numerical calculation of two-dimensional spatial distributions of the dose of radiation in a water phantom, bombarded with a beam of nucleons with an energy ranging from 0.05 to 10 GeV. The method of calculation has been realized in the form of the computing program MEDICA. The results obtained are in satisfactory agreement ($\pm 20\%$) with published calculated data for the conditions of a standard geometry and with experimental data for a neutron beam of finite size. A detailed description of the acting energy spectra of charged particles makes it possible, using the recommended values of the quality factor, to calculate the equivalent dose of radiation. The method developed can be effective and informative for the calculation of microdosimetric distributions as well as in problems of predicting radiation conditions in beam therapy, if use is made of the corresponding dependences of the coefficient of relative biological effectiveness on the form of the particles and their linear energy transfer.

LITERATURE CITED

1. R. Alsmiller, T. Armstrong, and T. Coleman, Nucl. Sci. Eng., 42, 376 (1970).
2. A. Ya. Serov, Yu. S. Sychev, and E. P. Cherevatenko, Preprint No. 18-80-540, Joint Institute for Nuclear Research, Dubna (1980).

3. E. K. Gel'fand, A. Ya. Serov, and B. S. Sychev, in: *Charged Particle Accelerators* [in Russian], Tr. Radiotekh. Inst. Akad. Nauk SSSR, No. 20, 136 (1974).
4. A. Ya. Serov and B. S. Sychev, in: *Charged Particle Accelerators* [in Russian], Tr. Radiotekh. Inst. Akad. Nauk SSSR, No. 14, 173 (1973).
5. B. S. Sychev, A. Ya. Serov, and B. V. Man'ko, Preprint 799, Radio-Engineering Institute, Academy of Sciences of the USSR, Moscow (1979).
6. *Recommendations of the ICRP, Publication 21*, Pergamon Press, Oxford (1971).
7. A. I. Vikhrov et al., in: *Atlas of the Dose Characteristics of External Ionizing Radiation* [in Russian], Atomizdat, Moscow (1978), p. 6.
8. T. Armstrong and K. Chandler, ORNL-3758, Oak Ridge (1972).
9. V. T. Golovachik et al., Preprint ORZ 74-58, Institute of High-Energy Physics, Serpukhov (1974).

FUSED SILICA IN IONIZING-RADIATION DOSIMETRY

R. R. Gulamova, N. A. Kasimov,
and M. I. Muminov

UDC 539.12.03

Existing solid-state dosimeters, in particular ones based on glasses, measure absorbed dose in the main up to 10^6 rad (1 rad = 0.01 Gy) [1-3]. It is necessary to extend the range to 10^7 - 10^9 rad for engineering dosimetry and materials sciences researches. For this purpose we have previously examined the optical characteristics of various grades of fused silica and have considered the scope for using them for the dosimetry of γ rays, γ -neutron radiation, and protons [4-7]. The present paper deals with the dosimetric characteristics and applications of dosimeters based on fused quartz.

The specimens were irradiated with ^{60}Co γ rays with a system at the Institute of Nuclear Physics, Academy of Sciences of the Uzbek SSR, at dose rates of 30-4000 R/sec (1 R = 2.58×10^{-4} Cu/kg), on a VVR-SM reactor at neutron flux densities of 1.8×10^{12} - 3×10^{13} $\text{cm}^{-2} \cdot \text{sec}^{-1}$, and with the proton beam from a U-150-11 cyclotron extracted into the atmosphere having a particle energy of 10-20 MeV at flux densities of 6×10^9 - 3×10^{11} $\text{cm}^{-2} \cdot \text{sec}^{-1}$.

The induced absorption spectra were measured for electrically fused silica type KI, and also for gas-fused types KV and KU-2, as well as vapor synthetic silica KU-1, which showed that the form of the radiation did not alter the general picture. The γ rays, mixed reactor radiation, and proton beams produced induced bands at wavelengths of 215, 240, 300, and 500 nm, whose positions and intensities were dependent on the grade of the silica and the amounts of impurities [1-4]. The impurity levels were determined by neutron activation and are given in Table 1.

The dosimetric parameter was taken as the change in optical density at 550 nm as referred to unit thickness for KI fused quartz or at 215 nm for KV, KU-2, and KU-1. It was found that γ rays produced absorption in KI silica at 550 nm whose intensity increased monotonically with the dose and tended to saturation at 10-30 Mrad which is characteristic of impurity centers (Fig. 1).

A similar dependence of the optical density at 550 nm on the absorbed energy was observed with the mixed reactor radiation and the proton beam (Fig. 1). The optical density at 550 nm increased with the neutron and proton doses and attained saturation at fluences of about 10^{16} neutrons/ cm^2 or 10^{14} proton/ cm^2 correspondingly. The kinetic curves for the accumulation and annealing of the color centers produced by ^{60}Co γ rays and mixed reactor radiation showed that the rates of formation and thermal bleaching were the same in the two cases. The induced absorption at 550 nm observed at fluences less than 10^{16} neutrons/ cm^2 is due to the γ component of the reactor radiation [7].

The optical density of KI silica acted on by protons ($E_p = 20$ MeV) agreed with the analogous values for specimens irradiated by γ rays with an error of 30% (Fig. 1). Exposure to protons with $E_p \leq 10$ MeV resulted in a certain reduction in the effectiveness of color-center formation at 550 nm by comparison with γ rays evidently because of the increased proton concentration in small volumes on account of the short particle range and suppression of the color-center formation at 550 nm [2].

Translated from *Atomnaya Energiya*, Vol. 56, No. 1, pp. 40-43, January, 1984. Original article submitted April 13, 1983; revision submitted July 25, 1983.

TABLE 1. Impurity Contents of Fused Silica Specimens, Mass %

Grade*	Na	K	Cl	OH
KI:				
a	$1,6 \cdot 10^{-2}$	$3 \cdot 10^{-1}$	—	—
b	$1,6 \cdot 10^{-3}$	$6 \cdot 10^{-2}$	—	—
c	$2,5 \cdot 10^{-3}$	$3,7 \cdot 10^{-2}$	—	—
KV	$(0,3 - 13) \cdot 10^{-4}$	$(2 - 6) \cdot 10^{-8}$	—	0,02
KU-1	$(0,3 - 12) \cdot 10^{-4}$	$\sim 10^{-8}$	$\sim 10^{-4}$	0,10

*a) KI fused silica melted from synthetic quartz; b) KI fused silica melted from Brazilian quartz; c) KI fused silica melted from Volynia quartz.

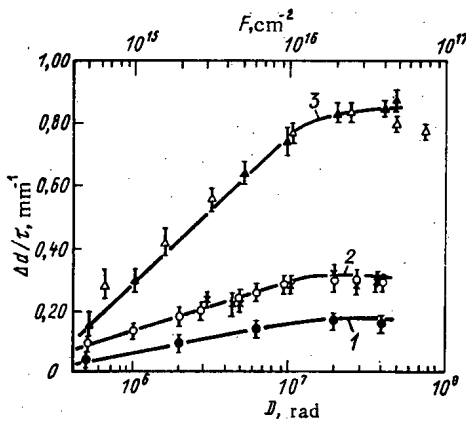


Fig. 1

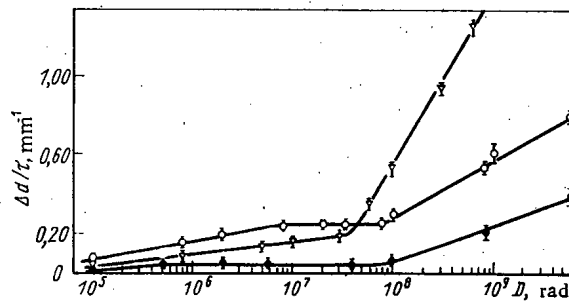


Fig. 2

Fig. 1. Reduced optical density $\Delta d/\tau$ at 550 nm for KI fused silica made from synthetic quartz (1), Brazilian quartz (2), and Volynia quartz (3) in relation to absorbed dose and fluence F ; ●, ○, and ▲) ^{60}Co γ radiation; ×) protons with $E_p = 20$ MeV; △) γ -neutron reactor radiation.

Fig. 2. Dependence of the reduced optical density $\Delta d/\tau$ for the following grades of fused silica: KV (○), KU-2 (●), and KU-1 (▽) at 215 nm as a function of absorbed dose D of ^{60}Co γ radiation (dose rate 3300 R/sec).

The optical density at 215 nm also increases with the absorbed energy for the hydrogen-bearing silicas KV, KU-2, and KU-1, but the rates of accumulation in these differ in the various dose ranges (Figs. 2 and 3). The curves relating the optical density to the absorbed dose showed kinks with the γ rays and neutrons. It is likely that the color centers are produced in the initial stages of irradiation at the sites of defects in the initial silica, while in the later stages (at doses of $5 \times 10^7 - 10^8$ rad of fluences of $>10^{16}$ neutrons/cm²) a contribution is made by defects of radiation origin [8, 9].

There was a more rapid increase in the optical density at 215 nm as the neutron fluence increased in γ -neutron irradiation, and there was no saturation region on the dose curve such as is characteristic of γ -irradiated specimens, which indicates that the induced absorption of reactor irradiation is possibly more dependent on the neutrons. The ultraviolet absorption spectra produced by γ rays and protons show optical densities at 215 nm produced by protons as being higher than those from γ irradiation at the same dose, which is due to the more effective formation of structural defects, which are responsible for absorption in the C bank, when protons are used. Therefore, when KV silica is used to determine absorbed proton energy, it is necessary to perform a preliminary calibration by means of standard dosimeters.

The mixture composition and method of melting the silica influence the magnitude and dose dependence of the absorption. The KI silica was the most radiation-sensitive, and therefore the fused silica promising for use in dosimeters is that made from Volynia quartz, which has high contents of Na and K but no hydroxyl (Fig. 1).

TABLE 2. Reduced Optical Density of Fused Silica at Various ^{60}Co γ -Ray Dose Rates

Grade	Wave-length, nm	Dose rate, R/sec	Dose, rad	Optical density
KI *	550	80	10^7	0,80
		600		0,79
		1800		0,79
		4000		0,79
KV	215	80	$5 \cdot 10^6$	0,50
		600		0,51
		1000		0,50
		1700		0,52
KU-1	215	4200	$6,6 \cdot 10^7$	0,50
		80		0,49
		600		0,50
		1700		0,50
		4200		0,51

*The KI specimens were made from Volynia quartz.

TABLE 3. Reduced Optical Densities of KI Fused Silica at 550 nm for Various Irradiation Temperatures with a Dose Rate of 1000 R/sec

Dose, rad	Irradiation temp., °C				
	40	70	100	120	150
10^6	0,21	0,22	0,22	0,21	0,21
10^7	0,73	0,73	0,73	0,75	0,72

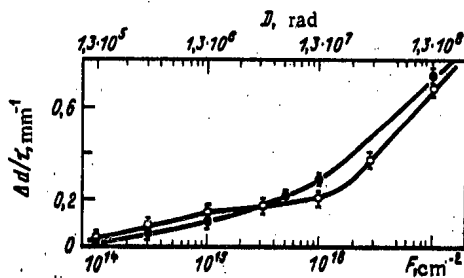


Fig. 3.

Fig. 3. Dependence of the reduced optical density $\Delta d/\tau$ for the following grades of fused silica: KV (○), and KU-1 (●) of the fluence F of mixed γ -n radiation at neutron flux density of 1.8×10^{13} neutrons/cm 2 · sec.

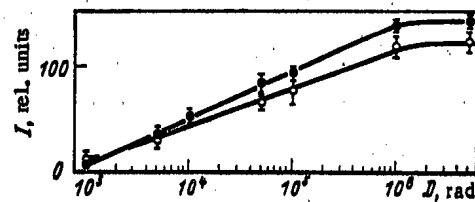


Fig. 4.

Fig. 4. Dependence of the intensity of the thermoluminescence peak at 110-140°C on the absorbed ^{60}Co γ -ray energy at a dose rate of 1000 R/sec for fused silica KI (●) and KV (○).

To extend the absorbed-dose range to 10^8 rad, we examined the thermoluminescence of KI, KV, and KU-1 specimens. The intensities from KI and KV in the range 10^3 - 10^6 rad were in proportion to the absorbed dose (Fig. 4).

It was found that there was no effect on the color-center formation rate, at least as regards the absorption at 215 and 550 nm (Tables 2 and 3), on varying the dose rate between 30 and 4000 R/sec, and the flux densities between 1.8×10^{12} and 3×10^{13} neutrons/cm 2 · sec or from 6×10^9 to 3×10^{11} protons/cm 2 · sec, and the same applies for irradiation temperatures between 40 and 150°C. There is no postirradiation effect over a period of 6 months for KI, while KV and KU-1 showed a slight reduction in the optical density in the first day (about 7%), with no change on further storage. The KI specimens were annealed completely in an hour at 450°C, but KV and KU-1 required 900°C.

We also consider the scope for using the dosimeters repeatedly. It was found that the reproducibility in reuse after annealing was better than $\pm 8\%$.

This reproducibility was obtained in repeated experiments, and it is reliable and does not conflict with the physical nature of the phenomena. The model has been formulated for the formation of E' centers responsible for the absorption in the 215-nm band in KV and KU-1 specimens [10]. The dosimetric reproducibility given here relates to the high-dose region (over 5×10^7 - 10^8 rad), where the main mechanism producing E' centers is the breakage of regular $\equiv\text{Si-O-Si}\equiv$ bonds. The formation of E' centers by the breakage of $\equiv\text{Si-H}$ and $\equiv\text{Si-Cl}$ bonds is important at lower doses, with the corresponding changes in the numbers of color centers after heat treatment. In this dose range, the increase in the number of color centers on repeat irradiation after heat treatment at 900°C is not considerable at 8% on account of the removal of gaseous impurities. These conclusions are confirmed by the infrared spectra and the annealing kinetics for various dose ranges.

The results show that fused silica of grades KI, KV, and KU-1 can be used for γ -ray dosimetry in the range 5×10^5 - 10^9 rad. Absorbed γ -ray doses in the range 10^3 - 10^6 rad can be measured from the proportional change in the intensity of the thermoluminescence. Dosimeters based on KI and KV materials can also be used to determine absorbed proton energy at fluences of 10^{11} - 10^{14} proton/cm². The dependence of the induced optical density on the absorbed energy for γ rays is the same as that for neutrons, and KI silica gives a satisfactory basic dosimeter parameter, so this material may be used in determining the γ component of reactor radiation.

These studies have yielded a thermally stable wide-range γ -ray dosimeter based on KI fused silica made from quartz from the Volynia deposit. This dosimeter is simple and reliable in use and can store the data over a prolonged period, and it can also be reused. The following are the basic characteristics of this dosimeter:

- 1) the dosimeter is made as a plane-parallel plate of size $10 \times 10 \times 1$ mm;
- 2) the absorbed γ -ray energy in the range 10^3 - 10^6 rad can be measured from the intensity of the thermoluminescence peak at 110 - 140°C , while in the range 5×10^5 - 2×10^7 rad it can be determined from the induced optical density at 550 nm;
- 3) the readings are stable over the dose-rate range 30-4000 R/sec at working temperatures of 40 - 150°C ;
- 4) the dosimetric information is retained for 6 months;
- 5) the dosimeters are suitable for reuse after annealing at $450 \pm 10^\circ\text{C}$ for 1 h. The agreement between the results on reuse is better than 6% with a probability of 0.95; and
- 6) the relative error in measuring the absorbed dose is $\pm 8\%$ with probability 0.95.

This dosimeter based on KI fused silica has undergone preliminary certification at the All-Union Technical Physics and Electronics Research Institute; metrological tests made on the detector with standard equipments at the Institute have shown that it corresponds to the standardized characteristics laid down by GOST 15546-81.

LITERATURE CITED

1. G. V. Byurganovskaya et al., The effects of Radiations on Inorganic Glasses [in Russian], Atomizdat, Moscow (1968).
2. S. M. Brekhovskikh et al., Principles of Radiation Materials Science for Glass and Ceramics [in Russian], Stroiizdat, Moscow (1971).
3. M. Frank and W. Stolz, Solid-State Ionizing-Radiation Dosimetry [Russian translation], Atomizdat, Moscow (1973).
4. R. R. Gulamova et al., in: Abstracts for the All-Union Seminar on Radiation Phenomena in Wide-Band Optical Materials [in Russian], Fan, Samarkand (1979), p. 47.
5. R. R. Gulamova, N. A. Kasimov, and E. V. Sazonova, Dokl. Akad. Uzb. Nauk SSR, No. 2, 26 (1979).
6. R. R. Gulamova, N. A. Kasimov, and M. I. Muminov, *ibid.*, No. 4, 34 (1980).
7. R. R. Gulamova, N. A. Kasimov, and M. I. Muminov, *ibid.*, No. 8, 20 (1982).
8. L. Sh. Nadirashvili, B. G. Berulova, and S. V. Sobolevskaya, in: Abstracts for the Third All-Union Conference on the Effects of Ionizing Radiation and Light on Heterogeneous Systems, Part 2 [in Russian], Kemerovo (1982), p. 329.
9. A. V. Amosov, V. V. Kornev, and S. F. Malyskin, Fiz. Khim. Stekla, 7, No. 2, 209 (1971).
10. A. V. Amosov and G. T. Petrovskii, Dokl. Akad. Nauk SSSR, 268, No. 2, 391 (1983).

AN APPLICATION PACKAGE FOR PROCESSING
AND ANALYZING DATA ON THE ENVIRONMENT
AND POPULATION HEALTH

E. I. Vorob'ev, V. A. Kornelyuk,
A. S. Kuz'menko, V. Yu. Reznichenko,
and V. L. Shestopalov

UDC 339

A large data volume has to be processed in monitoring the state of the environment and the health of the population in regions where fuel and power systems exist, in particular nuclear power stations. It is necessary to examine inhomogeneous objects of complex structure and the dynamics of stochastic and nonlinear processes. The specific features of the objects and processes make it difficult to establish regularities and tendencies even if the necessary information is available. The corresponding calculations require powerful software based on the latest data-analysis methods. Therefore, the monitoring system should be based on a set of facilities that realize particularly the methods of statistical data analysis [1].

The detailed objects subject to monitoring may vary in accordance with the features of the region, but the structures and processing methods have much in common.

In the design of the corresponding software, it is necessary to choose between creating novel software well adapted to particular conditions in the form of an applications package AP and adaptation of a certain universal AP less adapted to the conditions of a particular task. One of the purposes of this study is to show that the second approach is promising, and it substantially reduces the development costs while improving the performance.

Choice of AP Type. We consider the general specifications for the software for processing data on the state of the environment and public health. All existing data-processing packages can be classified into three groups [2].

Firstly, there are sets of modules to realize the operations and procedures encountered frequently. These are designed to enable the researcher to draw up his own processing programs for the particular situation. A typical representative is the SSP package (Scientific Subroutine Package) [3], which implements not only statistical-analysis methods but also many methods in applied mathematics. All the same, SSP lacks special methods and ones frequently necessary: Economical analysis and the principal-component method are lacking, while variance analysis is weakly represented, there is no nonlinear least-squares method, and there are no subroutines for oblique-angle rotation or factor analysis, etc. Also, strict specifications are laid down for the data, for example the conditioning of matrices, which cannot always be satisfied.

The second group is represented by packages constituting software libraries for a large number of definite cases typical in a particular subject. These include the packages in the BMD series (Bio-Medical Data) [4].

Finally, we have the third group in the form of combined packages, which are software systems providing comprehensive and multipurpose data analysis usually in a narrow area, such as one where almost all cases can be envisaged. A typical representative is the processing package appearing in the Sensor system for alternating biomedical experiments.

These groups represent various degrees of compromise between the desire to ease the work of the researcher and to provide the effective control over the processing. The groups differ in the requirements imposed on the user, the range of possible uses, and the modification simplicity (Table 1).

The means of analysis selected should satisfy the following requirements:

- 1) completeness: all basic processing methods should be available that are required in environmental and population-health monitoring;
- 2) independence: the AP should be usable directly in the operating system without the need for programming in a high-level language.

Translated from *Atomnaya Energiya*, Vol. 56, No. 1, pp. 43-47, January, 1984. Original article submitted October 4, 1983.

TABLE 1. Characteristics of the Main Types of Data-Processing Package

Package type	Typical representative	User requirements (apart from knowledge of content and instructions)	Use	Scope for extension
Set of program modules	SSP	High: elementary conception of the operating system and ability to program in high level languages (FORTRAN, PL/1, and ALGOL)	Very wide	Realizable by user
Library programs	BMD	Medium: elementary conception of operation system	Fairly wide	Realizable by writer
Combinable programs	Sensor	Low	Narrow	Not realizable

3) modularity: the structure should be modular and enable one to extend the package with new algorithms;

4) scope of composition: it should be possible to construct statistical-analysis algorithms by using combinations of various programs in a single computer job; and

5) intelligence: it should be possible to work in interactive mode and to control the data analysis at any stage in order to introduce modifications, and also to define an optimum strategy for obtaining a significant result under conditions of uncertainty over the initial data model. This includes specifications for editing the data and clear-cut result presentation.

It should be borne in mind that the package should be suitable for transfer to computers of standard configuration of the usual types (for example, the unified series).

Choice of Basic AP. We selected the BMD package, which in our opinion satisfies the above requirements. We also took into account the experience in creating the BMDP package, whose main difference from BMD lies in the organization of the job-control language. BMD uses a fixed specification format, whereas a more flexible facility was developed for BMDP: an English-based control language, which naturally led to other differences.

BMDP contains some forms of analysis not included in BMD, such as cluster analysis, reverse step regression, reverse discriminant analysis, variance analysis for repeated measurements, analysis of multidimensional frequency tables, analysis of models for processing omitted values, and a general mixed variance model. Also, certain programs have been modified: More correct statistical estimators have been included, partial correlations and multidimensional regressions are calculated, and the scope for data transgeneration has been extended. The results obtained with one BMDP program can be stored for subsequent analysis by others.

Many users prefer to work with a fixed specification format and avoid the effort involved in studying the control language. From the viewpoint of rapidly changing tasks in the monitoring system, the main advantage of BMD in our view is that the package allows simple development and extension.

We concluded that it is both possible and desirable to use BMD and BMDP to set up a standard package known as Angara on the basis of experimental operation of these packages for the above purposes, and also from a study of other packages used in this area.

The task of the Angara package is to supply those carrying out environmental monitoring and conservation with standard means of data processing applicable to regions where there are large areas of industry, nuclear power stations, and extensive economic activity. Particular attention was given to identifying the commonest of tasks and incorporating their features into the AP structure. We also standardized the procedures for operating with the AP on the basis of the specifications and facilities elsewhere in the monitoring system. This is governed by the variety of users as regards jobs and level of training.

The Angara package was constructed by supplementing and upgrading existing facilities as required in this area (including some that were lacking) while abandoning ones largely unused or irrelevant.

The BMD facilities as regards preliminary analysis were indicated by the authors' experience as being exhaustive and were partially incorporated into the Angara package.

Correlation Analysis. A researcher often needs to analyze the informativeness of the initial system of parameters and to transfer to a new system of smaller dimensions (data compression). This can be handled by programs that implement component analysis. It is also possible to perform regression analysis on the principal components and the dependent variables. A finer tool for analyzing system informativeness is factor analysis, which is a method in multidimensional statistics and also has heuristic features. The corresponding section of BMD was substantially altered on the basis of the significance and effectiveness of factor analysis. New methods were introduced for seeking a factor solution, determining statistical criteria for the quality of the factor solution, and also service facilities for representing the results as graphs and histograms. In developing the package, it was frequently necessary to select the best from several programs intended for the same purposes. As an example of program choice for the Angara package, we consider the choice of facilities for realizing factor analysis (FAN).

We set up the program MODEL, whose output is a matrix for the initial data with a preselected internal structure and which includes a given number of variables, factors, and the correlations between them. We compared the standard FAN program set from the SSP, the BMD08M program, and the F1 program written at Kharkov Technical Physics Institute.

The study enabled us to objectivize the choice of the optimum program. As a result, the Angara package included a hybrid suite combining the best features of the initial programs. This is provided by the BMD08M program with the addition of the necessary criteria from F1.

Model Construction. Experience with complicated systems has shown that one cannot construct models on the basis of a priori arguments alone. System identification involves refining theoretical models by means of experimental data. Regression analysis is a classical identification method. In BMD, this is represented by seven programs to realize stepwise linear regression, nonlinear least squares (this program has means of offsetting the effects of singularities that may arise), polynomial regression, harmonic regression enabling one to use up to nine harmonics, and a linear model with a selection of regressor combinations. At user request, almost all the programs enable one to use a plotter to provide graphs for the theoretical and experimental values.

In the Angara package, the identification methods provided in BMD are supplemented with stochastic approximation, gradient methods, and identification methods based on differential equations.

Identification methods that have become classical presuppose that the system structure is given, whereas problems related to the management of complicated systems do not always enable one to suggest a system structure as a relationship between the measured parameters (environmental monitoring and so on is undoubtedly of this class). In that case, one may reasonably use methods of synthesis and selection (self-organization) in regression models, which is known as the argument grouping method AGM [5], which has been found to be applicable to ecological systems.

The AGM programs and algorithms are used in short-, medium-, and long-range forecasts, system structure identification, pattern recognition, and defining control strategy optimum on a given criterion.

The AGM programs have been included with modifications and improvements in the Angara package. The standard AGM algorithms have been supplemented by introducing stepwise regression and principal-component methods (in the synthesis process). The latter increases the stability in the computational scheme by the use of orthogonal arguments and enables one to discard largely uninformative arguments and reduces the computation time.

Cases are common in ecology where the characteristics change stepwise for certain values of the environmental parameters [6]. The classical example is provided by the numbers of a species in relation to the conditions of life.

In an environmental-monitoring system, it is necessary to envisage qualitative model analysis for stability, particularly structural stability. Numerical methods from catastrophe theory have been introduced into the Angara package and enable one to evaluate the approximation by means of polynomials (the topic is particularly important when AGM is used) and also to define bifurcation sets and so on.

Processing Expert Evaluations. Our experience has shown that the facilities of the BMD package as regards classifications and pattern recognition do not correspond to the requirements for an environmental monitoring system. In the existing form of the Angara package, this is not completely handled. In the main we used programs from the BMD series. The deficiency was eliminated partly by including means of processing expert evaluations in the Angara package (ranking, direct evaluation, pair and serial comparison). For this purpose we used software devised at Kharkov Technical Physics Institute and elsewhere. To provide clarity in representing the results, the system was designed for operation with the Grafor suite, which enables one to use a standard plotter to generate histograms and graphs. The package is mobile and transportable, so it can be used in centers having ES or BESM-6 computers.

Time-Series Analysis. During the experimental operation of the Angara package, it was considered to be relatively important to be able to analyze time series, on account of the increasing importance of the chronological approach in environmental monitoring.

Programs taken from BMD were used in analyzing time series and their correlations. These programs extract harmonic components, evaluate frequency response, generate autocorrelation and cross-correlation spectra, and analyze response functions. The Angara package also has means of determining desynchronism (particularly for Circadian biorhythms). Provision was also made for including the effects of desynchronism arising from low-frequency biorhythms (for example, selenorhythms), although these lack theoretical basis. This enables one to improve the homogeneity of the sample considerably.

Special Programs. Programs for special purposes in data analysis required substantial changes. Those in BMD are designed for classical biological and biomedical treatments. In environmental monitoring, it is particularly important to have special programs for identifying the states of individual body systems, including ones for automating the processing of functional-diagnosis parameters such as a program for processing a heart rhythm that evaluates the harmonic series of R-R intervals by means of the autocorrelation function, the Hemming spectral estimator, a program for pulse processing, and similar ones for other harmonic processes.

The special programs include methods of processing biochemical, immunobiological, and chemical analysis data, as well as means of processing ECG and other automatically recorded curves.

Experience in Use. The Angara package was evaluated during a major biomedical experiment having the purpose of evaluating the changes in state of health for clinically healthy people as bioindicators for slight changes in the environment. A central problem was to select features reflecting the state of health.

In the experiment, each of 500 volunteers recorded a large set of parameters (about 300 including derived ones) corresponding to the specifications of the World Health Organization for routine medical examination of the population: informativeness, availability, comfort, carrying capacity, automation, and ease. The analysis revealed 45 parameters (19 methods) as being most informative as reflecting the state of clinically healthy people. These were used in another biomedical experiment and were subject to further refinement as experience accumulated.

Discussion of these results falls outside the scope of this paper, but the fact that some important practical problems were resolved during it means that the evaluation of the Angara package is good.

The main current problem is to accumulate experience in using these facilities in various areas of research on the environment and population health, and also to formulate individual programs and supplements in the form of a package corresponding to the current requirements.

LITERATURE CITED

1. E. I. Vorob'ev and V. Yu. Reznichenko, *At. Energ.*, 50, No. 4, 243 (1981).
2. Algorithmic and Program Support to Applied Statistical Analysis [in Russian], Nauka, Moscow (1980).
3. ES Computer Software [in Russian], Issue 16, *Izd. Inst. Mat. Akad. Nauk BSSR*, Minsk (1978).
4. W. Dixon (ed.), *Biomedical Computer Programs*, Vols. 1 and 2, University of California Press (1977).
5. A. G. Ivakhnenko et al., *The Self-Organization Method in Decision Theory* [in Russian], Sov. Radio, Moscow (1975).
6. T. Poston and I. Stuart, *Catastrophe Theory and Its Applications* [Russian translation], Mir, Moscow (1980).

RADIONUCLIDE DEFLATION EFFECTS
IN A CONTAMINATED LOCALITY WITH INTERMITTENT
AND STEADY-STATE DISCHARGES INTO THE ATMOSPHERE

K. P. Makhon'ko

UDC 551.510.72:551.515.3

If a contaminated zone is formed in a locality by radionuclide discharge into the atmosphere, this zone may afterwards be a secondary source of contamination of the atmosphere as a result of wind deflation of the radionuclides [1]. The concentration of radioactive dust q_α raised by the wind from the surface of the soil is proportional to the radioactive contamination density A :

$$q_\alpha = k_\alpha A, \quad (1)$$

where k_α is the deflation coefficient. In the present case, the radioactive dust consists of particles of soil bearing the radionuclides, so q_α can be represented as the product of the mass concentration of soil dust in the air C by the bulk concentration of the radionuclide in the surface dust layer \bar{n} [2]. Then from (1)

$$k_\alpha = C\bar{n}/A\rho, \quad (2)$$

where ρ is the density of the surface soil layer.

We consider the consequences of a single radionuclide discharge into the atmosphere. At the start, all the radionuclides are localized at the soil surface in the contaminated zone and $\bar{n} = A/l$ (l is the effective thickness of the surface dust layer). We substitute for \bar{n} into (2) and use (1) to get a formula for the experimental determination of l :

$$l = CA/q_\alpha\rho \quad (t \approx 0). \quad (3)$$

As C and q_α are integral characteristics of the locality as a whole, l also characterizes the locality as a whole, which may include zones with different surfaces. As time passes, the radionuclides migrate from the surface into the soil, which reduces the concentration in the surface dust layer of thickness l . For most soils in their natural state, one can use a linear relationship for the effective diffusion coefficient as a function of depth in the surface layer of 20-30 cm, which enables one to determine the concentration profile $n(x)$ after a single contamination episode by means of the expression from [3] and to transform (2) to

$$k_\alpha = \frac{C e^{-\lambda t}}{\rho \Gamma(1+\nu)(\nu_D t)^{1+\nu}} \int_0^l x^\nu e^{-\frac{x}{\nu_D t}} dx. \quad (4)$$

Here t is time, $\nu = \nu/\nu_D$ is the ratio of the linear downward rate of radionuclide transport to the diffusion rate, λ is the radioactive decay constant, and $\Gamma(1+\nu)$ is the gamma function. In the particular cases of $\nu=0$ (heavy soils or the absence of precipitation) and $\nu=1$ (light soils, through flow), the deflation coefficient can be expressed in analytic form:

$$k_\alpha = \frac{C e^{-\lambda t}}{\rho l} \left(1 - e^{-\frac{l}{\nu_D t}}\right) \quad \nu=0; \quad (5)$$

$$k_\alpha = \frac{C e^{-\lambda t}}{\rho l} \left[1 - \left(1 + \frac{l}{\nu_D t}\right) e^{-\frac{l}{\nu_D t}}\right] \quad \nu=1. \quad (6)$$

Figure 1 shows the variation in deflation coefficient for ^{90}Sr over time as calculated from (4)-(6) for values of ν , ν_D , and $C \approx 30 \mu\text{g}/\text{m}^3$, $\rho \approx 1 \text{ g}/\text{cm}^3$, $l \approx 0.5 \text{ cm}$ typical for undisturbed soils in the central belt of the USSR. The values of k_α decrease with time on light soils ($\nu \approx 1$) more rapidly than for heavy ones ($\nu \approx 0$), and for light soils or for comparatively large ν_D the $k_\alpha(t)$ dependence can be approximated satisfactorily by a simple function of the form $k_\alpha = at^{-b}$. The results for k_α coincide as regards order of magnitude with the value of

Translated from *Atomnaya Energiya*, Vol. 56, No. 1, pp. 47-50, January, 1984. Original article submitted March 24, 1983.

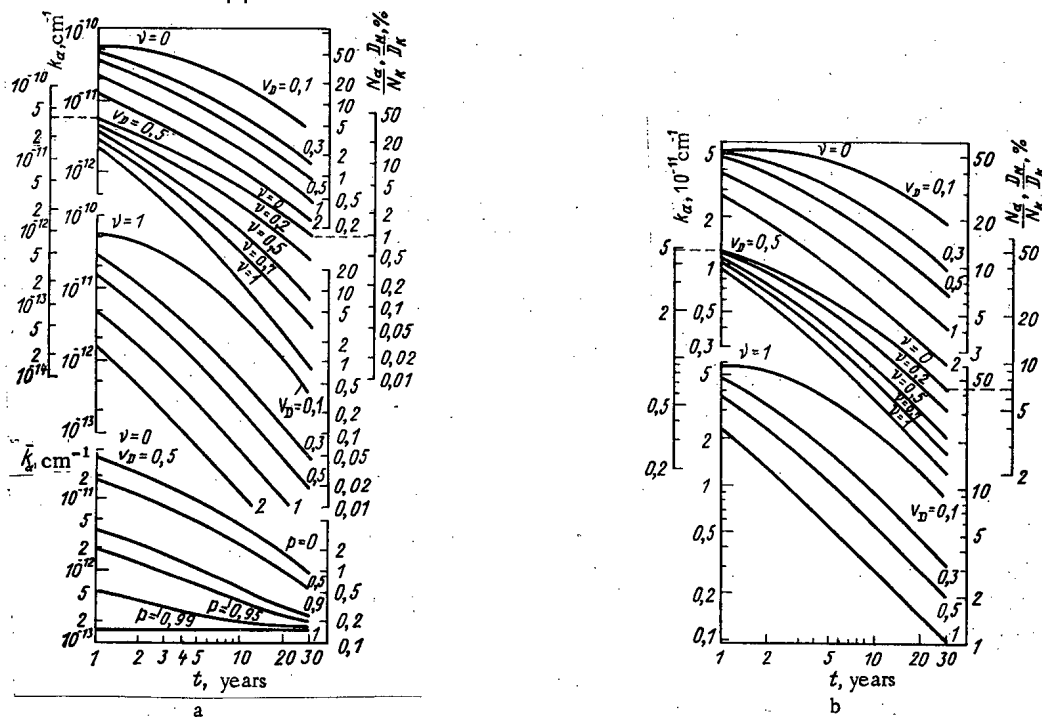


Fig. 1. Variation in deflation coefficient for ⁹⁰Sr over time after a single pollution accident (a) and in the neighborhood of a stationary radionuclide discharge source (b): N_{α}/N_K is the ratio of the aerosol contamination of the grass to the root contamination, while D_N/D_K is the ratio of the internal irradiation dose (via food chains) due to aerial and root entry to the plant.

$3 \times 10^{-12} \text{ cm}^{-1}$ established for the deflation of ^{238,239}Pu from desert soils in the nuclear test zone in Nevada (USA) 20 years after the area was contaminated [4].

So far it has been assumed that there are no plowed areas in the contaminated zone. During plowing, the upper contaminated layer is mixed to the depth H of the plowing. If the radionuclides have not penetrated deeply, then $\bar{n} = A/H$ in (2), and the deflation coefficient is independent of time in the plowed parts:

$$k_{\alpha}^p = C/H\rho. \tag{7}$$

For a locality containing plowed and virgin lands, the mean value of the deflation coefficient may be determined to a first approximation as the weighted mean:

$$\bar{k}_{\alpha} = k_{\alpha}^p p + k_{\alpha} (1 - p), \tag{8}$$

where p is the proportion of plowed land.

Figure 1a shows how \bar{k}_{α} varies with p for $\nu_D = 0.5 \text{ cm/year}$, $\nu = 0$, and $H = 20 \text{ cm}$ [3]. It is clear that in the early years after the formation of a contaminated zone in a region where nearly all the land is plowed, even a small proportion of unplowed areas ($1-p = 1-5\%$) can produce a marked increase in the atmospheric contamination, since k_{α} increases by an order of magnitude or so.

The radionuclides enter the plants in the contaminated zone through the roots from the soil and through the leaf surfaces by the deposition of aerosols raised by the wind. We compare the radionuclide concentration due to the entry into the plants from the air N_{α} arising from the deflation effect with the concentration $N_K = KA$, where K is an empirical coefficient for the accumulation of the nuclide by the plants from the soil. We use an expression from [5] for N_{α} to get

$$\frac{N_{\alpha}}{N_K} = \frac{R\nu_g\tau}{K} k_{\alpha}, \tag{9}$$

where R is the aerosol plant contamination coefficient, ν_g is the effective rate of turbulent aerosol deposition, and τ is the length of the growing period during which the radioactive dust deposits on the plants. Here we have used the relation $\alpha = k_{\alpha}\nu_{\alpha}$ between k_{α} and the parameters of the wind dust uptake from the surface α and ν_{α} , which we have used previously [1].

Figure 1a gives values of N_{α}/N_K calculated from (9) for natural hay fields in the middle belt of the USSR with the typical values of $R=20 \text{ cm}^2/\text{g}$ for air-dry hay, $K=2 \times 10^{-2} \text{ cm}^2/\text{g}$ for air-dry hay, and $\tau=2$ months; we take $v_g = 2 \text{ cm}/\text{sec}$ for the central part of the contaminated zone [5]. This shows that aerosol contamination of grasses substantially influences the entry of the radionuclides into the plants during the first few years after the formation of the contaminated zone. On the other hand (Fig. 1a), if the unplowed area after the formation of the contaminated zone is $< 5-10\%$, one can virtually neglect the aerosol contamination of the plants within a year. The radiation dose received from radionuclides entering the body via food chains is proportional to the concentrations of them in the initial product, which in the present case is the grass, so the ratio N_{α}/N_K is equal to the ratio of the internal-irradiation dose due to aerosol contamination of the plants to the irradiation dose due to root contamination D_N/D_K .

If there is a single discharge to the atmosphere, the dose from internal irradiation (from inhalation) is proportional to the time integral of the radionuclide concentration in the air:

$$D_q = B_D \int_0^t q(\theta) d\theta = B_D q', \quad (10)$$

where B_D is a dose-conversion factor. The contamination density in the locality is also proportional to this integral $A = v_g q'$. We use the value $q' = A/v_g$ to get readily from (10), (4), and (1) an expression for comparing the doses from internal (inhalation) irradiation D_{α} due to radionuclide deflation in the contaminated zone and D_q from the primary radioactive cloud:

$$\frac{D_{\alpha}}{D_q} = \frac{2v_g C \sqrt{\lambda}}{\rho v \Gamma(1+\nu) v_D \sqrt{v_D}} \int_0^l \sqrt{x^{\nu}} k_m(y, z) dx, \quad (11)$$

where

$$y = t \sqrt{\frac{v_D \lambda}{x}}, \quad z = 2 \sqrt{\frac{x \lambda}{v_D}},$$

$$k_m(y, z) = \frac{1}{2} \int_0^y \xi^{m-1} e^{-\frac{z}{2}(\xi+1)} d\xi$$

in which $k_m(y, z)$ is an incomplete MacDonal function and $m = -\nu$.

We now consider the consequences of steady-state entry of radioactive substances into the atmosphere, for example by discharges from a nuclear power station. In the neighborhood of the discharge source, a constant radionuclide concentration q is maintained in the air, while the contamination density in the locality increases linearly with time in accordance with $A = v_g q t$. An expression for the radionuclide concentration in the soil $n(x, t)$ is used for a stationary influx from the atmosphere to the surface $P = v_g q$ [3] to get from (2) that

$$k_{\alpha} = \frac{C}{\rho v \Gamma(\nu) v_D^{1+\nu} t} \int_0^t \frac{e^{-\lambda \theta}}{\theta^{1+\nu}} \int_0^l x^{\nu} e^{-\frac{x}{v_D \theta}} d\theta dx. \quad (12)$$

On the basis of [2] it can be shown that in this case a mobile equilibrium is set up in the surface soil layer. The influx of a nuclide from the atmosphere is balanced by the efflux into the deeper layers of soil and by radioactive decay. As A in (2) increases with time, k_{α} will decrease monotonically with time. Figure 1b shows calculations on k_{α} from (12) and on $N_{\alpha}/N_K = D_N/D_K$ from (9) for typical values of ν and v_D . Comparison of parts a and b of Fig. 1 shows that when there is a stationary discharge, the deflation coefficient and the ratios N_{α}/N_K D_N/D_K vary within much narrower limits than after a single discharge.

It is of interest to compare N_{α} with the concentration N_q due to deposition or primary aerosol particles discharged to the atmosphere from a nuclear power station stack. It is readily shown that in stationary discharge

$$\frac{N_{\alpha}}{N_q} = \frac{D_{\alpha}}{D_q} = \frac{q_{\alpha}}{q} = \frac{C v_g}{\rho v \Gamma(\nu) v_D^{1+\nu} t} \int_0^t \frac{e^{-\lambda \theta}}{\theta^{1+\nu}} \int_0^l x^{\nu} e^{-\frac{x}{v_D \theta}} d\theta dx, \quad (13)$$

which coincides with (11), i.e., the ratio of the internal-irradiation dose due to deflation to the dose due to inspiration of primary radioactive particles is the same for two cases: a single discharge and a stationary source.

Figure 2 shows that the deflation effects do not make a substantial contribution to the internal (inhalation) irradiation dose in the stationary case or in a single discharge. The contamination of the plants through the air near a nuclear power station also occurs mainly from the primary aerosol, not from deflation effects. The

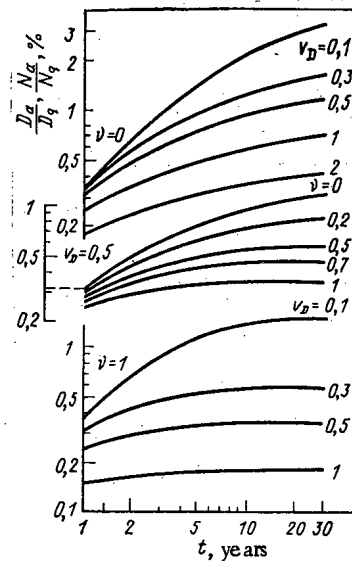


Fig. 2. Variation over time in the ratios of the inhalation dose due to ^{90}Sr (D_{α}/D_q) due to deflation and primary aerosol contamination for single and stationary discharges and also the aerial contamination of the grass (N_{α}/N_q) due to these effects for stationary discharge.

numerical values of N_{α}/N_K and N_{α}/N_q in Fig. 1b and 2 show that the proportion of aerosol entry of radionuclides into plants near a nuclear power station is decisive for all periods of station operation by comparison with the overall contamination N_q/N arising from the roots and parts outside them. We give below values of N_q/N for the most typical values $v_D = 0.5$ cm/year and $\nu = 0.5$:

t, years	1	3	5	10	20	30
$N_q/N, \%$	99.4	98.2	97.1	94.3	89.3	85.1

Results obtained here for ^{90}Sr apply also to ^{137}Cs , which has a similar value of λ ; ^{90}Sr differs from ^{137}Cs in being more readily soluble and therefore having a higher rate of infiltration into the soil with precipitation, so with approximately identical v_D the value of ν for ^{90}Sr is larger than that for ^{137}Cs by a factor of 2-3.

Therefore, effects due to the wind raising radionuclides from the soil may play an important part in accidental discharges because radioactive substances may be incorporated into food chains, while in the region of a normally working nuclear power station the main part is played by the entry of radionuclides into the plants directly from the gas-aerosol plume. The radiation dose due to radionuclide inhalation is virtually independent of the deflation effect. All these conclusions have been drawn on the assumption that the speed of vertical radionuclide migration in the soil does not vary in time. If on the other hand chemical processes cause the nuclides to be fixed in the surface layer of soil, the reduction in k_{α} over time indicated by Fig. 1a and b may be slowed down considerably, while the saturation level to which the curves tend in Fig. 2 will increase substantially.

LITERATURE CITED

1. K. P. Makhon'ko, *Izv. Akad. Nauk SSSR, Ser. Fiz. Atmos. Okeana*, No. 5, 568 (1979).
2. K. P. Makhon'ko, *Meteorol. Gidrologiya*, No. 9, 48 (1980).
3. K. P. Makhon'ko, in: *Radioactive Isotopes in Soils and Plants* [in Russian], Kolos, Leningrad (1969), p. 48.
4. L. Anspaugh et al., *Health Phys.*, 25, No. 4, 571 (1975).
5. K. P. Makhon'ko, *Ekologiya*, No. 2, 46 (1981).

USE OF PROTON AND DEUTERON ACTIVATION
METHODS OF ANALYSIS IN THE DETERMINATION
OF ELEMENTS WITH $Z > 42$

S. Mukhammedov, A. Vasidov,
and É. Pardaev

UDC 543.53

In recent years there has been intensive research on the physical principles and the analytic parameters of methods of activation analysis using charged particles (AAP) [1, 2]. The yield of radioactive nuclide is the main physical quantity determining the sensitivity of AAP and depends on the cross section of the analytic reaction, the energy, and the current of bombarding particles [2, 3]. Among the methods of AAP, those based on proton activation analysis (PAA) and deuteron activation analysis (DAA) are of special interest, since they can be used for determining the concentrations of a considerable number of elements at levels of 10^{-5} - 10^{-8} % [1, 4].

Today the possibilities of determining the concentrations of elements with $Z \leq 42$ by these two methods have been studied [4-7]. In the determination of elements with $Z > 42$ researchers have also achieved high sensitivities. However, up to now there has not been a sufficiently thorough investigation of the analytic parameter of the determination of these elements by the PAA and DAA methods. At the present time, investigators have measured the yields of radionuclides formed in the activation of elements with $Z > 42$ at $E_p = 10$ MeV [8] and of Pd, Ta, and W at $E_p = 12$ MeV [9], and Zatulokin et al. [4] give such data for six elements in the 8-11 MeV proton energy range. There have also been measurements of the yields of radionuclides formed in the activation of Rh, Eu, W, and Sb by deuterons [10-13]. The lack of the necessary data on the yields of radionuclides for elements with $Z > 42$ at different particle energies makes it difficult to use PAA and DAA in practice, to estimate the effect of the matrix and of possible interference on the analysis and the degree of radiochemical purification required.

In the present study we measure the yields of radionuclides with a half-life $T_{1/2} > 20$ min at an accelerate proton and deuteron energy ≤ 12 MeV and, making use of these results, we estimate the analytic possibilities of DAA and PAA in determining the concentration of elements with $Z > 42$.

Technique of the Experiment. In the experiments we used the 150-cm cyclotron of the Nuclear Physics Institute of the Academy of Sciences of the Uzbek SSR. The initial values of the proton and deuteron energy were 18 and 16 MeV, respectively. We used decelerating foils to reduce the particle energy to 7-12 MeV. The dispersion of the particle energies was about 2%. The methods used for the irradiation, the measurement of the induced radioactivity of the specimens, and the formulas for calculating the yields were similar to those described earlier [6]. The particle current was measured by means of an integrator with an error < 5 %. For the thick targets we used pressed tablets made from chemical compounds of the investigated elements, of an analytically pure brand [6]. The specimens were irradiated for 5-20 min, and the particle current was 0.05-0.1 μ A. The radioactivity was determined 3-5 min after the targets had been "cooled" for $(0.2-2) \cdot T_{1/2}$. The statistical errors of the measurement of the induced activity were no more than about 10%, and the absolute errors of the radionuclide yield measurements about 15%. For I, Ru, Pd, Au, and Th, because of the lack of suitable compounds of these elements and the difficulty of making the targets, the radionuclide yields were found by the method of numerical integration of the excitation functions of the reactions [14-17].

Evaluation of the Results. In Table 1 we show the yields of radionuclides from thick targets with $Z > 42$. The radionuclide yields of $E_p = 12$ MeV have values of $(2.7-7.8) \cdot 10^8$ Bq/ μ A \cdot h for ^{110}In , ^{128}I , ^{141}Nd , ^{107}Cd ; $(0.2-7) \cdot 10^7$ Bq/ μ A \cdot h for ^{110m}In , ^{111}In , ^{117}Sb , ^{121}Te , ^{130}I , ^{127}Xe , ^{133m}Ba , ^{142}Pr , ^{182}Re . For La, Au, Pb, and Th the yields are low and amount to $(0.4-4.8) \cdot 10^5$ Bq/ μ A \cdot h. When the targets were irradiated with deuterons ($E_d = 12$ MeV), the radionuclides had high yields: $(1-4.3) \cdot 10^7$ Bq/ μ A \cdot h for ^{105}Ru , ^{117}Sb , ^{130}I , ^{188}Re , ^{134m}Cs ; $(0.2-7) \cdot 10^6$ Bq/ μ A \cdot h for ^{87}Ru , ^{103}Pd , ^{111m}Pd , ^{115}Cd , ^{118m}Sb , ^{131}I , ^{127}Xe , ^{142}Pr , ^{151}Gd , ^{186}Re , ^{188}Au and $(2.9-9.7) \cdot 10^4$ Bq/ μ A \cdot h for ^{113}Sn , ^{160}Tb . As can be seen, there were no substantial differences between the yields of radionuclides when the elements were activated with protons and deuterons. In the case of PAA and DAA a high sensitivity S was attained for Cd, In, Sn, Ag, Pr, Sb, Ru, Te, Cs, Pb, and others. For these elements, at optimal analysis conditions, the

Translated from Atomnaya Énergiya, Vol. 56, No. 1, pp. 50-53, January, 1984. Original article submitted February 25, 1983.

TABLE 1. Yields of Radionuclides ($Y, \times 10^4$ Bq/ μ A·h) of Thick Specimens and Sensitivity of the Analysis of $E=10$ MeV, $I=10 \mu$ A, $t_{irr}=1$ h

Nuclear reaction	Particle energy, MeV						n	S, Bq/ μ g·s ⁻¹	
	7	8	9	10	11	12			
⁹⁶ Ru (d, p) ⁹⁷ Ru	0.7	2.0	3.5	5.0	7.0	9.6	5	5.0	
¹⁰² Ru (d, p) ¹⁰³ Ru	0.4	0.8	1.2	1.9	2.3	2.6	5	1.9	
¹⁰⁴ Ru (d, p) ¹⁰⁵ Ru	0.5	0.9	1.3	1.7	2.2	2.7	7	1.70	
¹⁰³ Rh (p, n) ¹⁰³ Pd	1.0	1.7	2.8	5.3	8.4	10.6	6	5.3	
¹⁰³ Rh (d, 2n) ¹⁰² Pd	0.3	0.9	2.0	3.2	4.5	7.0	6	3.2	
¹⁰⁹ Pd (d, p) ¹¹⁰ Pd	0.3	0.7	1.7	2.1	3.7	4.4	7	2.1	
¹⁰⁷ Ag (p, n) ¹⁰⁷ Cd	1.3	3.1	5.6	9.4	15.2	21.5	7	94.0	
¹¹⁰ Cd (p, n) ^{110m} In	0.2	1.3	3.8	7.2	11.0	15.4	8	72	
¹¹⁰ Cd (p, n) ¹¹⁰ In	0.2	0.5	1.0	1.6	2.7	4.2	8	1600	
¹¹¹ Cd (p, n) ^{111m} In		0.8	1.8	3.1	4.2	6.0	8	31	
¹¹³ Cd (p, n) ^{113m} In	0.7	1.0	1.5	2.1	2.9	3.6	7	210	
¹¹⁶ Cd (p, n) ^{116m} In	0.4	1.0	1.9	3.2	4.5	5.6	7	320	
¹¹⁴ Cd (d, n) ^{115m} Cd	0.6	1.1	2.0	3.0	4.0	5.0	5	3.0	
¹¹⁴ Cd (d, p) ¹¹⁵ Cd	0.5	0.8	1.6	2.1	3.2	3.8	6	21	
¹¹³ In (d, 2n) ¹¹³ Sn		0.1	0.5	0.8	2.4	2.9	4	0.08	
¹¹⁷ Sn (p, n) ¹¹⁷ Sb	0.4	1.1	1.9	3.1	4.8	7.0	7	310	
¹²⁰ Sn (p, n) ^{120m} Sb	0.2	0.6	1.0	1.4	2.0	2.6	6	14	
¹²² Sn (p, n) ¹²² Sb	0.2	0.5	0.8	1.1	1.6	2.1	6	11	
¹¹⁷ Sn (d, 2n) ¹¹⁷ Sb	1.0	2.2	6.2	9.5	13.5	17.5	6	95	
¹¹⁸ Sn (d, 2n) ^{118m} Sb	0.5	0.7	4.0	16	28	40	5	16	
¹²⁰ Sn (d, 2n) ^{120m} Sb	0.7	1.5	33	55	75	85	3	0.6	
¹²² Sn (d, 2n) ¹²² Sb	0.2	0.9	3.8	5.0	5.9	6.7	5	5.0	
¹²¹ Sb (p, n) ^{121m} Te	0.4	1.1	2.4	4.2	7.5	10.5	4	0.4	
¹²¹ Sb (p, n) ¹²¹ Te	6.4	1.2	3.0	5.9	10	15.0	5	5.9	
¹²³ Sb (p, n) ^{123m} Te	0.5	1.5	2.8	4.4	7.4	10.5	6	0.4	
¹²⁸ Te (p, n) ¹²⁸ I	0.2	0.4	0.9	1.2	1.8	2.4	8	1200	
¹³⁰ Te (p, n) ¹³⁰ I	0.4	0.6	0.8	1.1	1.4	1.8	7	110	
¹²⁶ Te (d, 2n) ¹²⁶ I	0.05	0.3	0.6	1.0	2.4	3.2	5	1.0	
¹³⁰ Te (d, 2n) ¹³⁰ I	0.05	0.6	1.0	1.5	2.9	4.3	7	150	
¹³⁰ Te (d, n) ¹³¹ I	0.3	0.6	1.1	1.9	2.8	3.2	5	1.9	
¹²⁷ I (p, n) ¹²⁷ Xe	0.8	2.3	4.9	8.9	13.4	19.1	5	8.9	
¹²⁷ I (d, 2n) ¹²⁷ Xe	0.5	1.4	2.8	3.4	7.7	10	5	3.4	
¹³³ Cs (p, n) ^{133m} Ba	0.7	1.6	3.1	5.3	10	15.7	6	5.3	
¹³³ Cs (d, p) ^{134m} Cs	0.8	1.4	1.9	2.9	3.5	4.6	7	290	
¹³³ Cs (d, p) ¹³⁴ Cs	0.4	0.8	1.2	1.6	1.9	2.5	4	0.16	
¹³³ Cs (d, 2n) ^{133m} Ba	1.5	2.2	3.7	7.4	10.2	15.7	6	74	
¹³⁹ La (p, n) ¹³⁹ Ce		0.15	0.45	1.0	1.7	2.5	5	1.0	
¹⁴² Ce (p, n) ¹⁴² Pr	0.2	0.5	1.0	1.5	1.7	1.9	6	15	
¹⁴² Ce (d, 2n) ¹⁴² Pr	0.2	0.4	1.5	3.8	5.1	8.0	6	38	
¹⁴¹ Pr (p, n) ¹⁴¹ Nd				0.4	2.4	4.7	7.0	8	2400
¹⁵¹ Eu (p, n) ¹⁵¹ Gd			2.5	5.4	8.3	12.5	4	0.5	
¹⁵³ Eu (p, n) ¹⁵³ Gd		0.8	1.4	2.2	3.9	4.3	4	0.2	
¹⁵³ Eu (d, 2n) ¹⁵³ Gd	0.5	0.8	1.4	2.1	3.9	5.2	4	0.2	
¹⁵³ Eu (d, 2n) ¹⁵³ Gd	0.2	0.7	1.1	1.6	2.9	4.0	4	0.16	
¹⁵⁸ Th (d, p) ¹⁶⁰ Th	0.4	0.8	3.5	5.5	7.0	9.7	4	0.6	
¹⁵⁹ Th (d, 2n) ¹⁵⁹ Dy		0.4	1.8	4.0	6.0	14	4	0.4	
¹⁸¹ Ta (p, n) ¹⁸¹ W		0.7	2.0	3.8	5.7	8.4	4	0.4	
¹⁸¹ Ta (d, p) ¹⁸² Ta	0.2	0.4	7.6	12	16	20	4	1.2	
¹⁸¹ Ta (d, 2n) ¹⁸¹ W	0.9	4.0	5.0	15	23	35	4	1.5	
¹⁸⁶ W (d, 2n) ¹⁸⁶ Re		0.5	2.2	0.8	12	22	5	8.0	
¹⁸⁷ Re (d, p) ¹⁸⁸ Re	0.6	1.0	3.0	4.6	8.0	11	6	46	
¹⁹⁷ Au (p, n) ¹⁹⁷ Hg			0.1	0.6	1.4	4.1	4	0.06	
¹⁹⁷ Au (d, p) ¹⁹⁸ Au	0.3	0.8	3.0	12	27	36	5	12	
²⁰⁴ Pb (p, n) ²⁰⁴ Bi		0.6	2.2	5.8	11.9	20.8	4	0.6	
²⁰⁶ Pb (p, n) ²⁰⁶ Bi	0.1	0.3	0.7	1.5	2.9	4.8	5	1.5	
²³² Th (p, n) ²³² Pa				1.0	1.6	2.4	5	1.0	

detection limits reach values of 1-0.01 μ g/g. Using the data obtained, we can estimate the level of interference due to the matrices and ascertain the specimens for which instrumental variants of the analysis are possible. The most suitable for the analysis may be matrices whose irradiation with a beam of protons and deuterons ($E < 12$ MeV) forms either very short-lived or very long-lived radionuclides emitting γ quanta which do not interfere with the determination of the elements, with a yield less than 10^4 Bq/ μ A·h.

In practice it is often necessary to have an idea of the advantages and disadvantages of activation-analysis methods. In Table 2 we show the radionuclide yields obtained in reactions with protons and deuterons, fast and thermal neutrons, and high-energy γ quanta [18, 19]. As can be seen, the radionuclide yields in the case of activation of elements with $Z > 42$ by charged particles are 10^2 - 10^6 times as large as those obtained in the activation of elements by fast neutrons and high-energy γ quanta. Only a few elements fail to conform to this rule. The activation of practically all elements by thermal neutrons yields radionuclides in quantities two to four orders of magnitude larger than the radionuclide yields produced in charged-particle reactions.

From the results obtained it follows that the PAA and DAA methods provide about the same sensitivity of analysis in the determination of elements with $Z > 42$. They have a number of advantages over other methods. For example, in the analysis of matrices containing elements with $Z > 75$, the radionuclide yields are small (10^4 Bq/ μ A·h) and the interference level is not high. Moreover, in the determination of the amount of a considerable number of elements (Pb, Ag, Te, Ce, etc.) contained in the specimen, PAA and DAA provide sensitivity values higher than can be attained with neutron-activation analysis at low concentrations because the latter has unfavorable nuclear-physics analytic characteristics.

TABLE 2. Comparison of the Yields of Radionuclides Formed in the Activation of Elements with Various Nuclear Particles

Activation by protons*		Activation by deuterons*		Activation by fast neutrons†		Activation by thermal neutrons‡		Activation by γ -quanta**	
radionuclide	Y, MBq/g	radionuclide	Y, MBq/g	radionuclide	Y, MBq/g	radionuclide	Y, MBq/g	radionuclide	Y, MBq/g
$^{103}\text{Rh} \rightarrow ^{103}\text{Pd}$	$2 \cdot 10^2$	$^{103}\text{Ru} \rightarrow ^{103}\text{Ru}$	10^3	$^{99}\text{Ru} \rightarrow ^{99}\text{Ru}$	$7 \cdot 10^{-3}$	$^{103}\text{Ru} \rightarrow ^{103}\text{Ru}$	20	$^{104}\text{Ru} \rightarrow ^{103}\text{Ru}$	0,7
		$^{103}\text{Rh} \rightarrow ^{103}\text{Pd}$	$2,3 \cdot 10^3$	$^{103}\text{Rh} \rightarrow ^{103}\text{Rh}$	$4 \cdot 10^{-4}$	$^{103}\text{Rh} \rightarrow ^{104}\text{Rh}$	$7 \cdot 10^5$	$^{103}\text{Rh} \rightarrow ^{103}\text{Rh}$	0,6
		$^{110}\text{Pd} \rightarrow ^{110}\text{Pd}$	20	$^{105}\text{Pd} \rightarrow ^{105}\text{Rh}$	$9 \cdot 10^{-4}$	$^{105}\text{Pd} \rightarrow ^{105}\text{Pd}$	10^4	$^{105}\text{Pd} \rightarrow ^{105}\text{Pd}$	1,0
$^{110}\text{Cd} \rightarrow ^{110}\text{In}$	$8,4 \cdot 10^3$	$^{114}\text{Cd} \rightarrow ^{114}\text{Cd}$	$1,5 \cdot 10^3$	$^{112}\text{Cd} \rightarrow ^{111}\text{mCd}$	$4 \cdot 10^{-1}$	$^{110}\text{Cd} \rightarrow ^{111}\text{mCd}$	$5 \cdot 10^3$	$^{118}\text{Cd} \rightarrow ^{118}\text{Ag}$	1,0
		$^{113}\text{In} \rightarrow ^{113}\text{Sn}$	1,1	$^{115}\text{In} \rightarrow ^{115}\text{Cd}$	10^{-3}	$^{110}\text{In} \rightarrow ^{116}\text{mIn}$	$6 \cdot 10^5$	$^{115}\text{In} \rightarrow ^{116}\text{mIn}$	40
$^{117}\text{Sn} \rightarrow ^{117}\text{Sb}$	$1,6 \cdot 10^3$	$^{117}\text{Sn} \rightarrow ^{117}\text{Sb}$	$6,3 \cdot 10^2$	$^{116}\text{Sn} \rightarrow ^{116}\text{mIn}$	$5 \cdot 10^{-3}$	$^{112}\text{Sn} \rightarrow ^{112}\text{Sn}$	$2 \cdot 10^{-1}$	$^{124}\text{Sn} \rightarrow ^{123}\text{Sn}$	0,1
$^{121}\text{Sb} \rightarrow ^{121}\text{Te}$	30			$^{123}\text{Sb} \rightarrow ^{123}\text{mSb}$	$4 \cdot 10^{-3}$	$^{121}\text{Sb} \rightarrow ^{122}\text{Sb}$	$2 \cdot 10^3$	$^{121}\text{Sb} \rightarrow ^{120}\text{mSb}$	10
$^{126}\text{Te} \rightarrow ^{126}\text{I}$	$8 \cdot 10^3$	$^{130}\text{Te} \rightarrow ^{130}\text{I}$	$1,3 \cdot 10^3$	$^{126}\text{Te} \rightarrow ^{126}\text{Te}$	$2 \cdot 10^{-1}$	$^{130}\text{Te} \rightarrow ^{131}\text{mTe}$	14		
$^{127}\text{I} \rightarrow ^{127}\text{Xe}$	60	$^{127}\text{I} \rightarrow ^{127}\text{Xe}$	35	$^{127}\text{I} \rightarrow ^{126}\text{I}$	10^{-2}	$^{127}\text{I} \rightarrow ^{126}\text{I}$	10^5	$^{127}\text{I} \rightarrow ^{126}\text{I}$	20
$^{133}\text{Cs} \rightarrow ^{133}\text{mBa}$	$3 \cdot 10^2$	$^{133}\text{Cs} \rightarrow ^{134}\text{Cs}$	$1,6 \cdot 10^3$	$^{133}\text{Cs} \rightarrow ^{134}\text{Cs}$	$3 \cdot 10^{-2}$	$^{133}\text{Cs} \rightarrow ^{134}\text{Cs}$	4,5	$^{133}\text{Cs} \rightarrow ^{132}\text{Cs}$	30
$^{139}\text{La} \rightarrow ^{139}\text{Ce}$	6			$^{139}\text{La} \rightarrow ^{139}\text{Ba}$	10^{-2}	$^{139}\text{La} \rightarrow ^{140}\text{La}$	$7 \cdot 10^3$		
$^{142}\text{Ce} \rightarrow ^{142}\text{Pr}$	50	$^{142}\text{Ce} \rightarrow ^{142}\text{Pr}$	$2 \cdot 10^2$	$^{140}\text{Ce} \rightarrow ^{139}\text{mCe}$	3,6	$^{142}\text{Ce} \rightarrow ^{143}\text{Ce}$	90	$^{140}\text{Ce} \rightarrow ^{139}\text{Ce}$	1,0
$^{141}\text{Pr} \rightarrow ^{141}\text{Nd}$	$1,3 \cdot 10^4$			$^{141}\text{Pr} \rightarrow ^{141}\text{Ce}$	$4 \cdot 10^{-5}$	$^{141}\text{Pr} \rightarrow ^{142}\text{Pr}$	$1,5 \cdot 10^4$	$^{141}\text{Pr} \rightarrow ^{140}\text{Ce}$	$2 \cdot 10^3$
$^{151}\text{Eu} \rightarrow ^{151}\text{Gd}$	2,0	$^{152}\text{Eu} \rightarrow ^{152}\text{Gd}$	1,0	$^{151}\text{Eu} \rightarrow ^{150}\text{mEu}$	$5 \cdot 10^{-2}$	$^{151}\text{Eu} \rightarrow ^{152}\text{mEu}$	$2 \cdot 10^5$		
		$^{156}\text{Tb} \rightarrow ^{156}\text{Dy}$	2,4	$^{156}\text{Tb} \rightarrow ^{156}\text{Gd}$	$2 \cdot 10^{-3}$	$^{156}\text{Tb} \rightarrow ^{160}\text{Tb}$	$3 \cdot 10^3$	$^{156}\text{Tb} \rightarrow ^{155}\text{Tb}$	$4 \cdot 10^{-3}$
$^{181}\text{Ta} \rightarrow ^{181}\text{W}$	1,5	$^{181}\text{Ta} \rightarrow ^{182}\text{Ta}$	6,0	$^{181}\text{Ta} \rightarrow ^{180}\text{mTa}$	$3 \cdot 10^{-1}$	$^{181}\text{Ta} \rightarrow ^{182}\text{Ta}$	$1,6 \cdot 10^2$	$^{181}\text{Ta} \rightarrow ^{180}\text{mTa}$	$8 \cdot 10^3$
$^{182}\text{W} \rightarrow ^{182}\text{mRe}$	$2 \cdot 10^2$	$^{186}\text{W} \rightarrow ^{186}\text{Re}$	50	$^{184}\text{W} \rightarrow ^{184}\text{Ta}$	10^{-3}	$^{186}\text{W} \rightarrow ^{187}\text{W}$	$9 \cdot 10^3$	$^{186}\text{W} \rightarrow ^{185}\text{W}$	1,0
		$^{187}\text{Re} \rightarrow ^{188}\text{Re}$	$3 \cdot 10^3$	$^{187}\text{Re} \rightarrow ^{187}\text{W}$	$2 \cdot 10^{-4}$	$^{187}\text{Re} \rightarrow ^{188}\text{Re}$	$6 \cdot 10^4$	$^{187}\text{Re} \rightarrow ^{186}\text{Re}$	50
$^{197}\text{Au} \rightarrow ^{197}\text{Hg}$	0,4	$^{197}\text{Au} \rightarrow ^{198}\text{Au}$	10^2	$^{197}\text{Au} \rightarrow ^{197}\text{mAu}$	$8 \cdot 10^{-1}$	$^{197}\text{Au} \rightarrow ^{198}\text{Au}$	$3 \cdot 10^4$	$^{197}\text{Au} \rightarrow ^{196}\text{Au}$	50
$^{206}\text{Pb} \rightarrow ^{206}\text{Bi}$	7,3			$^{204}\text{Pb} \rightarrow ^{203}\text{Pb}$	10^{-3}	$^{206}\text{Pb} \rightarrow ^{207}\text{mPb}$	$1,8 \cdot 10^2$	$^{206}\text{Pb} \rightarrow ^{205}\text{Pb}$	2,0

* Proton and deuteron current $10 \mu\text{A}/\text{cm}^2$, $E=11 \text{ MeV}$, $t_{\text{irr}}=1 \text{ h}$.† Flux density $\sim 10^9$ neutrons/ $\text{cm}^2 \cdot \text{sec}$, $E=14 \text{ MeV}$, $t_{\text{irr}}=1 \text{ h}$.‡ Flux density $\sim 10^{13}$ neutrons/ $\text{cm}^2 \cdot \text{sec}$, $t_{\text{irr}}=1 \text{ h}$.** Electron current $100 \mu\text{A}$, $E=25 \text{ MeV}$, $t_{\text{irr}}=4 \text{ h}$.

LITERATURE CITED

- V. A. Muminov and S. Mukhammedov, in: Use of Accelerators in Element Analysis [in Russian], Fan, Tashkent (1980), p. 4.
- B. V. Zatolokin, I. O. Konstantinov, and N. N. Krasnov, *ibid.*, p. 40.
- N. Krasnov, B. Zatolokin, and I. Konstantinov, *J. Radioanal. Chem.*, **39**, No. 1-2, 163 (1977).
- B. V. Zatolokin, I. O. Konstantinov, and N. N. Krasnov, *At. Energ.*, **42**, No. 4, 311 (1977).
- G. Vakilova et al., in: Radioactivation Methods of Analysis of Objects of Natural Origin [in Russian], Fan, Tashkent (1980), p. 108.
- G. Vakilov et al., *At. Energ.*, **55**, No. 3, 164 (1983).
- J. Debrun, J. Barrandon, and P. Benaben, *Anal. Chem.*, **48**, No. 1, 167 (1976).
- J. Barrandon, P. Benaben, and J. Debrun, *Anal. Chim. Acta*, **83**, No. 1, 157 (1976).
- K. Krivan and V. Krivan, *Fresenius Z. Anal. Chem.*, **295**, No. 4, 348 (1979).
- P. P. Dmitriev, M. V. Panarin, and G. A. Molin, *At. Energ.*, **53**, No. 3, 198 (1982).
- N. A. Kon'yakhin, I. O. Konstantinov, and P. P. Dmitriev, *ibid.*, **27**, No. 3, 208 (1969).
- P. P. Dmitriev and G. A. Molin, *ibid.*, **48**, No. 2, 122 (1980).
- P. P. Dmitriev et al., *ibid.*, **42**, No. 2, 148 (1977).
- J. Debrun, D. Riddle, and E. Schweikert, *Anal. Chem.*, **44**, No. 8, 1386 (1972).
- J. Natowitz et al., *Phys. Rev.*, **A155**, No. 4, 1352 (1967).
- A. Mito et al., *Nucl. Phys.*, **A129**, No. 1, 165 (1969).
- L. Hansen, *ibid.*, **30**, No. 3, 389 (1962).
- G. Lutz, *Anal. Chem.*, **41**, No. 3, 424 (1969).
- I. V. Medinis, Handbook Tables for Neutron Activation Analysis [in Russian], Zinatne, Riga (1974), p. 410.

LETTERS TO THE EDITOR

RESULTS OF MEASUREMENTS OF THE NEUTRON
FIELD IN THE CHANNELS OF THE VVER-1000

S. S. Lomakin, A. G. Morozov,
G. G. Panfilov, V. P. Kruglov,
and G. M. Bakhirev

UDC 621.039.51:539.125.52

The results of a calculation of the neutron field outside the bounds of the core of a nuclear power station reactor require a thorough experimental justification. As a rule, the values of the neutron flux density obtained at different points of the reactor serve as the starting data. Experiments carried out on the VVER-1000 of the fifth unit of the Novovoronezh nuclear power station by means of activation detectors, allow the fast and thermal neutron distribution to be determined outside the bounds of the high pressure vessel.

The measurements were conducted in vertical experimental channels (EC) and in the measurement channel (MC). The first channel, EC-1, made from a tube with a diameter of 36×3 mm, was installed flush with the inside surface of the concrete reactor shaft [1] at a distance of 293.5 cm from the axis of the reactor. The inside surface of the shaft was 291 cm distant from the axis of the reactor. The second channel, EC-2, was made from a tube with a diameter of 53×3 mm. The axis of this channel, and also of the MC channel, passes through at a distance of 310.5 cm from the axis of the reactor.

The fast neutron distribution was measured by means of threshold detectors containing ^{115}In . The values of the energy threshold and of the effective threshold cross section for the reaction $^{115}\text{In}(n, n')$ used were equal to 1.15 MeV and 286 mb respectively ($1 \text{ b} = 10^{-28} \text{ m}^2$). The activity of the indium detectors was measured on photon spectrometer.

The measurement results are shown in Fig. 1. The distribution 1 corresponds to the channel EC-1, and distribution 2 corresponds to EC-2. The "break" in distribution 1 for the upper part of the channel is due to the special structural feature of the latter. The upper end of this channel rests in the annular supporting girder of the reactor but does not reach to the top of the core by approximately 1 m. The structural design of EC-2 allowed the fast neutron distribution to be measured on a length greater than in the EC-1 channel, but still not over the entire height of the core. Nevertheless, from the general nature of the relations obtained, the factors affecting the formation of the fast neutron field outside the reactor vessel can be judged.

The neutron distribution at the inside surface of the concrete shield within the limits of 1-2.5 m of the height of the core almost repeats the energy distribution, averaged over the core (Fig. 1, curve 3). Below 1 m, the distribution in EC-1 slopes more mildly, which is due to neutrons shooting downwards through the gap between the reactor vessel and shaft. In distribution 2 there is a clearly expressed maximum, which is due to fast neutrons shooting along the horizontal gap (Fig. 1, position 4) between the supporting girder and the serpentine concrete (width of gap 3-5 cm). The sharp decrease of fast neutrons in the upper part of channel EC-2 is related with the intense absorption of neutrons by the supporting girder. The fast neutron flux density in channel EC-1 at the level of the center of the reactor core amounted to $4.7 \cdot 10^8$ neutrons/($\text{cm}^2 \cdot \text{sec}$), and in EC-2 it was $0.92 \cdot 10^8$ neutrons/($\text{cm}^2 \cdot \text{sec}$) with the reactor operating at nominal thermal power. The measurement error of the neutron flux density values was $\pm 20\%$ for a confidence coefficient of 95%.

The distribution of thermal neutrons over the height of channels EC-1 and EC-2 was measured by means of detectors containing the ^{63}Cu nuclide (Fig. 2). It follows from Fig. 2 that in channel EC-1 the thermal neutron distribution repeats the fast neutron distribution. The presence of a "steep drop" in the distribution for the upper part of the channel is due to the effect of the boron incorporated in the composition of the materials filling the supporting girder. The saddle at the maximum of the thermal neutron distribution for channel EC-2 is explained by the presence of the metal structure in the horizontal gap surrounding the channel. The nature of the thermal neutron distribution in the MC channel and in channel EC-2 is identical.

Detectors containing ^{176}Lu , ^{197}Au , ^{63}Cu , and ^{55}Mn were used for measuring the spectral parameters of the thermal neutron field. The detectors were calibrated beforehand in the standard neutron field of the F-1 reactor [2]. The activity of the thermal neutron detectors was measured on a standard counting facility.

Translated from *Atomnaya Énergiya*, Vol. 56, No. 1, pp. 54-55, January, 1984. Original article submitted January 6, 1983.

TABLE 1. Spectral Parameters of the Thermal Neutron Field in the Experimental Channels and in the Measurement Channel

Channel neutrons	$r\sqrt{T/T_0}$	$T, ^\circ\text{K}$	$\varphi_T 10^9$ neutrons/($\text{cm}^2 \cdot \text{sec}$)
EC -1	$0,090 \pm 0,004$	393 ± 16	$3,20 \pm 0,15$
EC -2	$0,050 \pm 0,002$	378 ± 15	$0,94 \pm 0,05$
MG	$0,16 \pm 0,01$	433 ± 17	$1,01 \pm 0,05$

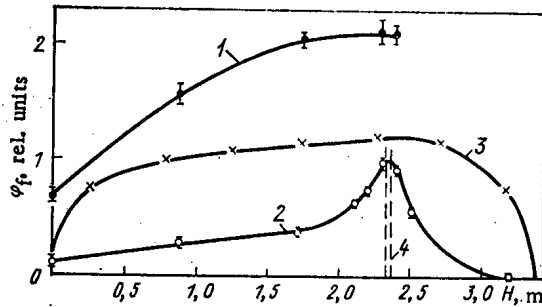


Fig. 1

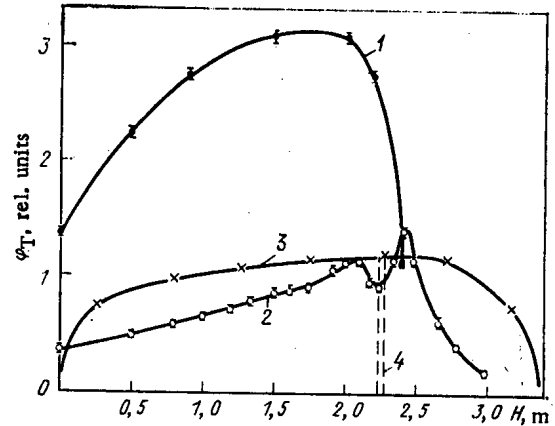


Fig. 2

Fig. 1. Axial distribution of the fast neutron flux density in the experimental channels (φ_f is the flux density of neutrons with energy $E > 1.15$ MeV; H is the distance from the lower boundary of the core): 1, 2) distribution $\varphi(H)$ in EC-1 and EC-2; 3) power distribution over the height of the core, averaged over the sections of location of the rhodium DPA, rel. units; 4) horizontal gap between concrete shield and the annular supporting girder.

Fig. 2. Axial distribution of the thermal neutron flux density φ_T in the experimental channels (legend the same as to Fig. 1).

The values of the thermal neutron flux density φ_T , corresponding to the temperature T of the Maxwell neutron distribution and the epithermal parameter $r\sqrt{T/T_0}$ [3] ($T_0 = 293^\circ\text{K}$) are shown in Table 1.

Analysis of the data shows that the spectrum of the thermal neutrons in channel EC-1 is harder than in EC-2. The spectrum of the neutrons in the MC channel differs in even greater hardness, which is explained by the large amount of metal in the tubes forming the channel. A comparison of the nature of the distribution φ_T in channels EC-1 and EC-2 confirms that the ratio of the neutron flux density for different height marks of the concrete shield is different. It should be borne in mind that the ratio of the fast and thermal flux densities in these channels can vary with change of the energy distribution in the core, due to the position of the control rods the fuel burnup or the xenon poisoning. This is a consequence of the effect of the structural characteristics of the circum-vessel compartment of the reactor, which have a marked effect on the formation of the neutron in channels MC and EC-2.

LITERATURE CITED

1. Yu. V. Vikhorev et al., *At. Energ.*, **50**, No. 2, 87 (1981).
2. É. F. Garapov et al., *At. Energ.*, **42**, No. 4, 286 (1977).
3. C. Westcott, *Effective Cross Section Values for Well-Moderated Thermal Reactor Spectra*, Chalk River, Canada, CRRP-960 (1960).

AMPLITUDE CHARACTERISTIC OF PYROELECTRIC DETECTORS

V. A. Borisyonok and E. Z. Novitskii

UDC 539.1.074:537.226/227

Analytic formulas for the amplitude characteristic of pyroelectric detectors have been obtained in [1-4]. When the sensitive element of the detector is a planar capacitor filled with a pyroelectric substance, the formulas are

$$i(t) = \frac{p}{c_V} \kappa \varphi(t); \quad (1)$$

$$q = \frac{p}{c_V} \kappa F; \quad (2)$$

$$q = \frac{p}{c_V} D, \quad (3)$$

where i denotes the density of the output current; q , density of the electric charge; p , pyroelectric coefficient; c_V , specific heat; κ , density of the absorbed energy per particle; and φ , F , and D , density of the current, the radiation flux, and the absorbed radiation dose, respectively.

The ratio p/c_V is termed the Coulomb-rad sensitivity of the detector. The amplitude characteristic in the form of Eq. (3) is quite universally valid because a source of some radiation (including composite radiations) can be employed for the experimental determination of the formula. The transition to characteristics in the form of Eqs. (1) and (2) is made with the coefficient κ ,

It is generally accepted [1-3] that the sensitive elements of pyrodetectors are prepared basically from materials belonging to the class of Seignette electrics which are characterized by better pyroelectric characteristics than the linear pyroelectric materials. The maximum flux values or the maximum absorbed radiation dose which can be recorded with such a detector are limited by the temperature of the phase transition of the Seignette electric (Curie point T_C) because when the material is heated above this temperature, the material loses its pyroelectric properties. Equations (1)-(3) show that the linear part of the amplitude characteristic is given by the condition $p/c_V = \text{const}$ in a certain temperature interval (or interval of absorbed dose). This condition is fulfilled at temperatures far from T_C . For example, the authors of [5] have made estimates and shown that the amplitude characteristic of a detector with a sensitive element of barium titanate is linear in the dose range $10^{-1}-2 \cdot 10^6$ rad (1 rad = 10 Gy). The authors of [1, 2] have experimentally shown that the amplitude characteristic of a lead zirconate-titanate ceramic detector of the 65/35 ZTP type is linear in the range $2-8 \cdot 10^3$ rad (ZTP 65/35). The experiment was made in a pulsed SPR reactor and with γ sources.

We studied in the experiment of our work the amplitude characteristic of a pyroelectric detector at absorbed doses of 10^3-10^6 rad. The experiment was made on a pulsed nuclear reactor with a radiation-pulse length $t_p \leq 10^{-4}$ sec. Detectors on the basis of the ZTP ceramic, type PKR-1 [6], and on the basis of single crystals of deuterated triglycine sulfate with an addition of 20% L- α alamine [7] were examined. The sensitive elements of PKR-1 and deuterated triglycine sulfate had a size of 20×2 and $10 \times 10 \times 2$ mm, respectively. Detectors with sensitive elements of unpolarized PKR-1 material or of two identical samples of PKR-1 and deuterated triglycine sulfate joined so that the pyroelectric effect was suppressed were used to determine the background.

We recorded in each experiment the detector output signal and calculated from it the charge flowing in the detector circuit while the radiation pulse acted. The parameters of the measuring circuit were chosen so that

Translated from *Atomnaya Énergiya*, Vol. 56, No. 1, pp. 55-56, January, 1984. Original article submitted February 16, 1983.

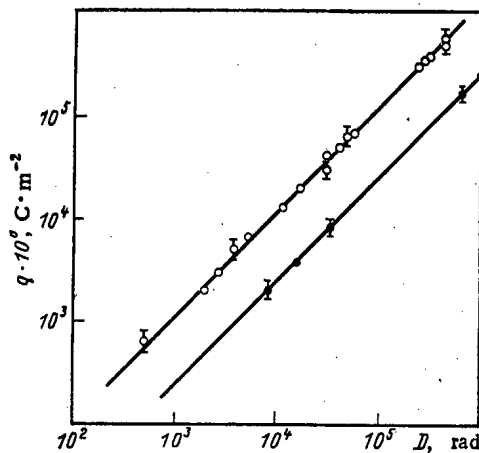


Fig. 1. Amplitude characteristic of the pyroelectric detectors with sensitive elements of (●) deuterated triglycine sulfate and (○) PKR-1.

the condition $\tau_e \ll t_p$ was satisfied, where τ_e denotes the electric constant of the detector. The radiation dose absorbed in the pyroelectric was determined with the formula

$$D = \kappa_\gamma F_\gamma + \kappa_n F_n, \quad (4)$$

where F_γ and F_n denote the flux of the γ radiation and of the neutrons at the location of the detector, respectively; the κ_γ and κ_n values calculated on a computer with the Monte Carlo method from the energy spectra of the reactor radiation were for PKR-1:

$$\kappa_\gamma = 0.73 \cdot 10^{-11} \frac{\text{J} \cdot \text{kg}^{-1}}{\text{quantum/cm}^2} \text{ and } \gamma_n = 0.13 \cdot 10^{-11} \frac{\text{J} \cdot \text{kg}^{-1}}{\text{neutron/cm}^2}; \text{ and for deuterated triglycine sulfate } \kappa_\gamma = 0.43 \cdot 10^{-11} \frac{\text{J} \cdot \text{kg}^{-1}}{\text{quantum/cm}^2} \text{ and } \kappa_n = 1.0 \cdot 10^{-11} \frac{\text{J} \cdot \text{kg}^{-1}}{\text{neutron/cm}^2}.$$

The experimental results depicted in Fig. 1 reveal that the amplitude characteristic of the pyroelectric detectors on the basis of PKR-1 and deuterated triglycine sulfate can be described by a linear function in the range 10^3 - 10^6 rad. The proportionality coefficient (Coulomb-rad sensitivity) is $(1.18 \pm 0.08) \cdot 10^{-8} \text{ C} \cdot \text{m}^{-2} \cdot \text{rad}^{-1}$ (in the case of PKR-1) and $(0.23 \pm 0.04) \cdot 10^{-8} \text{ C} \cdot \text{m}^{-2} \cdot \text{rad}^{-1}$ (in the case of the deuterated triglycine sulfate). It follows from the results of our work and the work of [1, 2] that the amplitude characteristic of pyrodetectors made from ceramic materials of the ZTP system with $T_C \geq 300^\circ\text{C}$ is linear in the range 1 - 10^6 rad (ZTP system). The relatively high T_C value of these materials allows the assumption that the linear range may extend to $5 \cdot 10^6$ rad (ZTP system). In the case of the deuterated triglycine sulfate, the value $D = 10^6$ rad (deuterated triglycine sulfate) reached in our work is close to the limit because in this case $T_C \approx 60^\circ\text{C}$. Additional investigations are required to establish the lower limit of the linearity region of these materials.

The results of our work allow us to evaluate at least two aspects in the operation of pyrodetectors. Thus, it has been mentioned in [3] that it is possible to calibrate pyroelectric detectors of ionizing radiation with optical wavelengths. The Coulomb-rad sensitivity was calculated through the dynamic pyrocoefficient measured with techniques in which an infrared radiation source was used for heating the sample; furthermore, the sensitivity was also calculated with the aid of the specific heat. The resulting values $p/c_V = (0.5-0.6) \cdot 10^{-8} \text{ C} \cdot \text{m}^{-2}/\text{rad}$ (PKR-1) ($p = 2.0 \cdot 10^{-4} \text{ C} \cdot \text{m}^{-2} \cdot \text{K}^{-1}$ [8], $c_V = (2.6-3.2) \cdot 10^6 \text{ J} \cdot \text{m}^{-3} \cdot \text{K}^{-1}$ [9])* and $p/c_V = (0.07-0.1) \cdot 10^{-8} \text{ C} \cdot \text{m}^{-2}/\text{rad}$ (deuterated triglycine sulfate) ($p = (0.95-1.82) \cdot 10^{-4} \text{ C} \cdot \text{m}^{-2} \cdot \text{K}^{-1}$ [7]; $c_V = 2.5 \cdot 10^6 \text{ J} \cdot \text{m}^{-3} \cdot \text{K}^{-1}$ [9, 10])* do not describe the results of our work. The p/c_V measurements made with the method of [11], where a pulse of ionizing radiation was used to heat the sample, rendered values $(1.10 \pm 0.32) \cdot 10^{-8} \text{ C} \cdot \text{m}^{-2}/\text{rad}$ (PKR-1) and $(0.24 \pm 0.08) \cdot 10^{-8} \text{ C} \cdot \text{m}^{-2}/\text{rad}$ (deuterated triglycine sulfate), which are in good agreement with the data listed above. The deviation from the calculated Coulomb-rad sensitivity obviously has the same reason as the deviation of the static and dynamic pyrocoefficients noted in [11] and can be explained by effects caused by nonuni-

*Since no published data are available, the specific heat values of related PKR-1 ceramics of the ZTP system and of deuterated triglycine sulfate crystals without L-alanine doping have been stated.

form heating of the material in the dynamic measurements made with sample heating by infrared radiation sources [12, 13]. Thus the calibration of a pyrodetector of ionizing radiation in the optical wavelength range can lead to large errors of the detector characteristics.

In [1, 14] the high selectivity of pyroelectric detectors, particularly of detectors of lead-containing ceramics of the ZTP system, to γ radiation in mixed γ -neutron fields was mentioned. It should be noted in this connection that the relative contribution of each of the components of a mixed or composite radiation to the absorbed dose depends upon the energy spectrum of the radiation, the properties of the material (its chemical composition and density) and the ratio of the fluxes F_γ and F_n (see Eq. (4)). In the present work, for example, the neutron contribution to the absorbed dose reached 36% and 90% in the case of PKR-1 and deuterated tri-glycine sulfate, respectively. Thus the selectivity of the pyroelectric detector must be evaluated for each specific case. The Coulomb-rad sensitivity of 65/35 ZTP [2] was evaluated in an experiment in an SPR reactor $((0.76 \pm 0.2) \cdot 10^{-8} \text{ C} \cdot \text{m}^{-2}/\text{rad})$ in the case of 65/35 ZTP) and in "pure" γ units $((0.56 \pm 0.1) \cdot 10^{-8} \text{ C} \cdot \text{m}^{-2}/\text{rad})$ in the case of 65/35 ZTP). Better agreement between these values will obviously be obtained when the contribution of the neutron radiation of the reactor to be absorbed dose is brought into account.

LITERATURE CITED

1. D. Hester and D. Glower, IEEE Trans., NS-11, No. 5, 145 (1964).
2. D. Hester and D. Glower, Nucl. Appl., 3, 41 (1966).
3. R. Ya. Strakovskaya and L. S. Kremenchugskii, At. Energ., 51, No. 1, 37 (1981).
4. E. Z. Novitskii and V. A. Borisyonok, Problems of Atomic Science and Technology, Series "Nuclear Instrument Construction" [in Russian], No. 2(51), 61 (1982).
5. L. S. Kremenchugskii and R. Ya. Strakovskaya, At. Energ., 41, No. 3, 190 (1976).
6. E. G. Fesenko, A. Ya. Dantsiger, and O. N. Razumovskaya, New Piezoceramic Materials [in Russian], Rostov-on-Don Univ. (1983).
7. T. A. Dabizha and N. G. Maksimov, in: 9th All-Union Conference on Seignette Electricity (Abstracts of Reports) [in Russian], Part 2, Rostov-on-Don Univ. (1979), p. 189.
8. V. K. Novik, N. D. Gavrilova, and N. B. Fel'dman, Pyroelectric Converters [in Russian], Sovet-skoe Radio, Moscow (1979).
9. H. Beerme, Infrared Phys., 15, 225 (1975).
10. L. S. Kremenchugskii and O. V. Roitsina, Pyroelectric Radiation Receivers [in Russian], Naukova Dumka, Kiev (1979).
11. V. A. Borisyonok and E. Z. Novitskii, Problems of Atomic Science and Technology, Series "Nuclear Instrument Construction" [in Russian], No. 2(51), 70 (1982).
12. S. D. Pel'ts and A. E. Karpel'son, Kristallografiya, 18, 573 (1973).
13. L. Goulpeau and P. Sallio, C. R. Acad. Sci. Paris, 282, Ser. B, 539 (1976).
14. Z. A. Al'bikov, A. I. Veretennikov, and O. V. Kozlov, Detectors of Pulsed Ionizing Radiation [in Russian], Atomizdat, Moscow (1978).

How To Comply With The New COPYRIGHT Law

Participation in the Copyright Clearance Center (CCC) assures you of legal photocopying at the moment of need.

Libraries everywhere have found the easy way to fill photocopy requests legally and instantly, without the need to seek permissions, from more than 3000 key publications in business, science, humanities, and social science. You can:

Fill requests for multiple copies, interlibrary loan (beyond the CONTU guidelines), and reserve desk without fear of copyright infringement.

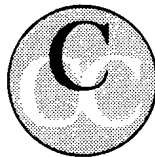
Supply copies from CCC-registered publications simply and easily.

The Copyright Clearance Center is your one-stop place for on-the-spot clearance to photocopy for internal use.

Its flexible reporting system accepts photocopying reports and returns an itemized invoice. You send only one convenient payment. CCC distributes it to the many publishers whose works you need.

And, you need not keep any records, the CCC computer will do it for you. Register now with the CCC and you will never again have to decline a photocopy request or wonder about compliance with the law for any publication participating in the CCC.

To register or for more information, just contact:



Copyright Clearance Center

21 Congress Street
Salem, Massachusetts 01970
(617) 744-3350

a not-for-profit corporation

NAME	TITLE		
ORGANIZATION			
ADDRESS			
CITY	STATE	ZIP	
COUNTRY	TELEPHONE		

CHANGING YOUR ADDRESS?

In order to receive your journal without interruption, please complete this change of address notice and forward to the Publisher, 60 days in advance, if possible.

(Please Print)

Old Address:

name _____

address _____

city _____

state (or country) _____ zip code _____

New Address

name _____

address _____

city _____

state (or country) _____ zip code _____

date new address effective _____

name of journal _____



233 Spring Street, New York, New York 10013

MEASUREMENT TECHNIQUES

Izmeritel'naya Tekhnika
Vol. 27, 1984 (12 issues) \$520

MECHANICS OF COMPOSITE MATERIALS

Mekhanika Kompozitnykh Materialov
Vol. 20, 1984 (6 issues) \$430

METAL SCIENCE AND HEAT TREATMENT

Metallovedenie i Termicheskaya Obrabotka Metallov
Vol. 26, 1984 (12 issues) \$540

METALLURGIST

Metallurg
Vol. 28, 1984 (12 issues) \$555

PROBLEMS OF INFORMATION TRANSMISSION

Problemy Peredachi Informatsii
Vol. 20, 1984 (4 issues) \$420

PROGRAMMING AND COMPUTER SOFTWARE

Programmirovaniye
Vol. 10, 1984 (6 issues) \$175

PROTECTION OF METALS

Zashchita Metallov
Vol. 20, 1984 (6 issues) \$480

RADIOPHYSICS AND QUANTUM ELECTRONICS

Izvestiya Vysshikh Uchebnykh Zavedenii, Radiofizika
Vol. 27, 1984 (12 issues) \$520

REFRACTORIES

Ogneupory
Vol. 25, 1984 (12 issues) \$480

SIBERIAN MATHEMATICAL JOURNAL

Sibirskii Matematicheskii Zhurnal
Vol. 25, 1984 (6 issues) \$625

SOIL MECHANICS AND FOUNDATION ENGINEERING

Osnovaniya, Fundamenty i Mekhanika Gruntov
Vol. 21, 1984 (6 issues) \$500

SOLAR SYSTEM RESEARCH

Astronomicheskii Vestnik
Vol. 18, 1984 (6 issues) \$365

SOVIET APPLIED MECHANICS

Prikladnaya Mekhanika
Vol. 20, 1984 (12 issues) \$520

SOVIET ATOMIC ENERGY

Atomnaya Energiya
Vols. 56-57, 1984 (12 issues): \$560

SOVIET JOURNAL OF GLASS PHYSICS AND CHEMISTRY

Fizika i Khimiya Stekla
Vol. 10, 1984 (6 issues) \$235

SOVIET JOURNAL OF NONDESTRUCTIVE TESTING

Defektoskopiya
Vol. 20, 1984 (12 issues) \$615

SOVIET MATERIALS SCIENCE

Fiziko-khimicheskaya Mekhanika Materialov
Vol. 20, 1984 (6 issues) \$445

SOVIET MICROELECTRONICS

Mikroelektronika
Vol. 13, 1984 (6 issues) \$255

SOVIET MINING SCIENCE

Fiziko-tekhnicheskie Problemy Razrabotki Poleznykh Iskopaemykh
Vol. 20, 1984 (6 issues) \$540

SOVIET PHYSICS JOURNAL

Izvestiya Vysshikh Uchebnykh Zavedenii, Fizika
Vol. 27, 1984 (12 issues) \$520

SOVIET POWDER METALLURGY AND METAL CERAMICS

Poroshkovaya Metallurgiya
Vol. 23, 1984 (12 issues) \$555

STRENGTH OF MATERIALS

Problemy Prochnosti
Vol. 16, 1984 (12 issues) \$625

THEORETICAL AND MATHEMATICAL PHYSICS

Teoreticheskaya i Matematicheskaya Fizika
Vol. 58-61, 1984 (12 issues) \$500

UKRAINIAN MATHEMATICAL JOURNAL

Ukrainskii Matematicheskii Zhurnal
Vol. 36, 1984 (6 issues) \$500

Send for Your Free Examination Copy

Plenum Publishing Corporation, 233 Spring St., New York, N.Y. 10013

In United Kingdom: 88/90 Middlesex St., London E1 7EZ, England

Prices slightly higher outside the U.S. Prices subject to change without notice.

RUSSIAN JOURNALS IN THE PHYSICAL AND MATHEMATICAL SCIENCES

AVAILABLE IN ENGLISH TRANSLATION

ALGEBRA AND LOGIC

Algebra i Logika
Vol. 23, 1984 (6 issues) \$360

ASTROPHYSICS

Astrofizika
Vol. 20, 1984 (4 issues) \$420

AUTOMATION AND REMOTE CONTROL

Avtomatika i Telemekhanika
Vol. 45, 1984 (24 issues) \$625

COMBUSTION, EXPLOSION, AND SHOCK WAVES

Fizika Goreniya i Vzryva
Vol. 20, 1984 (6 issues) \$445

COSMIC RESEARCH

Kosmicheskie Issledovaniya
Vol. 22, 1984 (6 issues) \$545

CYBERNETICS

Kibernetika
Vol. 20, 1984 (6 issues) \$445

DIFFERENTIAL EQUATIONS

Differentsial'nye Uravneniya
Vol. 20, 1984 (12 issues) \$505

DOKLADY BIOPHYSICS

Doklady Akademii Nauk SSSR
Vols. 274-279, 1984 (2 issues) \$145

FLUID DYNAMICS

Izvestiya Akademii Nauk SSSR, Mekhanika Zhidkosti i Gaza
Vol. 19, 1984 (6 issues) \$500

FUNCTIONAL ANALYSIS AND ITS APPLICATIONS

Funktional'nyi Analiz i Ego Prilozheniya
Vol. 18, 1984 (4 issues) \$410

GLASS AND CERAMICS

Steklo i Keramika
Vol. 41, 1984 (6 issues) \$590

HIGH TEMPERATURE

Teplofizika Vysokikh Temperatur
Vol. 22, 1984 (6 issues) \$520

HYDROTECHNICAL CONSTRUCTION

Gidrotekhnicheskoe Stroitel'stvo
Vol. 18, 1984 (12 issues) \$385

INDUSTRIAL LABORATORY

Zavodskaya Laboratoriya
Vol. 50, 1984 (12 issues) \$520

INSTRUMENTS AND EXPERIMENTAL TECHNIQUES

Pribory i Tekhnika Éksperimenta
Vol. 27, 1984 (12 issues) \$590

JOURNAL OF APPLIED MECHANICS AND TECHNICAL PHYSICS

Zhurnal Prikladnoi Mekhaniki i Tekhnicheskoi Fiziki
Vol. 25, 1984 (6 issues) \$540

JOURNAL OF APPLIED SPECTROSCOPY

Zhurnal Prikladnoi Spektroskopii
Vols. 40-41, 1984 (12 issues) \$540

JOURNAL OF ENGINEERING PHYSICS

Inzhenerno-fizicheskii Zhurnal
Vols. 46-47, 1984 (12 issues) \$540

JOURNAL OF SOVIET LASER RESEARCH

A translation of articles based on the best Soviet research in the field of lasers
Vol. 5, 1984 (6 issues) \$180

JOURNAL OF SOVIET MATHEMATICS

A translation of Itogi Nauki i Tekhniki and Zapiski Nauchnykh Seminarov Leningradskogo Otdeleniya Matematicheskogo Instituta im. V. A. Steklova AN SSSR
Vols. 24-27, 1984 (24 issues) \$1035

LITHOLOGY AND MINERAL RESOURCES

Litologiya i Poleznye Iskopaemye
Vol. 19, 1984 (6 issues) \$540

LITHUANIAN MATHEMATICAL JOURNAL

Litovskii Matematicheskii Sbornik
Vol. 24, 1984 (4 issues) \$255

MAGNETOHYDRODYNAMICS

Magnitnaya Gidrodinamika
Vol. 20, 1984 (4 issues) \$415

MATHEMATICAL NOTES

Matematicheskie Zametki
Vols. 35-36, 1984 (12 issues) \$520

continued on inside back cover